

Microthermal analysis of polymeric and biological materials

by

Nobumichi Fuchigami

A thesis submitted to the graduate faculty

In partial fulfillment of the requirements for the degree of

MASTER OF SCIENCE

Major: Materials Science and Engineering

Major Professor: Vladimir V. Tsukruk

Iowa State University

Ames, Iowa

2001

Copyright © Nobumichi Fuchigami, 2001. All rights reserved.

Graduate College
Iowa State University

This is to certify the Master's thesis of
Nobumichi Fuchigami
has met the thisis requirement of Iowa State University

Signatures have been redacted for privacy

TABLE OF CONTENTS

LIST OF FIGURES	v
LIST OF TABLES	xii
ACKNOWLEDGEMENTS	xiii
ABSTRACT	xv
1. INTRODUCTION.....	1
1.1. The Micro – Thermal Analysis.....	1
1.2. Biomimetics Systems.....	2
1.3. Polymer Ultra – Thin Films	3
1.4. Objectives and Goals of the Project.....	4
2. LITERATURE SURVEY	6
2.1. From the SPM to the Micro – TA.....	6
2.2. Infrared Receptor in Snake Head and Beetles Body.....	8
2.3. Polymer Ultra – Thin Film and the Glass Transition Temperature	10
3. METHODOLOGY	13
3.1. Scanning Thermal Microscopy (SThM)	13
3.1.1. Thermal conductivity contrast	13
3.1.2. Scanning thermal microscope probes	15
3.1.3. Thermal – distance curve	16
3.1.4. The measurement principle and calibration procedure for the localized microthermal probing.....	17
3.2. Micro – Thermal Analysis (μ TA).....	20
3.2.1. Micro – thermal mechanical analysis (μ TMA).....	21
3.2.2. Micro – differential scanning calorimetry (μ DSC).....	21
3.2.3. Experimental procedure	21
4. EXPERIMENTAL SPECIFICS, RESULTS, DISCUSSION, AND CONCLUSIONS	24
4.1. Microthermal Probing by Scanning Thermal Microscopy	24
4.1.1 .Experimental	24
4.1.2. Results and discussion	27
4.2. Microthermal Analysis with Scanning Thermal Microscopy, Calibration	35
4.2.1. Surface thermal conductivity	35
4.2.2. Simulations of thermal behavior	38
4.2.3. Conclusions.....	43

4.3. Ultra-microstructure and Microthermomechanics of Infrared Detectors in the Beetle <i>Melanophila acuminata</i>	45
4.3.1. Experimental	46
4.3.2. Results and discussion	48
4.3.3. Conclusions and prospectives	61
4.4. Ultra-microstructure and Microthermomechanics of Snake IR Receptors	62
4.4.1. Experimental	63
4.4.2. Results and discussion	64
4.4.2.1. Surface morphology	64
4.4.2.2. MicroThermal properties	72
4.4.2.3. Micromechanical properties	81
4.4.2.4. Tissue microstructure: preliminary data	87
4.4.3. Conclusions	91
4.5. Microthermal Analysis of Polymer Ultra-thin Films	92
4.5.1. Experimental	92
4.5.2. Results and discussion	95
4.6. Calibration of the Cantilever Spring Constant	99
4.6.1. The cantilever – against – cantilever measurement	99
4.6.2. Added end mass method using tungsten micro-sphere	106
4.6.3. The tip radius measurement	109
4.6.4. Conclusions	113
BIBLIOGRAPHY	114

LIST OF FIGURES

Figure 3.1.	Thermal conductivity mode scheme.	14
Figure 3.2.	MicroThermal Probe. Tip is made of filament of the Wollaston wire (platinum/10% rhodium alloy). The diameter of the tip is 5 μm with radius curvature about 10 μm . The total length of the thermal probe is close to 3 mm and the spring constant is estimated as approximately 6 N/m (Topometrix, private communication). The very end of the tip is etched to expose the platinum core.	16
Figure 3.3.	The geometry of the thermal sensing loop and hemispherical model used in this project for data processing and modeling.	19
Figure 4.1.	The topographical (left) and thermal (right) images of grids composed of silicon coated with a thin silicon oxide layer with periodicity 16 x 16 μm	28
Figure 4.2.	Thermal signal and probe deflection versus tip-surface distance during approaching cycle for platinum, silicon, glass, and PEHD samples. The approaching velocities are 5 μm and the probe temperature is 70 $^{\circ}\text{C}$	29
Figure 4.3.	The heat dissipation versus tip-surface distance calculated from the experimental data for gold and polystyrene surfaces along with the force-distance curve; the initial probe temperature is 40 $^{\circ}\text{C}$	30
Figure 4.4.	The probe heat dissipation versus tip-surface gap width calculated from experimental data for gold and polystyrene at two approaching velocities; initial probe temperature is 80 $^{\circ}\text{C}$	31
Figure 4.5.	The surface temperature versus the tip-surface gap calculated from experimental data for polystyrene and gold surfaces; the initial probe temperature is 40 $^{\circ}\text{C}$	32
Figure 4.6.	The variation of ΔQ versus ΔT as calculated from experimental data for polystyrene surface and corresponding linear approximation.	34

Figure 4.7.	μ DSC thermogram for the polystyrene surface with a linear approximation of the thermal signal within the temperature interval between room temperature and glass transition temperature. The slope correlates with the surface thermal conductivity according to the equation (9).	34
Figure 4.8.	The thermal conductivity versus probe heat dissipation using various materials	37
Figure 4.9.	The simulation of the heat dissipation of the thermal probe and the surface temperature variation versus the tip-surface gap width between the thermal probe and gold or polystyrene surfaces. The initial gap width is 10 μm and two probe velocities are 1 $\mu\text{m}/\text{sec}$ and 5 $\mu\text{m}/\text{sec}$	39
Figure 4.10.	The simulation of the surface temperature variation versus the tip-surface gap width between the thermal probe and gold or polystyrene surfaces. The initial gap width is 10 μm and two probe velocities are 1 $\mu\text{m}/\text{sec}$ and 5 $\mu\text{m}/\text{sec}$	39
Figure 4.11.	The simulation of the surface temperature of gold versus the tip-surface gap width between the thermal probe and gold.	42
Figure 4.12.	The simulation of the surface temperature of polystyrene versus the tip-surface gap width between the thermal probe and polystyrene.	42
Figure 4.13.	Time variation of the surface temperature for PS, PEHD, and gold surface under the thermal probe located at 10 μm above the surface after turning in its temperature to 40°C.	44
Figure 4.14.	Schematic drawing of the IR sensillum. The internal cuticular sphere is composed of three distinguishable areas (1 – 3) and covered by a thin outer cuticle. Three enveloping cells (theco-, tricho-, and tormogen cell) surround the sensory neuron which is anchored with the tip of the dendrite within the peripheral area 3. DIS: dendric inner segment; DOS: dendric outer segment; i.r.l.c.: inner receptor lymph cavity; o.r.l.c.:L outer receptor lymph cavity. Diameter of the spere is about 12 μm . Adapted from Vondrdan, 1995.....	47

Figure 4.15.	Optical micrograph of cross section of IR receptor area of beetles <i>Melanophila acuminata</i>	49
Figure 4.16.	Optical micrograph of IR receptor area of beetles <i>Melanophila acuminata</i> from front side.	49
Figure 4.17.	SEM micrographs of the receptor array after drying procedure at different magnifications taken by Dr. Stone in AFRL.	50
Figure 4.18.	SPM topographical image of microtomed ultrathin slices of the receptor areas at low magnifications.	51
Figure 4.19.	SPM topography (left) and lateral force (right) images of multilayered structures in outer areas of IR receptors at intermediate magnifications.	51
Figure 4.20.	SPM topography (left) and amplitude deflection (right) images of multilayered structures with fine grainy morphology at highest magnifications.	53
Figure 4.21.	SPM topography (left) and phase (right) images of multilayered structures in outer areas of IR receptors at 70°C.	53
Figure 4.22.	SPM topography (left) and phase (right) images of multilayered structures in outer areas of IR receptors at 70°C.	54
Figure 4.23.	SPM topography (left) and phase (right) images of multilayered structures in outer areas of IR receptors at 25°C.	54
Figure 4.24.	Micromapping of elastic modulus (32 x 32 pixels, 4 x 4 μm) (top-left) and corresponding surface histogram distribution of elastic modulus (bottom-left). Top-right and bottom-right images are the examples of Young's modulus depth dependence and the original force-distance curves, corresponding to the number in the elastic modulus mapping respectively.	55

Figure 4.25.	Micromapping of adhesive forces (32 x 32 pixels, 4 x 4 μm) (top-left) and corresponding surface histogram distribution of elastic modulus (bottom-left). Bottom-right image is the examples of the original force-distance curves, corresponding to the number in the adhesive forces mapping respectively.	56
Figure 4.26.	SThM topography (left) and heat dissipation (right) images of a section of the IR receptor.....	58
Figure 4.27.	Temperature variation of multilayered spacing for sections of the IR receptors during heating cycle.	60
Figure 4.28.	Special micro-stage supporting 100 % humid environment to biological samples by wet towel bridge. Samples are placed on the silicon substrate. Concave shape of the surface makes SPM scan less difficult.....	65
Figure 4.29.	3D surface morphology of snake skin (alive Indian Python)	65
Figure 4.30.	3D surface morphology of snake skin (alive Indian Python) (3-D image analysis of Figure 4.29).	66
Figure 4.31.	3D surface morphology of snake IR receptor (alive Indian Python).....	67
Figure 4.32.	3D surface morphology of snake IR receptor (alive Indian Python) (3-D image analysis of Figure 4.30).....	67
Figure 4.33.	The distribution of the width of layers for alive Indian Python comparing the pit area to non-pit area.	70
Figure 4.34.	SThM images for Ball Python: morphology (left) and thermal conductivity (right).	70
Figure 4.35.	The distribution of the diameters of nanopits for alive Indian Python comparing the pit area to non-pit area.....	71
Figure 4.36.	The distribution of the depths of nanopits for alive Indian Python comparing the pit area to non-pit area.	71
Figure 4.37.	The average values of the width of a pit layer for three different kinds of snakes.	73

Figure 4.38.	The average values of the distances between nanopits for three different kinds of snakes.	73
Figure 4.39.	The average values of the depths of nanopits for three different kinds of snakes.	74
Figure 4.40.	The average values of the diameters of nanopits for three different kinds of snakes.	74
Figure 4.41.	SThM images for Ball Python: morphology (left) and thermal conductivity contrast (right).	75
Figure 4.42.	Thermal distance curve for snake pit area and non-pit area using Ball Python. Probe temperature was 60 °C, and approaching velocity of the probe was 1 µm/sec.	76
Figure 4.43.	The dissipated heat during approaching-retracting motion of a thermal probe to the surface of snake pit and non-pit area using different initial probe temperatures.	76
Figure 4.44.	Microthermograms for the IR receptor (top) and the non-specific skin areas (bottom) of Ball Python. Heating rate was 5 °C/sec, and the same thermal probe was used for both measurement to keep the same conditions.	77
Figure 4.45.	Histogram of surface distribution of thermal conductivities across receptors areas and outside receptors.	79
Figure 4.46.	Variation of surface temperature for receptor and non-specific areas during approaching thermal tip pre-heated to 40 °C (left) and time-dependence of temperature gradient after turning on heat source (right).	81
Figure 4.47.	The surface Young's modulus (middle) and stiction (adhesion) (top-right) mapping corresponding to the pixel – by- pixel morphology image (top-left) and the distribution of Young's modulus values (bottom) using full-range penetration for pit area of alive Indian Python.	82
Figure 4.48.	The surface Young's modulus (middle) and stiction (adhesion) (top-right) mapping corresponding to the pixel – by- pixel morphology image (top-left) and the distribution of Young's modulus value (bottom-right) using full-range penetration for non-specific skin area of alive Indian Python.	83

Figure 4.49.	An example of force-distance curve (top) and the calculated penetration-load curve (bottom). Sample was alive Indian Python and the place was non-specific skin area.....	84
Figure 4.50.	The penetration dependence of Young's modulus for IR receptor (top) and non-specific skin (bottom) area.	86
Figure 4.51.	AFM scanning image of underlying tissue of snake IR receptor area, which demonstrates collagen fibers taken by John Hazel, Western Michigan University.	88
Figure 4.52.	AFM scanning image of underlying tissue of snake IR receptor area taken by John Hazel, Western Michigan University.....	89
Figure 4.53.	AFM scanning image of underlying tissue of snake IR receptor area taken by John Hazel, Western Michigan University.....	90
Figure 4.54.	Sketch of the SThM detection scheme for ultrathin films measurements (right) and the micrograph of the actual thermal probe (left).	94
Figure 4.55.	Microthermal probing of bulk sample of PET (top) and PS film with 200 nm thickness on silicon substrate (bottom) at various heating rates. Data plots are offset along y-axis.	96
Figure 4.56.	μ DSC of the PS films with different thicknesses on silicon substrate (data plots are offset along y-axis).....	97
Figure 4.57.	The variation of glass transition temperature for PS films with different thicknesses.	97
Figure 4.58.	The scheme of cantilever – against – cantilever spring constant measurement.....	100
Figure 4.59.	The position of the tip on v-shaped cantilever.....	100
Figure 4.60.	The cantilever of AFM with tungsten added mass..	102
Figure 4.61.	The spring constant of cantilevers versus (resonant frequency) ³ for non-contact Si_3N_4 coated Si short cantilever.....	104

Figure 4.62.	The spring constant of cantilevers versus (resonant frequency) ³ for contact Si ₃ N ₄ coated Si long cantilever.	105
Figure 4.63.	The spring constant of cantilevers versus (resonant frequency) ³ for contact Si ₃ N ₄ coated Si short cantilever.	105
Figure 4.64.	The result of added end mass measurement using silicon cantilever. Slope is the spring constant of cantilevers.	107
Figure 4.65.	The plot of spring constants of cantilevers obtained by added end mass method versus the spring constants of cantilevers obtained by cantilever – against – cantilever method. The data are from Table V.	109
Figure 4.66.	Scanning image of gold nanoparticles by AFM. The average diameter of the particles were 28 nm.	110
Figure 4.67.	The cross section image of gold particle (left) and schematic drawing of AFM tip scanning of gold nanoparticle (right). From height and width data of captured gold nanoparticle image, the radius of AFM tip is calculated.	110
Figure 4.68.	The distribution of the diameters of gold nanoparticles counted by AFM. Manufacturer provided the size as 28.3 nm.	112

LIST OF TABLES

Table I.	The parameters of mechanical and thermal properties for delegation materials (data are taken from Tong (1994) and Internet databases of MatWeb, MEMS Materials Database, CenBASF/Materials).....	25
Table II.	The average value of the morphological parameters for three types of snakes. Carpet Python data are taken from Campbell et al., 1999.....	69
Table III.	Young's modulus & Thermal conductivity of three types of snakes calculated from experimental data.	79
Table IV.	Glass transition and melting temperatures as measured by μ TA.....	94
Table V.	The spring constants of cantilevers from added end mass method and cantilever – against – cantilever method corresponding data of Figure 58. Only short cantilevers were employed for added end mass measurement due to the availability for experiment.....	105

ACKNOWLEDGEMENTS

Studying in the Iowa State University and Western Michigan University to complete the program of Master of Materials Science & Engineering took me nearly three years. During this time, I have been helped by many people, so here I would like to appreciate them from the bottom of my heart. First of all, to my adviser, Dr. Vladimir V. Tsukruk, who found me and gave me an opportunity to work in science world. Polymer science, my new challenging world, taught me that all science and engineering are connected each other in universal language. The attitude and passion will determine future direction of our research work. The joy and feeling of achievement come from our daily effort. Dr. Tsukruk was also a greatest teacher I have ever met. When he speaks to students, he uses familiar words to us, and try to let us participate in the core of discussion. I also personally learnt the importance of statistics working with him. Now all of these are my properties which will never disappear during my life time. He also always encouraged and helped me in my personal struggle. I would like to say thank you to this great scientist and a human being.

I had also the privilege to work with Dr. Valeriy V. Gorbunov, ThermoMicroscopes, and John L. Hazel. They are beyond my colleagues and advisers. Without their guidance and support, this work could not be done.

I also would like to thank Dr. Igor Luzinov, Dr. Alexander Sidorenko, and Duangrut Julthongpiput for their help in polymer studying, and Marina Ornatska for her help in biology studying. I would like to express my appreciation to everybody in this laboratory from the bottom of my heart.

I also would like to thank following people who contributed to this work: Dr. Joshua Otaibe and Dr. Steve Martin for providing instrumentation of thermal measurement, Brad Tischendorf and Jeremy Schrooten for their help in technical assistance of thermal measurement, and Dr. Moorely Stone, Wright Labs, USAF, for providing snake samples and SEM measurement, Dr. Michael Grace, Florida Institute of Technology, for providing living snake samples, Dr. Helmut Schmitz, Universität Bonn, for providing microtomed beetles sample, Dr. Daniel X. Hammer, University of Texas at Austin for collaboration of living

beetle's measurement, and providing beetle samples, Dr. Joshua Otaigbe and Dr. Surya Mallapragada for their supports and advices as my program of study committee members.

My thanks also go to the Department of Materials Science & Engineering, ISU, and College of Applied Science, WMU.

Finally, I would like to thank Yichuan Li and my family for their warm support and encouragement.

Funding for this research at ISU and WMU was provided by the National Science Foundation and the Air Force Office of Scientific Research.

Nobumichi Fuchigami

ABSTRACT

Morphology of biological IR receptors was investigated by Scanning Probe Microscopy. Micro-Thermal Analysis (μ -TA) and Scanning Thermal Microscopy (SThM) were adopted and were modified to analyze micro-thermal properties of biological IR receptors and polymer ultra-thin films. The methodology, instrumentation, parameter optimization, and calibration procedure for μ -TA, SThM, and SPM were established.

Based on our developed model for the analysis of approaching – retracting data of thermal probes, the thermal conductivity of variety of polymers were measured and used for calibration procedures. The resultant values were fairly close to the known bulk thermal conductivities. Our original modified μ -TA scheme provided the glass transition temperature and the melting temperature of ultra-thin polymer films with thicknesses down to 10 nm, which are the first direct measurement in the world.

The thermal conductivity surface distribution of snake IR receptor and beetles IR receptor showed clear influence of morphology. SPM confirmed highly ordered multilayered organization of outer shells in beetle IR receptors and the receptors surfaces were thoroughly characterized by SPM and μ -TA. For snake IR receptor, nanopits arrays onto the micro-terrace like structure were confirmed and the dimension parameters were compared with the data from other species. The thermal conductivity of outer receptor area of snake was 0.34 W/m-K, and that of receptor area was 0.11 W/m-K.

1. INTRODUCTION

1.1. The Micro-Thermal Analysis

The Micro-Thermal Analysis (μ -TA) is a new method which was developed for studying of localized thermal property of materials surface several years ago (Hammiche, et al, 1996). Micro-TA is a collection of techniques that use SPM technology to study the relationship between temperature and the properties of a material on a microscopic scale. Basically this system is the combination of the SPM and thermal analysis.

The SPM technique is a relatively new tool for studying of surface properties on a sub-micron scale (Binning and Quate, 1986). In the SPM, sharp tip is monitored as it is moved across a sample. The behavior of the tip during this scanning is used to infer characteristics of the surface. Topography is established by recording the height of the tips during it is scanned in a raster pattern across the surface. The SPM has been improved to provide most accurate and high resolution tip control. Now the SPM can scan from hundred micrometer down to tens of nanometer level (Digital Instrument, Inc). As a proof of the precise controlled motion of piezoelectric tubes, the detection of one protein molecule was demonstrated by attaching one end of the molecule to an SPM tip and the other to a sample surface then moving the tip away from the surface (Reif et al., 1997).

In addition to the normal topography scanning, the SPM has another important feature, which is characterization of the surface-probe interaction at a single point of contact. Chizhik et al. used this single point contact measurement to investigate the localized elasticity of the polymer surface with sub-micron resolution in 1998. Now this measurement is known as micro-mechanics measurement and actually gives a way to micro-thermal probing measurement (Gorbunov, Fuchigami, and Tsukruk, 2000).

In the characterization of the materials, thermal analysis has been one of the strong tools to characterize materials and developed many applications such as the differential scanning calorimetry (DSC), thermal mechanical analysis (TMA), and thermal gravimetric analysis. Thermal analysis examines the change of materials condition as a function of temperature. Thermograms obtained from thermal analysis include the information about thermodynamics, heat flow physics, and molecular behavior, which help researchers to

characterize and analyze the materials. Generally these conventional thermal analyses are only applicable to bulk samples. The data are averaged over the volume of a material which is usually order of a few mm^3 .

Hammiche et al. established the μ -TA in 1996 combining the SPM and conventional thermal analysis. The capability of controlled motion with sub-micrometer in the SPM was apparently promising for the μ -TA's concept which is to measure the local thermal properties with sub-micron resolution using ultra small forces.

Hammiche et al. demonstrated first experiment for polymer blends. μ -TA can also be useful for micropatterning of polymeric-organic interfaces. In practical use, the thermal detection of device failure (Lai et al., 1995) and sub-surface detection of polymer embedded with metallic particles (Hammiche et al., 1996) was demonstrated. The μ -TA has demonstrated the promising performances.

1.2. Biomimetics Systems

The design of man-made materials through guidance from nature is called biomimetics. The current infrared (IR) technology for heat detection is not sensitive enough to detect heat for looking at a satellite or an aircraft. While man-made infrared device can only detect several tenths of a degree, the infrared receptor in pit vipers can sense a thousandth of a degree from 10-20 m away of the object in a unique way (Newman and Hartline, 1982). Another big problem is that man-made IR devices are large and cumbersome, as well as expensive to operate with liquid nitrogen. Snakes, on the other hand, have made heat sensing visually detectable through small pits near their eyes. The work of biomimetics consists of theoretical works on biomechanics, physiology, thermal mechanism, chemistry, and morphology. Ultimate goal of biomimetics system is to obtain significant improvements in applied materials and systems through the understanding and description of the evolutionary-optimized structure and function of biological systems (Srinivasan et al., 1996).

In this research, we study about the IR receptor in snakes and beetles. Many research has been done on snake IR receptor, however, those were not characterization of IR tissues but biological and physiological study. Using μ -TA, we challenge the first attempt of

materials characterization for snakes and beetles IR receptor. We believe highly localized micro-scale thermal analysis will bring substantially different aspects for evaluation of IR receptor.

1.3. Polymer Ultra-Thin Films

The morphological characteristics of thin films at solid interfaces is of great technological importance to a wide variety of applications such as dielectric layers, coatings, composites, electronic packaging, lubrication, and biocompatible materials. These properties of polymer thin films attract microelectronics, medical, and chemical industries. In microelectronics, polymers are used as resists for microlithography and as packaging materials. While the main function of the packaged electronic assembly is the conduction of signals through the device, the equal or greater importance is in the insulation of the polymer (Thompson, 1994).

Temperature affects the properties of polymeric materials greatly. Both physical and chemical changes can occur with the exposure of the materials to different temperatures. Polymers, unlike metals or ceramics which have a higher temperature exposure limit, have a considerably restricted temperature range. This is why thermal properties of polymers are quite important, especially when the application polymer has many possibilities to expose huge range of temperature. There are several key parameters to evaluate thermal properties of polymers; thermal conductivity, specific heat, glass transition temperature, melting temperature, and thermal expansion coefficient. The principles of the differential scanning calorimetry and the thermal mechanical analysis are ideal for the investigation of these parameters.

When polymers form thin films, the properties of the polymers often change significantly because the mechanical and thermal properties of polymers depend on the morphology, molecular structure, and thickness. For instance, when a small percentage of polymer network is formed within liquid crystals, the mechanical strength of the film increases dramatically due to their susceptibility to mechanical shock (Guymon et al., 1996).

Due to the increasing demand of polymer thin-films in industry, thermal analysis for such materials is desired.

1.4. Objectives and Goals of the Project

This research is a part of project in development of artificial IR sensors. Morphological study and micro-thermal property investigation are the core of this research. Our hope is to make significant contribution for biomimetic precision sensing. For the investigation of the IR receptors, we will do morphology measurement to reveal micro-structure using SPM, and micro-thermal property investigations using μ TA. We believe that morphology investigation and micro-thermal analysis for IR receptors will make substantial contribution to the development of artificial IR sensor. Especially direct measurement of micro-thermal property measurement has never been attempted although its importance was widely recognized.

We established SThM and μ TA systems in our laboratory. After installation of this system, we started understanding of instrumentation. Development of thermal imaging mode and testing of its applicability for snake skins were important steps to achieve our aim. In this development, identification of lateral resolution of thermal micro-probes and thermal conductivity resolution should be clarified. Also we quantify function of tip-sample heat transfer for various materials. Integrating these tasks, we establish probing protocol for local thermal properties measurements. This step give a way of highly quantified micro-thermal analysis for IR receptors.

In scanning the biological tissues by SPM, there are some problems which are not seen in scanning solid materials. To dissect snake IR receptor (pit) by micro-surgery is one of challenging tasks. In order to scan biological tissues by SPM, those tissues should be sliced very smoothly and should be as thin as 0.5-1.5 mm. Besides, those tissues should be attached on the scanning stage, and humidity should be kept constant. Micro-surgery tools and its protocol, development of micro-precision stage, and system for humidity control is achieved in this project. In scanning the IR pit by SPM, ultimately we would like to scan very stable image by reducing damage and keeping natural environment.

Combining the protocol of micro-thermal probing and that of SPM scanning for biological tissues, we investigate the micro-thermal property of IR receptors.

On top of above works, to pursue and develop further potential of micro-thermal analysis, we will investigate polymer thin films using μ -TA. We make the original scheme of μ -TA instrument for this particular work since polymer thin films are assembled on silicon substrate which has much higher thermal conductivity than polymeric materials.

2. LITERATURE SURVEY

2.1. From the SPM to the Micro-TA

As one application for the concept of the scanning tunneling microscopy, the SPM was introduced (Binnig and Quate, 1986). The SPM is concerned with the measurement of ultrasmall forces on particles as small as single atoms. As it has been a common practice in materials characterization, the concept of the SPM is to use the displacement of springs as a measure of force. The force required to move the cantilever beam through measurable distances (10^{-1} Å) can be as small as 10^{-12} N. This level of sensitivity clearly represents the regime of interatomic forces between single atoms and open the door to the various applications. The SPM is a tool designed to exploit this level of sensitivity. It can be used to investigate both conductors and insulators.

Several SPMs and its applications have been invented to date. One of the major applications is the scanning thermal microscopy (SThM). The SThM uses a small temperature-sensing scanning probe to measure temperature fields on a surface or study probe-sample energy transport. Interestingly, the origin of the SThM was elaborated to build alternative of the invention of the scanning tunneling microscopy (STM), even before the invention of the SPM, which can be thought as a predecessor of the SPM (Williams and Wickramasinghe, 1986, 1988). In its original configuration, the tip-sample heat conduction was used as a feedback signal. Hence, this allowed imaging of insulating materials, which was advantageous over the STM. In their work, Williams and Wickramasinghe achieved a spatial resolution of the order of tens of nanometers, and a thermal resolution of about a millidegree. They used the special probe which consists of a coaxial tip that forms a fine thermocouple junction. The SThM gave a way to biological spectroscopy with sub 100 nm resolution and thermal characterization of materials. In the recent past, most of the effort has been focused on developing temperature-sensing cantilever probes that can be used in an SPM configuration (Nonnenmacher and Wickramasinghe, 1992). In this scheme, both force feedback loop and thermal feedback loop work independently. As a result, the ability to obtain thermal and topographical images of a surface simultaneously was achieved.

One serious problem in the thermal imaging was the invention of miniaturized thermal probe. Two major designs, used to date, explored either a microthermocouple (Lai et al., 1995, Luo et al., 1997) or a microthermoresistor (Hammiche et al., 1996) as a miniature probe, which scanned across a surface in a usual SPM mode. The concerns in manufacturing the miniaturized temperature sensors are how easily it can be fabricated and how sharp the tip end is. Using nanofabrication technique, microthermoresistors achieved the spatial resolution of 24 nm (Luo et al., 1997). On the contrary, the spatial resolution of microthermoresistors was estimated as submicron (Gorbunov, Fuchigami, and Tsukruk, 2000).

Although the spatial resolution of microthermoresistors is inferior to that of microthermocouples, microthermoresistors can act as both heat sources and thermometers. Using the SThM's system with microthermoresistors, Hammiche et al. developed a new instrumentation whose aim was to combine modulated temperature differential scanning calorimetry (MT-DSC) and scanning probe technology, that is 'calorimetric analysis with scanning probe microscopy' in 1996. Thus finally μ -DSC became reality. This new tool can build the mapping of surface calorimetric information. The characteristic temperatures obtained by μ -DSC for major polymer such as PEHD, PS, PET, and nylon showed close values as the values obtained by conventional DSC. In the μ -DSC, main events under melting point, which are glass transition, recrystallization, and melting, shows reproducible results in any location, and each temperature doesn't vary due to the location. The height of the peak depends on the location, thermal history, and the condition of the probe. Above the melting point, μ -DSC shows several peaks tentatively associated with degradation effects, the breaking of particular bonds, and also the effect of possible changes in mechanical contact area between probe and sample (Hammiche et al., 1996.)

As a sub-product of μ -DSC, μ -TMA was born at the same time. By monitoring the probe position during μ -DSC, the TMA data with submicron resolution can be obtained. The data obtained by μ -TMA is very similar to the one obtained by conventional TMA.

Potential usage for Micro-TA is micropatterning polymeric-organic interfaces. The accuracy and probe positioning in the SPM scheme and capability of thermal probe temperature control would make highly localized thermal pyrolysis to do micropatterning.

2.2. Infrared Receptor in Snake Head and Beetles Body

In the process of evolution of natural selection, nature developed most advanced and competitive system in itself. Actually human found the many of the amazing mechanisms of nature after establishing the today's advanced technology world. Nature still represents most sophisticated body, however, human technology is growing so rapidly that someday we may be able to mimic highly complicated system of nature. Clone animals such as sheeps and goats surprised us very recently.

Materials science field is also attracted to the beauty of nature. Air Force Office of Scientific Research (AFOSR) started the project of biomimetics in 1991 (Srinivasan, 1996). In this project, one of main purposes is to develop high sensitive artificial IR detectors. Snake IR receptors were chosen as research objects for this particular topic due to the superb functions and features compared to the artificial IR detectors. Although excellent infrared sensors are available today based on materials such as mercury cadmium telluride and platinum silicide, most current man-made infrared receptors have substantial volume and weight as a practical use. Besides these equipments must be cooled to cryogenic temperatures to get the satisfactory sensitivity. In these schemes, significant improvements are potentially obtainable. In contrast, nature has evolved very compact and extremely sensitive infrared receptor.

Pit vipers (snake) can sense a temperature difference of 0.003°C in their environment, which is easily more than ten times better than any man-made infrared sensor available (Newman and Hartline, 1982). In 1950's Bullock et al. made direct measurement of the temperature sensitivity of the trigeminal nerve in the rattlesnake pit organ (Newman et al., 1982). They controlled the temperature of the pit by directing a stream of warm water into the pit cavity. This sensitive system demonstrated the noticeable temperature sensitivity as small as 0.003 degree Celcius. Gathering the thermal information from this infrared

receptor, snakes can strike the target at various angles from zero to 60 degrees to the left or right of where the snake is facing.

Later the morphology of snakes IR receptors were investigated using SPM (Campbell et al, 1999, Amemiya et al., 1995). Campbell et al. studied the morphology of the infrared receptor (pit) by the SPM and the scanning electron microscopy in 1999. They examined the IR receptors (pits) themselves and non-IR receptors (non-pit) area (scale) architecture. In their studying, the microstructure of pits and non-pits have several common features; the highly dense distributed micropits, the structure made of many plates which appears to slide, and sinusoidal shape of the end of each plate. The critical difference of the mean micropits distance and the dimensions between pits and non-pits area indicate that micropits have a specific meaning or function. They proposed that micropits may work as a filter of infrared radiation.

Motivated by the above work, Hazel et al. focused on the studying of non-pits area using SPM. They discovered the nanoscale structure of snake skin and its mechanism for smooth locomotion using the SPM in 1999 (Hazel, 1999). The nanoarchitecture of snake skin revealed micro-hair like fibrils and micropits evenly distributed over the surface. To investigate the friction system in the snake skin at the micro-scale, friction force microscopy was employed. It proved that the end of the microfibrils provide much friction when the tip scanned from tail to head or backward snake motion, and vice versa when scanned from head to tail. This means when snakes move forward, they don't have much friction, thus they can go forward smoothly, and when going backward, it will come up with much friction. The design of the microfibrils consists of double-ridge and one steep ends, which may reduce the friction when snakes move forward, and may also serve as an effective stopper with the steep ends. As a next step, the snake skin was placed onto the viscous liquid which can be cured after a while. After drying, the SPM study revealed that the viscous liquid penetrated through the micropits. It was concluded that micropits may be continuous pores which can deliver viscous fluids across snake skin. Micropits may serve for permeability control, delivery of lubricant or anti-adhesive fluid to the contact area of the surface. This study proved that snake skin has highly sophisticated microscopic design and is a very effective evolutionary solution for reptation locomotion.

For the IR receptor, in addition to these morphological studies, thermal investigation with micro-level resolution is critical because the effective transmission of thermal stimuli to terminal nerve mass requires specific thermal properties of the IR receptor surfaces and these properties are untested to date. The understanding of unique thermal properties of biological heat detectors is, obviously, important step in attempts of mimicing their high sensitivity in the design of “soft matter”-based artificial IR detectors. Taking into account that dimensions of major sensing elements are on a micrometer scale (0.1-10 μm), the solution should be thought on a microscale level.

In addition to the IR receptor in snakes, we investigate the IR receptor in beetles as well. Only reptiles and insects have sensitivity to IR radiation. Among insects, *Melanophila acuminata* beetles are capable of distant detection of forest fires via IR paired thoracic pit organs (Evans, 1964). Behavioral and physiological studies have shown that the pit organs are most sensitive to IR radiation in the wavelength range between 2 and 4 μm (Evans, 1966, Schmitz et al., 2000). In behavioral experiments, a radiation intensity of only 60 $\mu\text{W}/\text{cm}^2$ at a wavelength of 3 μm was sufficient enough to elicit a response in the beetle (Evans, 1966). Each organ contains of 50-100 spherical IR sensillae. Morphology investigation and micro-thermal measurement will be applied to this biological samples as well.

2.3. Polymer Ultra-Thin Films and the Glass Transition Temperature

Nowadays polymer thin films play an important role in many industries. Microelectromechanical systems (MEMs) have serious problems in the friction control. These friction can cause low wearability and short life time of the MEMs. This friction is occurred by micro-tool's motion on silicon substrate because silicon surfaces have very high surface energy. To reduce the friction in MEMs, polymers can be employed as efficient lubricants. The lubricant polymers should be as thin as 10 nm or less than that, which consists of a few molecules, and should be homogeneous. These lubricant polymers layers can be combination of several layers. In this case, the layer between other layers should work as adhesives.

In 1999, Luzinov et al. fabricated a self-assembled monolayer using epoxy surface groups to serve as a template for chemical anchoring of polymer layers. Resultant

monolayers were truly monomoleculars, dense, homogeneous, and firmly attached to the surface. The thicknesses of the SAMs were measured by ellipsometry, and the morphologies were examined by the scanning probe microscopy. The friction force on the surface was measured by friction force microscopy. The self-assembled monolayer proved the ability to serve as adhesives.

Including SAMs, the polymer thin films which have less than 10nm thickness is called polymer ultra-thin films. Smooth and stable surfaces and interfaces are essential for many applications such as dielectric layers, coatings, composites, packaging, lubrications, adhesives, and biocompatible materials. The special geometries of the polymer ultra-thin films cause the unique properties of polymer ultra-thin films. The surface-to-volume ratio of polymer ultra-thin film is much higher than that of bulk polymers. Because of the high ratio of interface in polymer ultra-thin films, the energetic interaction at surfaces is largely different from bulk materials. Therefore, scientists focus on the molecular ordering at the interfaces, inherent stress-strain correlation, and thermal expansion coefficients lately (Beaucage et al., 1993). In other words, the importance of understanding the temperature dependence of morphological changes of thin films is persistent since many of these devices are used under conditions of thermal variation. The glass transition temperatures are critical parameters to investigate the thermal properties of polymer ultra-thin films.

There have been fewer experimental studies showing the effect of temperature on polymer film properties. Because of the extreme thin thickness, optical methods were often employed for the investigation of polymer thin films. Beaucage et al. invented new method to measure glass transition temperature of polymer thin film in ellipsometric technique in 1993. This method plots the refractive index as a function of temperature. When the thickness was 300nm, the glass transition temperature of polystyrene was 86.4 °C. When the thickness was 350nm, the glass transition temperature of the same polymer was 91.6°C. In 1996, Prucker et al. introduced evanescent wave optics method which measures refractive index as a function of temperature same as ellipsometric study. According to their study, the glass transition temperature of ultra thin film for polymethylmethacrylate was drastically decreased when the thickness reached less than 100 nm. They also concluded that this effect could be found in several different techniques. In 1995 Takahara et al. observed that the

surface glass transition temperature of poly (styrene-block-methyl methacrylate) decreased dramatically as the thickness became thinner. They used temperature dependent X-ray photoelectron spectroscopy. The glass transition temperature of polystyrene phase was decreased down to 65.4 °C when the thickness was about 6 nm, while that of the bulk was 107.5 °C.

Optical methods can observe glass transition phenomena, however, actually real data include considerable errors and always need regression analysis. Usually those data show only slight change at glass transition temperature which produce unreliability for regression analysis. Another problem is optical method only can measure overall properties of total polymers. Although the location to measure can be changed, it is as large scale as several mm to one cm level.

We will apply μ -TA to polymer thin-film, and discuss the results comparing the results from optical methods and conventional thermal analysis.

3. METHODOLOGY

3.1. Scanning Thermal Microscopy

The SThM's ability to probe with a submicron resolution was demonstrated for polymer composites as well as for semiconductor and metal surfaces by several groups (Majumdar et al., 1993; Hammiche et al., 1996). After that, some of works using this technique were done such as the investigation of the buried metal particles in polymer composites (Hammiche et al. 1996), photothermal FTIR analysis based on modified SThM technique (Hammiche et al. 1999), and the detection of phase transformations of various polymer surfaces (Pollock et al., 1998).

3.1.1. Thermal conductivity contrast

Figure 3.1 shows general scheme of the SThM. This scheme employs Wheatston bridge circuit to detect small amount of error current from set point current. Thermal probe is one of the legs of the Wheatston bridge and plays a role of resistive heater. This scheme, which is called thermal feedback loop, detects the error signal from setpoint temperature and tries to compensate the excessive or deficient error. When keeping constant temperature, the heat, which is dissipated from probe to surface, gives information of the thermal conductivity of materials surface.

Changes in the heat flow between the probe and the sample are measured by monitoring the bridge voltage. Actually the heat flow is controlled not only by thermal conductivity of the sample, but also by other factors such as;

- Temperature difference between the probe and the sample
- Contact area of the probe
- Ambient temperature and its condition (such as humidity, vacuum, etc.)

Especially, the contact area of the probe is a significant problem. The contact area of the probe depends on the topography. When thermal probe is located on the top of a bump, the contact area is small, thus heat dissipation between probe and sample surface is smaller. When thermal probe is located on the bottom of the valley, the contact area becomes large, therefore the heat dissipation between probe and surface is larger.

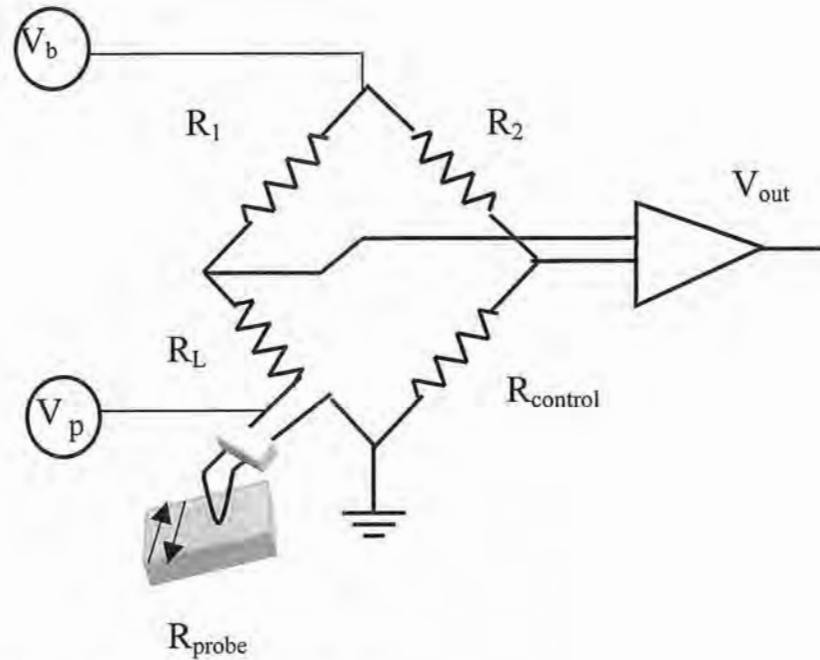


Figure 3.1. Thermal conductivity mode scheme.

Because of these reasons, thermal conductivity contrasts mostly have very similar features. Therefore, we should always take into account this topographical effects for the interpretation of the thermal images .

Probe temperature can be specified by a user. For glass-like polymeric materials, normally the temperature of thermal probe should be below the glass transition temperature to avoid the softening the sample during scanning. For rubber-like materials, we usually use room temperature, however, scanning is unstable because of the compliance.

Using thermal probe, the sum of the laser voltage is about 30 nA. When a thermal tip is contaminated by small debris, it can be cleaned by heating up to 450°C for several seconds. The debris on the thermal probe is sometimes not visible, so another way to recognize the debris and dirt on the tip is to compare the heat dissipation of the probe in the air before and after the measurement. For example, when we set 50°C as a probe temperature before measurement, thermal probe will show 3-5 mW as a heat dissipation. Then after the measurement, we will do same procedure, and then look at the heat dissipation again. If the

heat dissipation is less than the value before the measurement, probably the thermal tip has debris on it.

3.1.2. Scanning thermal microscope probes

The thermal probe consists of cantilever, tip (filament), reflective mirror, and half-moon plate (Figure 3.2) (Topometrix). Cantilever is made of silver wire and it is connected to the tip directly. Tip is made of filament of the Wollaston wire (platinum/10% rhodium alloy). The diameter of the tip is 5 μm with radius curvature about 10 μm . The total length of the thermal probe is close to 3 mm and the spring constant is estimated as approximately 6 N/m (Topometrix, private communication). The very end of the tip is etched to expose the platinum core. Reflective mirror is to reflect the laser to the photodetector. Whole scheme is placed on the half-moon plate which can be attached to the piezo scanner magnetically.

Thermal probe is extremely fragile so that it can be easily damaged and broke or bent. When engaging the thermal tip, the voltage difference between set point and present voltage shown as an internal sensor should be less than 15 nA. Too large voltage difference (loading force) will bend the tip. The sensor response shows the cantilever deflection as a function of the probe position. If the sensor response curve shows linear line with small data distribution, it is ready to go to scanning the surface.

In case thermal tips were damaged, micro-tweezers is employed to fix the shape under optical stereo microscope. The thermal tips purchased from company does not have complete uniform shape. Thus it is very important to examine the tip shape through stereo optical microscope before measurement in order to make sure the tip has reasonable shape. The shape of a thermal probe affect the characteristics of heat dissipation from probe to the surface. Hence, after modification of a thermal probe, the recalibration of thermal property is necessary. Most of the time, this method works well for such troubles, however, a problem of this approach is degradation of mechanical property of the probe. Most likely, the mechanical strength of the thermal probe is not as good as before modification. It is more fragile so that one can not expect to use the probe for a long time.

After overcoming such problem, by treating the probe very delicately, we will obtain quality-data, which are greatly dependable, repeatable, and meaningful.

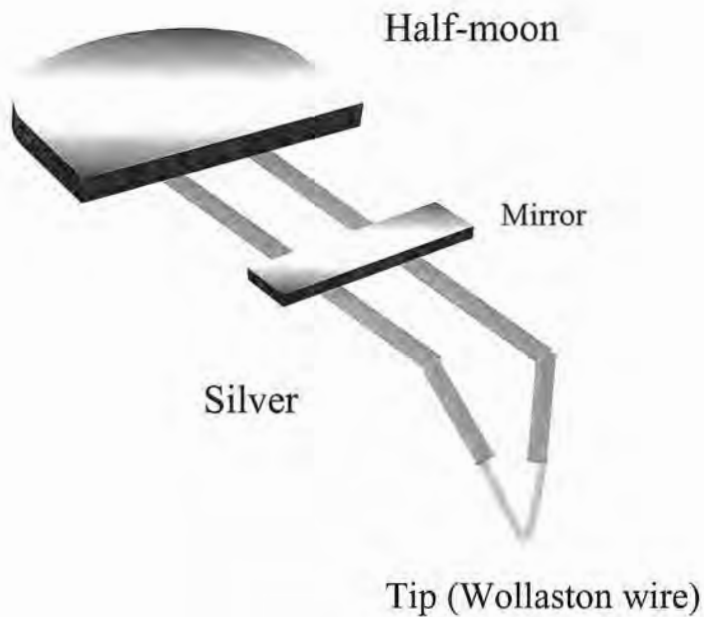


Figure 3.2. MicroThermal probe. Tip is made of filament of the Wollaston wire (platinum/10% rhodium alloy). The diameter of the tip is $5\ \mu\text{m}$ with radius curvature about $10\ \mu\text{m}$. The total length of the thermal probe is close to 3 mm and the spring constant is estimated as approximately 6 N/m (Topometrix, private communication). The very end of the tip is etched to expose the platinum core.

3.1.3. Thermal-distance curve

When a thermal probe approaches to the surface, heat dissipates from the probe to the surface. This heat dissipation, as a function of probe position, during approaching-retracting motion of the thermal probe to the materials surface is called thermal-distance curve. During the measurement of the thermal distance curve, we can obtain force-distance curve simultaneously, which is correlation between probe position and cantilever deflection. We develop the data analysis procedure for thermal-distance curve which will provide the thermal conductivity of the materials surfaces, and simulation of heat flow for variety of materials.

Before measuring the thermal – distance curve, the thermal conductivity contrast may be obtained to find interesting places. Sometimes, thermal conductivity contrast reveals different features as are not seen in topography image. For example, topography can not detect sub-surface materials unless they affects the surface morphology, however, thermal conductivity contrast can detect sub-surface substance because the materials underneath the surface affects the thermal conductivity of the surface materials (Hammiche et al., 1996).

After specifying the location, we can select such parameters as approaching – retracting speed of the thermal probe at several points, time delays, and set point. The approaching – retracting speed of the probe greatly affects the sensitivity of the thermal – distance curve. From our experience, at start point, probe should have high speed to obtain reasonable curve. At sample point, the speed of thermal probe should be as low as possible since high speed of the probe at sample point leads thermal probe very unstable so that oscillation of the probe occurs before its contact to the surface. Set point affects the whole shape and position of thermal – distance curves. Lower set point shifts thermal distance curve to the left side, and higher set point shifts the curve right side.

As for the approaching speed of thermal probe, our condition was as follows;

Feed back point: 100 $\mu\text{m/s}$ Start point :1000 $\mu\text{m/s}$

Sample point: 1 $\mu\text{m/s}$ Pull – back point 100 $\mu\text{m/s}$

3.1.4. The measurement principle and calibration procedure for the localized micro-thermal probing [Gorbunov et al., 2000]

In this section our calculation procedure is described. Microthermal probing operation is primary carried out in the thermal conductivity contrast mode (Figure 3.1). In this scheme, input internal resistance of the operational amplifier, M , is much higher than the resistance of the electric bridge (R_1 , R_2 , R_L , R_C and R_P). As a result, the dependence of bridge voltage, V_b , and probe voltage, V_P , can be described by the equation:

$$V_P = V_b \frac{R_P}{R_P + R_1 + R_L}, \quad [\text{V}]. \quad (1)$$

Therefore, heat loss (dissipation), Q , is directly related to the parameters of the electric circuit as:

$$Q = \frac{V_P^2}{R_P} = V_b^2 \frac{R_P}{(R_P + R_1 + R_L)^2}, [\text{W}] \quad (2)$$

Parameters presented here can be easily measured and, in recent upgrades, are available in the controller software (Topometrix, 1999).

To simplify data analysis, we adopt a spherical approximation and replace the actual sensing loop with a hemi-spherical tip (Figure 3.3). For all practical purposes, this replacement is sufficient. Only when using quite large loading force, and very high magnification, the elliptical shape of the thermal contact is appeared in the image.

The effective tip radius, r , can be calculated from the condition of the equal contact area for the adopted spherical model and actual elliptical shape characterized by two radii:

$$r \approx \sqrt{R_1 \times R_2}, [\text{m}] \quad (3)$$

where R_1 is the radius of the sensing loop and R_2 is the radius of the microwire.

After these preliminary elaborations, we develop the consistent scheme of heat loss (dissipation) calculations for the thermal probe for the given SThM measuring setup. For this, we define the initial position of the thermal probe above the surface as Z_0 (see Figure 3.3) The feedback loop of the control unit keeps a constant temperature of the thermal probe, T_P . The initial temperature of the surface is T_S . The heat transfer per unit area through the tip-surface gap, q , is caused by the temperature gradient between the thermal probe and the surface, $\Delta T = T_P - T_S$. The air gap between the thermal tip and the surface, Z , for all practical measurements, is much less than the probe radius: $Z < r$. This is very typical for usual SThM setup, which is different from traditional AFM scheme. Contact mode AFM nanoprobe has much smaller tip radius curvature so that usually the relationship of Z and r becomes; $Z > r$.

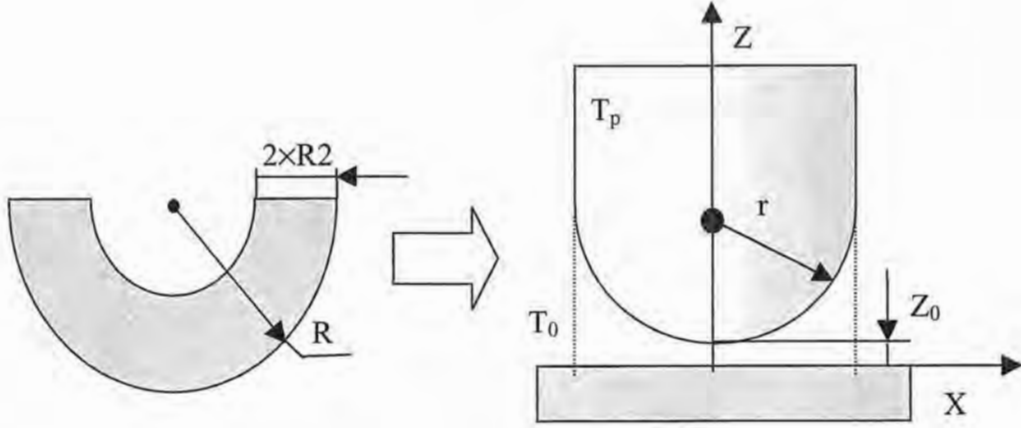


Figure 3.3. The geometry of the thermal sensing loop and hemi-spherical model used in this paper for data processing and modeling.

The radiation transfer between the thermal probe and the surface is estimated from Pt extinction data as being negligible at the temperature explored. We do not take into account the heat convection between probe and surface either. Under these conditions, the heat dissipation between the thermal tip and the surface can be presented in a linearized form:

$$q = \lambda_{air} \cdot gradT \approx \lambda_{air} \cdot \frac{T_p - T_s}{Z}, [W/m^2] \quad (4)$$

where λ_{air} is the air thermal conductivity.

During engaging and disengaging the tip, the tip-surface gap width can be defined via a time-dependent function:

$$Z(t) = Z_0 - v \cdot t, [m] \quad (5)$$

where v is an approaching velocity of the thermal probe and t is the time from the beginning of the approaching motion. During the approaching cycle, the surface temperature rises as:

$$T_s(t) = T_0 + \Delta T(t), [\text{K}] \quad (6)$$

where $\Delta T(t)$ is the temperature gradient that causes the probe heat dissipation.

From the equations (4)-(6), we can determine the integral heat dissipation from the thermal tip, Q , as:

$$Q(t) \approx \lambda_{air} \cdot \pi \cdot r^2 \cdot \frac{T_p - T_0 - \Delta T(t)}{Z_0 - v \cdot t}, [\text{K}] \quad (7)$$

From the thermal-distance data using the equation (7), we can estimate the temperature variation on the surface defined by the equation (2) as :

$$\Delta T(t) = T_p - T_0 - \frac{R_p \cdot V_b^2(t)}{(R_p + R_l + R_L)^2} \cdot \frac{Z_0 - v \cdot t}{\lambda_{air} \cdot \pi \cdot r^2}, [\text{K}] \quad (8)$$

The equations (7) and (8) provide basic relationships between the heat dissipation and the surface temperature and measured experimental data and instrumentation parameters.

3.2. Micro-Thermal Analysis

This technique consists of two modes which are micro-thermomechanical analysis (μ TMA) and micro differential scanning calorimetry (μ DSC). These two data can be obtained simultaneously and the scanning (measurement) time is extremely short compared to conventional thermal analysis due to its high heating rate. Normally it takes 30 seconds to 5 minutes for one measurement. The heating rate varies from 1 C°/sec (60 C°/min) to 25 C°/sec (1500 C°/min). Conventional thermal analysis has mostly 10 C°/min to 100 C°/min as a heating rate, which is much slower than that in μ TA.

3.2.1. Micro-thermal mechanical analysis

The mechanical properties of materials are an essential guide to their suitability for particular usage, and can indicate the history of formation and fabrication of the materials before testing. The molecular nature is most important for mechanical properties, for example, the behavior of plastics is strongly influenced by the thermal history and its chemical structure (Reading et al., 1995).

μ TMA is very similar to conventional TMA. The μ TMA monitors the z - position of the thermal probe under the constant force during increase of temperature.

In conventional TMA, whole entire body of the sample is surrounded by large furnace so that whole body of the sample is heated homogeneously. But in the μ TMA, furnace is substituted by AFM probe (MicroThermal probe), and only the place under the probe will be heated, which means pinpoint heating. Although the instrumentation of μ TA is largely different from that of conventional thermal analysis, the data obtained by these two methods are very similar.

3.2.2. Micro-differential scanning calorimetry

The μ DSC measures the difference of heat dissipation between the probe on sample and reference probe in the air during linear increase of temperature. Same as mentioned in the section above (μ TMA), μ DSC also has much smaller heating area compared to conventional DSC, which means the area under the probe can only be heated. Because heating area is not surrounded by particular space as is seen in conventional DSC, the change of room temperature cause uncertain results.

Sample probe and reference probe are heated in same heating rate during measurement. Both probes should have similar thermal properties.

3.2.3. Experimental procedure (simultaneous measurement of μ DSC & μ TMA)

In μ TA measurement, we use a couple of thermal probes. Both probes should have similar thermal properties and electric properties to obtain best results. In μ DSC measurement, we measure the difference of heat dissipation between sample probe and reference probe, thus, similar couple of probes is very important. The resistance of a probe is

within 1-3 Ω . Resistance of a probe is measured by multimeter. After finding probes which has similar resistance, we have to measure the heat dissipation in specific temperature such as 50°C. Typical heat dissipation value when probe is 50 °C is about 3 mW. If these values are also close each other, we can use these probes for measurement.

Anywhere on the screen can be chosen as a measurement point. Before measuring the μ TA, to scan the image of scanning thermal microscopy (SThM) or thermal conductivity contrast is recommended in order to find interesting place, although μ TA measurement can be done without scanning the SThM image.

Measuring the baseline is one of the most important processes for the μ DSC. During the baseline measurement, the difference of heat dissipation between sample probe and reference probe is monitored as a function of temperature. When taking the baseline, both of the probes should be in the air and temperature range should start below room temperature such as 0 °C to a final temperature such as beyond the glass transition temperature, or melting temperature. Thermal feedback loop works above room temperature, so if temperature increase starts from 0 °C, at room temperature, thermogram shows sharp kick-in phenomenon. Usually baselines show linear curve with kick-in phenomenon since there are some differences of properties between two probes such as thermal conductivity and mechanical properties.

Once the curve (baseline) were obtained, it will be always used to subtract from original data.

To calibrate the probe temperature, a set of polymeric materials whose glass transition temperature and melting temperature are known, such as polystyrene ($T_g=100^\circ C$) and polyethylene terephthalate ($T_m=260^\circ C$). Including the room temperature's kicking-in, these three points are used for temperature calibration of thermal probe. Since these temperatures are already known, if instrument showed different temperature at those temperatures, we should correct them and obtain new calibration files.

After completing these processes, μ TA measurement can get started. There are some parameters we should set in, such as temperature heating rate and cooling rate, temperature range, set point, and location. Optimal heating rate is between 5 to 10 °C/s. Depending on purpose, the heating and cooling rate for one measurement can be programmed.

After the measurement, because mostly the temperature of thermal probe goes up to more than melting temperature, the end of the probe is attached with debris of polymeric materials. So after disengaging, the thermal probe may be cleaned by heating up to 450 °C for several seconds. That will burn those trashes up. Sometimes burning debris up provides the flush light of the very end of the tip. If the tip was attached to the surface quite strongly, the tip might be bent during disengaging. Tip bent can be fixed by micro-tweezers under optical stereo microscope.

Data analysis is done with the software called universal analysis. At the glass transition and melting temperature, thermograms show sharp drop down. The extrapolation linear curves from thermogram before and after such phenomena make a intersection, which is defined as onset point (Haines, 1995). Using this onset-method, we determine the glass transition temperature and melting temperature. Several curves are put together in one plot for comparison. When having several thermograms with different heating rate, this works very well. Anywhere on thermograms can be zoomed in, and a user can see the slight shift of the peaks.

4. EXPERIMENTAL SPECIFICS, RESULTS AND DISCUSSIONS, AND CONCLUSIONS

4.1. Microthermal Probing by Scanning Thermal Microscopy

4.1.1. Experimental

The samples for investigation were selected to represent materials with a wide range of surface thermal properties (Gorbunov et al, 1999). Thermal properties of these materials taken from databases of MatWeb, MEMS Materials Database, CenBASF/Materials and from Tong (1994) are presented in Table I. Polymer samples were received from Bayer, Fluka, Jenssen Chimica, and Aldrich. Smooth polymer films with several hundred-micrometer thicknesses were prepared by solution-casting technique.

Thin films (250 μm) of Pt and Au were purchased from Goldsmith. The surface topography for all samples were characterized prior to thermal measurements and observed to be smooth and homogeneous. The average microroughness within 1 μm x 1 μm area did not exceed 5 nm.

For microthermal measurements, an Explorer SPM microscope (Topometrix) with an SThM controller was exploited. The thermal probes were 90%Pt-10%Rh thermoresistors with the microwire diameter of 1 μm and the sensing loop diameter of 20 μm . The approaching-retracting mode was used to collect the force-distance data concurrently with the thermal signal (current through the probe)-distance data beginning from several micrometers above the surface. The temperature of the thermal probe was kept constant by the electronic feedback. The sets of the thermal data for each material within the temperature interval from 35°C to 80°C were collected. To calculate the heat dissipation on the thermal probe, a combination of measured voltages within the electric bridge along with the calibration procedure similarly to a scheme proposed in Hammiche et al (1996) were used. After this, the heat dissipation on the thermal probe from the equation (2) was calculated and the surface temperature gradient according to the methodology presented above (equation (8)) was estimated.

Table I. The parameters of mechanical and thermal properties for delegation materials.*

materials	Poisson ratio	Young's modulus, GPa	λ , $\text{W m}^{-1}\text{K}^{-1}$	α , 10^{-8} , m^2s^{-1}	$\Delta Q/\Delta T$, 10^{-5} , WK^{-1}
polystyrene (PS)	0.38	3.0	0.142	7.52	1.0
polyurethane (PU)	0.49	0.44	0.147	8.91	1.04
polypropylene (PP)	0.43	1.9	0.18	9.47	0.91
poly(methyl methacrylate)(PMMA)	0.4	3.2	0.19	11.77	0.83
poly(vinyl chloride) (PVC)	0.42	2.5	0.21	14.93	0.96
polyethylene (PEHD)	0.49	0.88	0.37	17.52	1.30
glass	0.23	60.0	1.6	67.34	1.26
silicon nitride	0.25	385.0	19.0	863.24	1.26
graphite	NA	4.8	24.0	1543.66	1.56
platinum	0.39	171.0	71.0	2507.59	1.87
silicon	0.27	112.4	156.0	9394.33	2.0
gold	0.42	78.0	317.0	12830.60	2.30
air	-	-	0.024	18.4	- ¹

*Data are taken from Tong (1994) and Internet databases of MatWeb, MEMS Materials Database, CenBASf/Materials.

Here, major experimental conditions and limitations for the SThM probing are listed. Some practical advices are aimed on helping to find optimal measurement parameters. The main conditions for microthermal measurements with SThM technique are:

- To get stable imaging and force/thermal signal-distance data, it is necessary to scan the surface by the same thermal probe prior to the thermal measurement and repeat approaching-retracting probing several times before data collection.

- The thermal probes are not rigid beams and are the subject of thermally induced deformations. Vertical and, occasionally, torsional, deflections are observed at elevated temperatures. The thermal probes need prior “warm-up” (heating-cooling cycling before actual measurements) that leads to more predictable thermal deflections. Careful selection of “twin” thermal tips is a key issue for the high-resolution differential measurement in differential thermal analysis (μ DSC) regime (Song M. et al., 1999; Reading M et al., 1999). The criteria for the selection are very close resistivities and similar deflection behavior at higher temperatures.
- For the measurement of composite materials and complicated geometrical objects, a hand made microstage is a crucial tool. In order to control engagement process, our microstage is designed to have independent stand-alone legs and stage.
- A critical parameter for a quality thermal-distance measurement is the probe velocity and a set point. Significant noise and auto-accelerated oscillations can occur due to the feedback loop intrusion that can completely mask actual thermal data if these parameters are not optimized.
- The room temperature can play a critical role in the thermal measurements and calculations especially at the lowest probe temperature. The lowest practical probe temperature is 30-35°C at room temperature close to 20 °C. The best solution (and maybe the only solution for samples with a low melting temperature) is to keep constant and low surrounding temperature by having the SPM scanner isolated in an environmental chamber with and external temperature control. In some case, thermal scanning was conducted in a refrigerator.
- If the sensor loop is deformed as a result of exceeding forces during engagement (it happens from time to time), it is fixed by microtweezers under a stereomicroscope and check again the resistivity and the deflection behavior, however, after this procedure, the characteristics of original thermal probe is usually changed so that the probe should be calibrated again and whole entire measurement must be repeated again.

Additional important technical parameters of thermal measurements are presented below:

- The probe velocity is in the range from 1 to 10 μm ;
- Starting position of the thermal probe is 1 to 3 μm above a surface;
- Collection time per single data-point is 10^{-2} seconds;
- The frequency of approaching-retracting cycle is in the range 0.1-5Hz.
- The effective radius of the thermal probe is calculated to be 4.5 μm .

From the experimental data, the heat dissipation according to the equation (2) for the thermal tip in direct physical contact, Q_c , and far from the surface, Q_0 , were calculated. The applicability of the relationship between the difference in these heat dissipations, $\Delta Q = Q_c - Q_0$, and the temperature difference of the probe, T_p , and the surface, T_s , in the form:

$$\frac{\Delta Q}{\Delta T} = \frac{Q_c - Q_0}{T_p - T_s} = \frac{3}{4} \pi \lambda R_c, \left[\frac{W}{K} \right] \quad (9)$$

where R_c is the effective thermal contact radius and λ is the generalized thermal conductivity, defined as $\frac{2}{\lambda} = \frac{1}{\lambda_p} + \frac{1}{\lambda_s}$, where λ_p and λ_s are the thermal conductivities of the thermal probe and the surface, respectively (Haritonov et al., 1997). This relationship is derived from the Blok relationship (Blok, 1937) that holds for steady flow conditions of the heat transfer process with paraboloidal distribution flow from the round surface. These conditions are satisfied for our measurements.

4.1.2. Results and discussion

To test the sensitivity of our SThM instrumentation, we recorded thermal images of 16 μm x 16 μm grids composed of silicon substrate ($\lambda = 156 \text{ W m}^{-1} \text{ K}^{-1}$) coated with a thin (200 nm) silicon oxide layer ($\lambda = 1.6 \text{ W m}^{-1} \text{ K}^{-1}$) (Figure 4.1). As we observed, for these materials with very different thermal conductivities, an excellent thermal contrast is achieved for a wide range of probing parameters. The resolution of topography image is sub-micron.

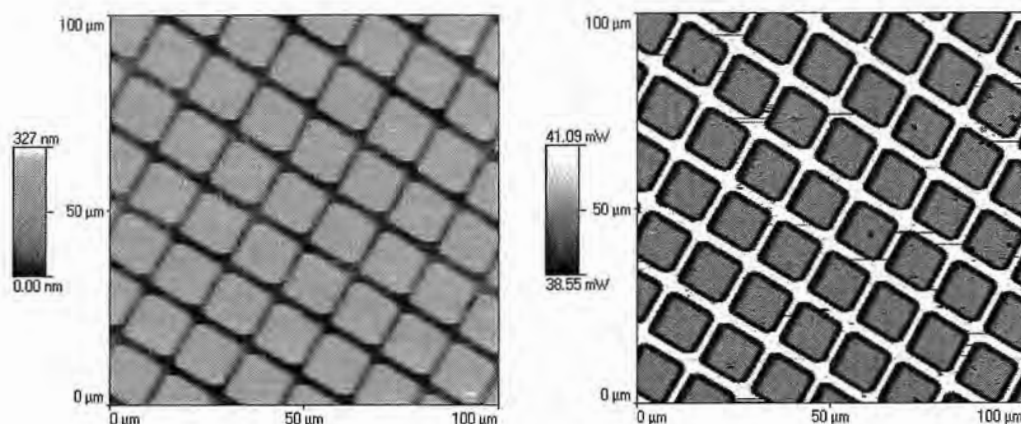


Figure 4.1. The topographical (left) and thermal (right) images of grids composed of silicon coated with a thin silicon oxide layer with periodicity $16\ \mu\text{m} \times 16\ \mu\text{m}$.

In the left figure, lower area like background corresponds to the silicon and each square island is silicon dioxide film. From right figure, it is clear silicon substrates showed much higher thermal conductivity than silicon oxide island. The thermal lateral resolution is estimated from the sharpness of the edges of silicon oxide grid on thermal images as being in the range 50 - 200 nm.

For all samples studied here, the similar thermal behaviors of the probe during the approaching-retracting cycle were observed. Selected thermal/force-distance data for platinum, silicon, glass and high-density polyethylene samples are presented in Figure 4.1. The thermal signal increases very modestly during the approaching cycle for large distances between the thermal tip and surfaces, rises faster when the thermal tip is very close to the surface (tens-hundred nanometers), and is a subject of sharp changes at the point of the physical contact. The thermal signal is virtually constant after the physical contact is reached (Figure 4.2).

Obviously, this behavior reflects rising heat dissipation of the thermal probe due to the thinning gap between the thermal probe and the heat sink represented by the solid surface (Gorbunov et al., 1999). Similarities in the thermal behavior for all samples at large distances are due to virtually identical environmental conditions for the thermal probe in air and far from the surface ($>2\ \mu\text{m}$).

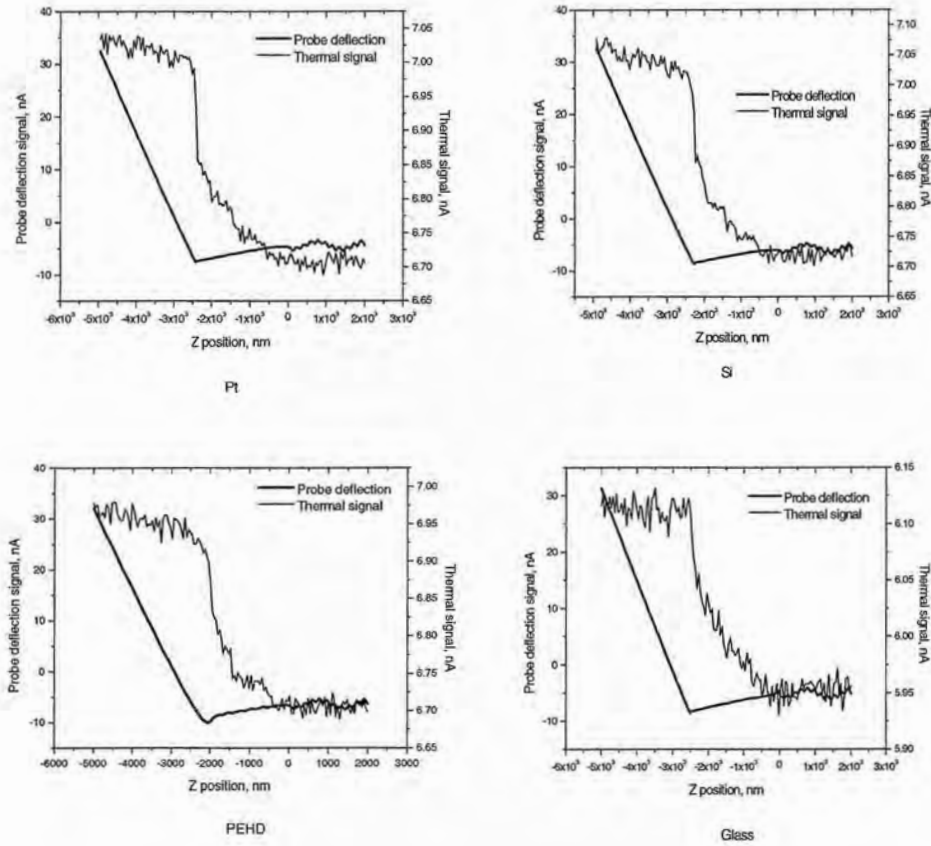


Figure 4.2. Thermal signal and probe deflection versus tip-surface distance during approaching cycle for platinum, silicon, glass, and PEHD samples. The approaching velocities are 5 μm and the probe temperature is 70 $^{\circ}\text{C}$.

However, the thermal behavior of the thermal probe in the vicinity of the direct physical contact is very different for surfaces with different thermal conductivities. The thermal signal-distance data were collected with the preheated thermal probe for various surfaces with large difference in thermal properties (Table I). Examples for very low conductive and very high conductive surfaces are presented in Figure 4.3. For the surface with the high thermal conductivity (gold), a sharp jump in the thermal signal occurs at the physical contact.

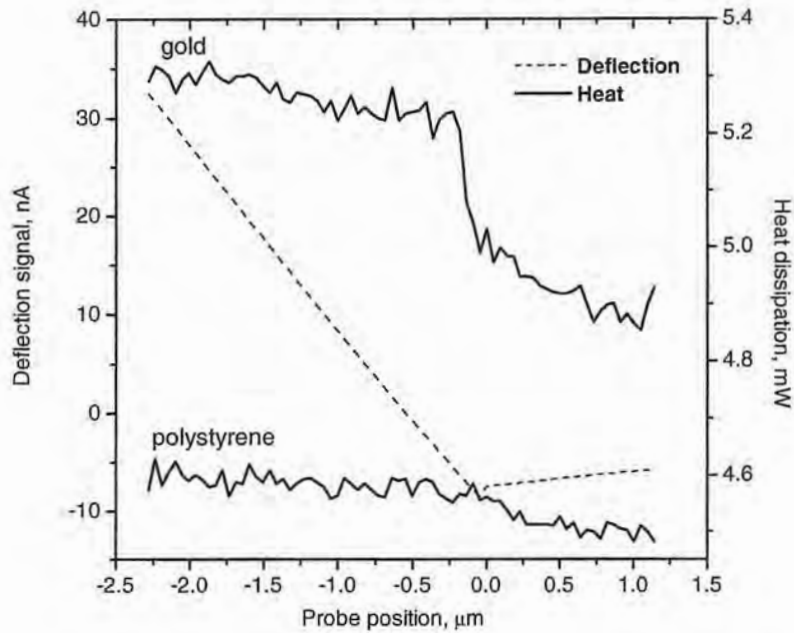


Figure 4.3. The heat dissipation versus tip-surface distance calculated from the experimental data for gold and polystyrene surfaces along with the force-distance curve; the initial probe temperature is 40°C.

In contrast, for the surface with low thermal conductivity (polystyrene), a very gradual increase in the thermal signal up to the physical contact point is observed with only slight increase after the physical contact. Apparently, this difference is caused by very different abilities to dissipate heat by metal and polymer surfaces.

Using the equations (2) and the experimental thermal data for different probe temperatures and different approaching velocities, the probe heat dissipation versus the gap variation up to the direct physical contact (zero gap width) was calculated. These variations were calculated from the experimental data for the highly thermally conductive surface (gold) and the low thermally conductive surface (polystyrene). Figure 4.4 demonstrates the data derived from experimental runs where the probe temperature was selected to be 80 °C and approaching velocities of the thermal probe were 1 $\mu\text{m/s}$ and 5 $\mu\text{m/s}$.

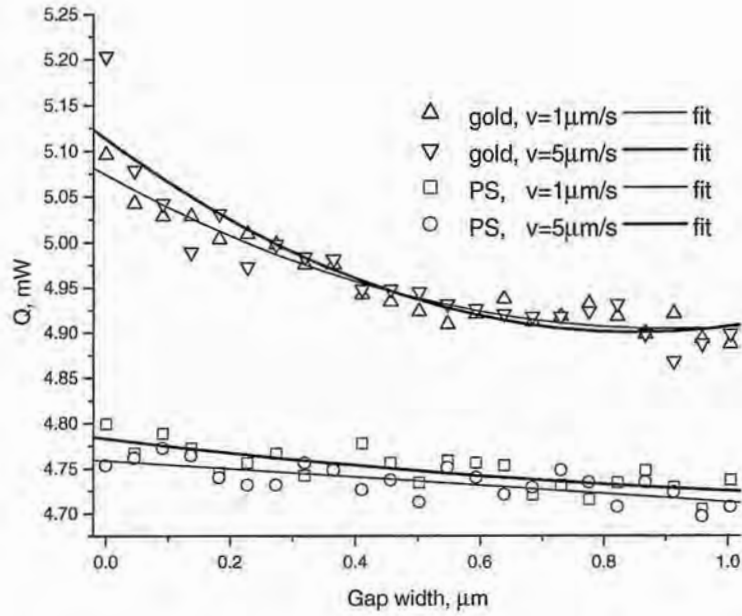


Figure 4.4. The probe heat dissipation versus tip-surface gap width calculated from experimental data for gold and polystyrene at two approaching velocities; initial probe temperature is 80°C.

As clear from these experimental results, the absolute level of the heat dissipation was much higher for a higher probe temperature. The tip velocity affected very lightly the level of the probe heat dissipation in the presence of both surfaces.

As can be seen from these plots, the variation of the heat dissipation versus tip-surface distance was very different for metals and polymers. For the gold surface, a significant rise of the heat dissipation was observed in the vicinity of surface (the gap width less than 0.2 μm). This effect was much more pronounced for a higher probe temperature, however, for the polystyrene surface, the heat dissipation was virtually constant in a whole range of tip-surface distances (Figure 4.3). Slight increase of the probe heat dissipation in the vicinity of the surface was noticed only at a high probe temperature.

From this experimental data, the temperature gradient on both surfaces beneath the thermal tip was calculated by using the equation (8) (Figure 4.5).

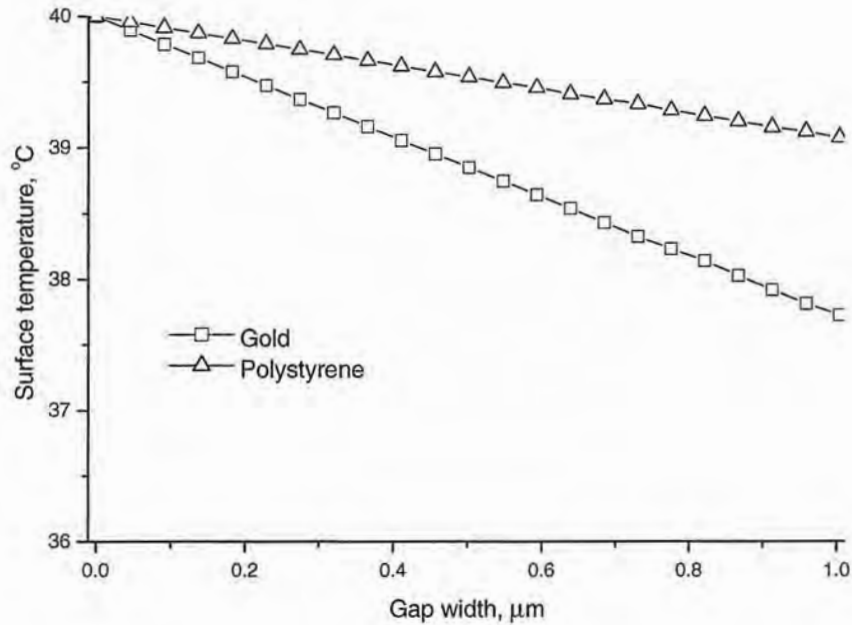


Figure 4.5. The surface temperature versus the tip-surface gap calculated from experimental data for polystyrene and gold surfaces; the initial probe temperature is 40°C .

These variations were calculated for gold and polystyrene samples from the experimental data for the initial probe temperature of 40°C and the approaching velocity of $1 \mu\text{m/s}$. As clear from these data, the surface temperature for polystyrene surface approached 40°C even when the pre-heated thermal probe was located on the largest distance from the surface ($1 \mu\text{m}$). Very small increase of the surface temperature was observed during the thermal tip approaching the surface. In contrast, the surface temperature of the gold surface initially stabilized at a lower temperature for the gap width of $1 \mu\text{m}$ and gradually increased to 40°C during the approaching cycle.

Obviously, this behavior reflects very different scenarios of the heat dissipation dynamics. In the case of very poorly conductive surface, the heat flow from the pre-heated tip located at large distance is capable of rising the surface temperature because of extremely low rate of the heat dissipation from the polymer surface to inner bulk material. On the other hand, highly conductive surface dissipates a fraction of the heat flow from the thermal tip,

thus, keeping its current temperature below the tip temperature. Only decreasing tip-surface gap width results in gradual rise of the surface temperature that approaches the tip temperature at the tip-surface gap width less than 200 nm.

As a next step, how the heat dissipation, ΔQ , behaves for different initial temperature gradients between the thermal tip and the surface, ΔT , was studied. According to the equation (9), the heat dissipation should increase linearly with the temperature gradient for any given surface, with a slope, proportional to the product λR_c . The ΔQ for different surfaces in the range of temperatures of the thermal probe from 40°C to 80°C was tested. Indeed, for all surfaces studied here, we observed virtually linear variation of ΔQ with ΔT for $\Delta T > 10$ °C as demonstrated in Figure 4.6 for polystyrene surface. Therefore, the equation (9) was verified to be correct for the variety of surfaces and, thus, can be used for the calibration procedure as will be described in chapter 4.2.

Finally, based on the recent μ DSC development that allows the variation of the thermal probe temperature after the thermal tip engagement, another approach was attempted. In this case, the direct measurement of the heat dissipation versus temperature was possible with instantly changing the temperature of the thermal probe (Pollock et al., 1996; Reading et al., 1999). This alternative approach was tested for several polymer surfaces (see an example for polystyrene surface in Figure 4.6) and the slope of the thermal signal within the temperature interval outside of phase transformations (e. g., glass transition temperature at 100 °C for polystyrene) was confirmed to correlate fairly well with the surface thermal conductivity indeed.

From the whole experiments described above, we confirmed that μ -TA system is possible to analyze our physical model approach fairly well.

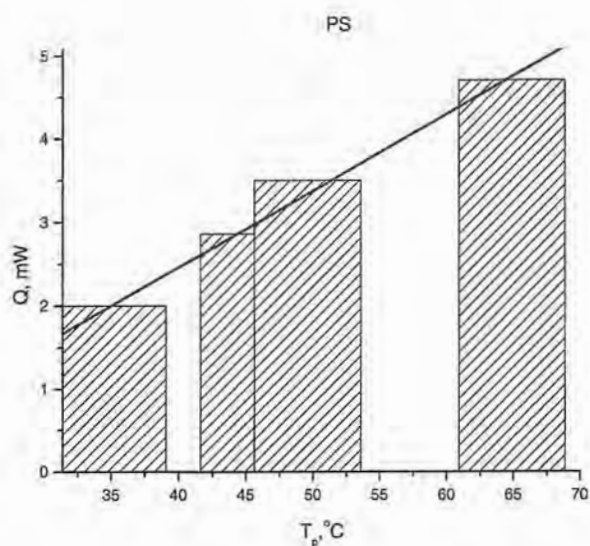


Figure 4.6. The variation of ΔQ versus ΔT as calculated from experimental data for polystyrene surface and corresponding linear approximation.

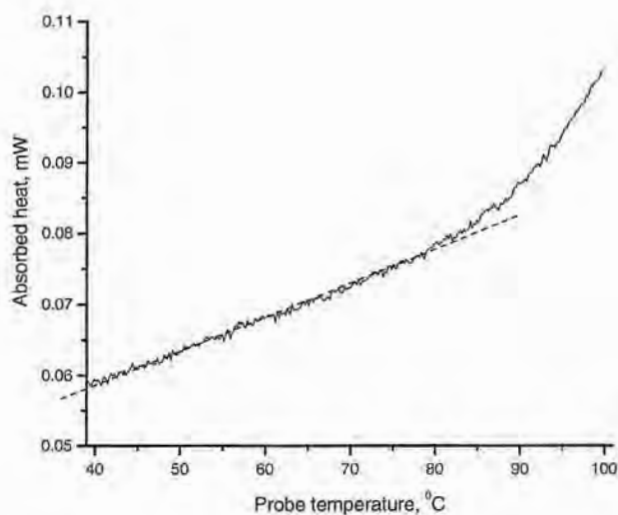


Figure 4.7. μ DSC thermogram for the polystyrene surface with a linear approximation of the thermal signal within the temperature interval between room temperature and glass transition temperature. The slope correlates with the surface thermal conductivity according to the equation (9).

4.2. Microthermal Analysis with Scanning Thermal Microscopy, Calibration

4.2.1. Surface thermal conductivity

The equation (9) shows that a linear relationship should exist between the experimentally measured ratio $\Delta Q/\Delta T$ and the surface thermal conductivity, λ_s . In fact, this relationship is observed experimentally for a variety of materials studied (Figures 4.6 and 4.7). The equation (9) can be presented in a different way, which is more suitable for the calibration procedure:

$$\frac{\lambda_p}{\lambda_s} = \frac{3}{4} \lambda_p \pi R_c \frac{\Delta T}{\Delta Q} - 1 \quad (10)$$

where λ_p is the thermal conductivity of the thermal probe and R_c is the effective radius of the thermal contact.

In the framework of the approach, the thermal conductivity is used in a combination λ_p/λ_s as a dimensionless reference parameter taken from the literature (Table I). The measured and reference parameters are combined as $\frac{3}{4} \lambda_p \pi R_c \frac{\Delta T}{\Delta Q}$ for the straightforward regression analysis and the establishment of the relationship between the measured value of $\frac{\Delta T}{\Delta Q}$ and the known values of λ_s . This approach can be applied to various materials only if the effective thermal radius, R_c , is constant for all surfaces studied, however, the area of the thermal contact is directly proportional to the area of mechanical contact that depends upon surface elastic properties. Therefore, the renormalization procedure that takes into account possible variations of the area of the contact for different surfaces is used here. During all measurements the approaching velocity and set-point voltage of the thermal probe was kept constant.

The variation of the radius of the contact area can be estimated using the Hertzian model of elastic mechanical contact (Johnson, 1998). This model assumes reversible elastic deformation in the contact area and negligible adhesion and was proven to be a reasonable approximation for the scanning probe microscopic measurements with a modest level of

normal loads (Chizhik et al., 1998; Burnham et al., 1990). The model provides the expression for the ratio of contact radii for two surfaces with different elastic moduli. To take into account this variation, the contact radius for a silicon surface as the reference radius, R_{cSi} , and calculate the reduced contact radius, R_c , for other materials using the Hertz approximation ratio (Tsukruk et al., 2000; Tsukruk et al., 1998; Chizhik et al., 1998).

$$\frac{R_{cSi}}{R_c} \approx \left(\frac{E}{E_{Si}} \right)^{\frac{1}{3}} \quad (11)$$

Therefore, if the thermal data for various surfaces are obtained under the identical normal load (the same set-point), the contact radius varies according to the relationship (11). For these estimations, the mechanical properties of tested materials as presented in Table 1 is used.

Complete analysis of our experimental data by using equations (10) and (11) is presented in Figure 4.8. Here, each data point represents the average value for a given surface obtained at several (3-5) locations and several (3-4) tip temperatures. Taking into account a very wide range of materials property combinations (elastic modulus and thermal conductivity), the agreement with the equation (10) that predicts a linear correlation, is excellent. For a given thermal tip and identical normal load, this type of plot is, indeed, a calibration plot that allows the direct measurement of the surface thermal conductivity of unknown materials. This plot provides a means for a straight evaluation of the thermal conductivity by measuring the ratio $\Delta T/\Delta Q$ under the same normal load and within the same temperature interval. The accuracy of such measurements is estimated to be within 30% if surfaces are relatively smooth and topographical contribution is negligible. This represents the typical standard deviation of multiple thermal probing as estimated from surface histograms.

Obviously, the serious drawbacks of this approach is a very time-consuming procedure that requires the collection of a large array of data the variety of surfaces, however, this type of complete analysis is not required for practical measurements. It is critical only to prove that, despite all assumptions and limitations, the relationship (1) holds

for various surfaces and different temperatures on a microscale. For practical purposes, it is sufficient to make concurrent measurements of an unknown surface and a reference surface with an identical thermal tip under conditions discussed above. Measurements should be repeated at several locations and temperatures and averaged over at least 5-10 independent probing. The selection of the reference sample is critical. A general recommendation is to select several reference samples to be used as counterparts for different materials with a combination of elastic and thermal properties neither very close nor very far from assumed/tested parameters of the surface studied. After initial studies, the actual measurement of the surface thermal conductivity takes several hours, however, if elastic properties of a surface are not known, additional micromechanical measurements are required.

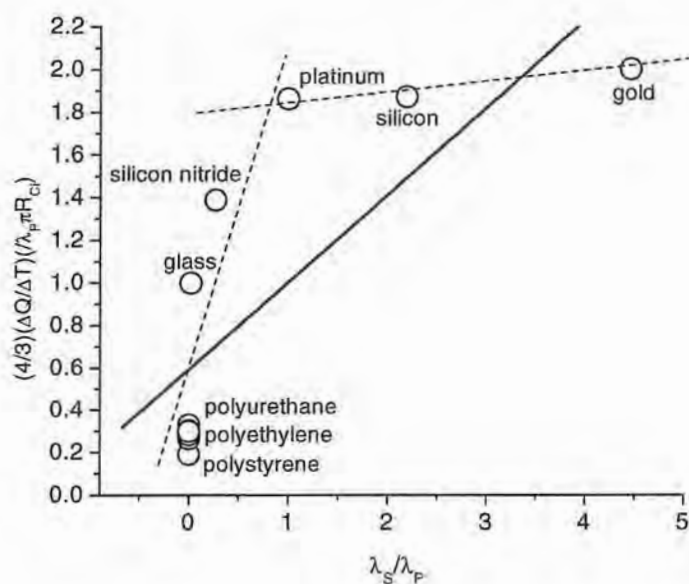


Figure 4.8. The thermal conductivity versus probe heat dissipation using various materials.

4.2.2. Simulations of thermal behavior

The heat transfer and the surface temperature variation as a function of the gap width between the approaching thermal tip and two different surfaces were calculated (Figures 4.9 and 4.10) using the model developed by Gorbunov et al. at 2000. In this simulation, the parameters were chosen from real experimental setup as described in chapter 4.1. Materials properties were employed from Table I. Gold and polystyrene were chosen to represent high and low thermally conductive materials respectively. (gold: $\rho=19,320 \text{ kg/m}^3$, $\lambda=318 \text{ W/m-K}$, $c=132 \text{ W/kg-K}$, polystyrene: : $\rho=1,050 \text{ kg/m}^3$, $\lambda=0.142 \text{ W/m-K}$, $c=1,800 \text{ W/kg-K}$). Approaching velocities of the thermal probe were selected to be $1 \text{ }\mu\text{m/s}$ and $5 \text{ }\mu\text{m/s}$, the initial surface temperature was 20° , and the probe temperature was kept constant and equal to 40°C . All parameters represented typical experimental values used for actual measurements (see chapter 4.1). The initial gap width was selected to be $10\mu\text{m}$ that included typical experimental thermal probe-surface distance ($<2 \text{ }\mu\text{m}$). Simulations for smaller initial gap widths followed the same trends.

As clear from the analysis of the simulated data, the thermal probe heat dissipation should behave very differently for high and poor thermally conductive surfaces. For polystyrene surface with very low thermal conductivity, the heat dissipation is virtually constant over the entire range of gap widths and depends very little on the probe velocity except some overall increase of the heat dissipation level at higher velocities (Figure 4.9). In contrast, for gold surfaces, the heat dissipation increases significantly when the thermal probe approaches the surface. Higher probe velocity significantly raises the level of the heat dissipation in the vicinity to the gold surface. These trends are similar to the thermal behavior observed experimentally in chapter 4.1 except the difference in an absolute level of the heat dissipation. Much higher overall level of the heat dissipation observed experimentally is due to the fact that, in practical measurements, a whole microwire serves as the dissipating sink. In our modeling, the heat flow only from the very end of the thermal probe presented by a hemi-microsphere was simulated. The heat dissipation from the whole sensing loop cannot be taken into account in our calculations.

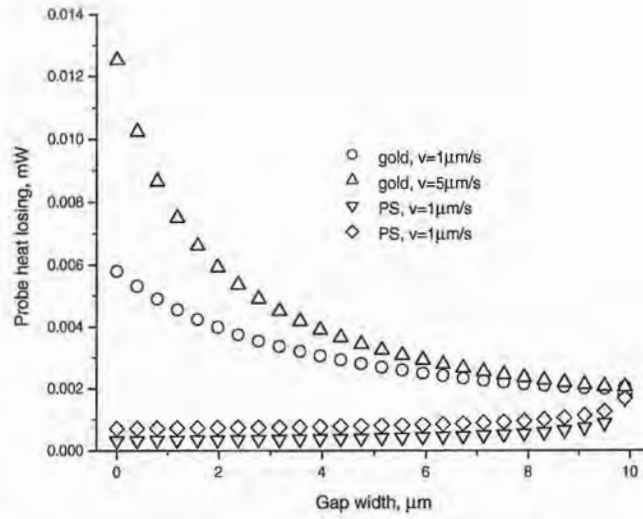


Figure 4.9. The simulation of the heat dissipation of the thermal probe versus the tip-surface gap width between the thermal probe and gold or polystyrene surfaces. The initial gap width is 10 μm and two probe velocities are 1 $\mu\text{m}/\text{sec}$ and 5 $\mu\text{m}/\text{sec}$.

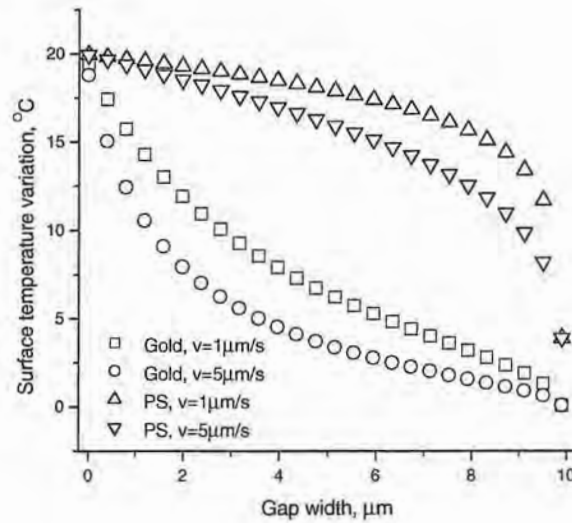


Figure 4.10. The simulation of the surface temperature variation versus the tip-surface gap width between the thermal probe and gold or polystyrene surfaces. The initial gap width is 10 μm and two probe velocities are 1 $\mu\text{m}/\text{sec}$ and 5 $\mu\text{m}/\text{sec}$.

Since the rest of the sensing loop, besides the very end, is located very far from the surface, its contribution varied very insignificantly during approaching-retracting motion and constituted virtually constant thermal “background”.

The heat dissipation behavior becomes clear after the evaluation of the surface temperature variation in the heated zone (Figure 4.10). For polystyrene surface, turning in the heat source with temperature 40°C located at the distance 10 μm leads to immediate rise of the surface temperature by 10 °C followed by the gradual temperature rise to the level very close to the probe temperature for the gap width less than 2 μm . The surface temperature difference between the thermal tip and the surface immediately before the physical contact is less than 0.1 °C.

In contrast, the surface temperature of gold is affected in much lesser extent and remains virtually unchanged for the gap width larger than 5 μm (Figure 4.10). Significant increase of the surface temperature is observed only in the very proximity of the probe to the surface. Even under these conditions, the final surface temperature immediately preceding physical contact is 1-3 °C below the probe temperature. Similar thermal behavior is observed for higher probe velocity with more gradual variation of the polystyrene surface temperature and more steep increase of the gold surface temperature for smaller probe-surface distances (Figure 4.10).

Different surface temperature behavior revealed by our simulations is, obviously, caused by very different thermal conductivities of different surfaces. Fast initial surface temperature increase for polystyrene is due to the fast saturation of its ability to dissipate the heat flow by passing exceeding heat to underlying bulk material. Therefore, very soon after the beginning of the approaching motion, the thermal probe and PS surface become virtually equally heated. As a result, the level of the heat transfer between two surfaces with close temperatures reduces to a very low level. The same reason should lead to very low, in any, jump in the heat dissipation at the point of the actual physical contact. On the other hand, high thermal conductivity of gold surface provides a means for a fast transfer of the heat from surface layer to the bulk material that helps keeping the surface temperature well below

the temperature of the approaching thermal probe. Only at a very small probe-surface distances, the heat transfer from the approaching tip overwhelms the heat dissipation ability of the gold surface that results in its temperature rise, however, even under these conditions, the temperature gradient in the vicinity of physical contact is still significant to give a sharp rise of the probe heat dissipation at very small gap width and physical contact itself.

These conclusions match greatly match the experimental observations for various materials as discussed in chapter 4.1 (see Figures 4.3 – 4.5). For example, for all polymer surfaces with low thermal conductivity, a very gradual increase in the heat dissipation up to the contact point is observed without any abrupt changes during physical contact. On the contrary, all metal surfaces show both significant increase of the heat dissipation for small probe-surface distances and a sharp jump in heat dissipation at the actual physical contact. The surface temperature variation does also confirm simulated behavior (compare Figures 4.5, 4.9, and 4.10).

Some additional observations can be made for the simulations of the heat dissipation at smaller probe-surface distances and for a wider range of probe velocities. To examine the probe velocity dependence of surface temperature variation, the probe velocities from 0.01 $\mu\text{m/s}$ to 1000.0 $\mu\text{m/s}$ were employed using gold (Figure 4.11) and polystyrene (Figure 4.12) for simulation. Although the probe velocity of 1000 $\mu\text{m/s}$ is close to the limits of the quasi-steady heat transfer process for some surfaces, these plots are a good illustration of general trends. The result of the simulation demonstrates that the approaching velocity determines the final surface temperature right before the physical contact. The difference in surface temperatures between the thermal probe and gold surface increases from 0.5 $^{\circ}\text{C}$ to 17.5 $^{\circ}\text{C}$ for velocity increasing from 0.01 $\mu\text{m/s}$ to 1000.0 $\mu\text{m/s}$ and initial temperature gradient of 20 $^{\circ}\text{C}$ (Figure 4.11). The temperature difference for polymeric surface increases from 0.1 to 2.5 $^{\circ}\text{C}$ in the same velocity range (Figure 4.12).

Some additional conclusions can be made from simulations, which go beyond our experimental observations and can be important for other practical considerations. One conclusion is that the increasing probe velocity can be recommended as a means for higher sensitivity of the microthermal probing in approaching-retracting mode due to lesser surface “pre-heating” contribution and higher jump in the heat dissipation at the contact point.

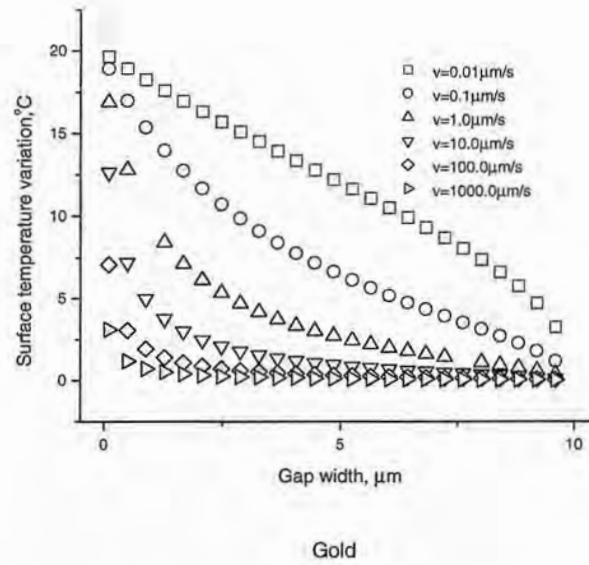


Figure 4.11. The simulation of the surface temperature of gold versus the tip-surface gap width between the thermal probe and gold.

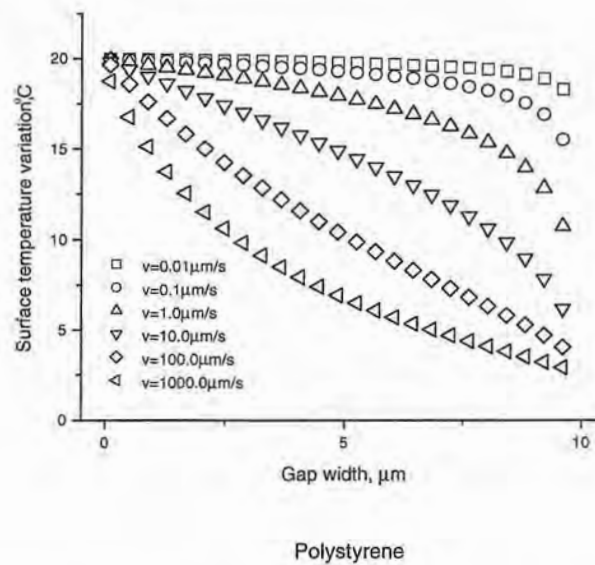


Figure 4.12. The simulation of the surface temperature of polystyrene versus the tip-surface gap width between the thermal probe and polystyrene.

Second, if the probe heat dissipation during the microthermal probing is used to detect phases with different thermal conductivities in composite materials, the increasing probe velocity can significantly increase the thermal gradient on the surface and, thus, enhance thermal contrast. Third, the difference in the probe heat dissipation is so significant that even “non-contact” microthermal probing with the thermal tip not touching surface can provide enough thermal “contrast” to identify different surfaces.

Low probe velocity can significantly reduce the thermal resolution and completely suppress meaningful data. The probe velocity below $0.5\ \mu\text{m/s}$ should be avoided especially for poor thermally conductive surfaces. On the other hand, higher probe velocity results in higher thermal sensitivity for any kind of a surface. A very high probe velocity can lead to superior thermal response and sensitivity. This regime can be realized through temperature/probe modulation mode in the kHz frequency range, however, one should remember that under these conditions, quantitative correlations and relationships for the evaluation of the thermal conductivity (see equation (10)) could be violated due to highly non-linear, non-steady heat transfer process.

Finally the dynamics of the surface temperature variation was tested since any practical measurements should include extended pre-heating time and “warm-ups” to get meaningful results. Figure 4.13 displays time-dependent surface temperature for PS, PEHD, and gold surfaces under stationary probe at the probe-surface distance of $10\ \mu\text{m}$ after turning in its temperature (40°C). As clear from these plots, the initial rise of the surface temperature occurs very fast, however, significant temperature gradient of $2\text{--}4^\circ\text{C}$ for polymers and $16\text{--}18^\circ\text{C}$ for metals is observed even at very long expose times exceeding 100 seconds for polymers and 10,000 seconds for metals. This result indicates that a reasonably short tuning period before the actual measurements would not prevent meaningful microthermal probing, however, caution should be exercised during “pre-probing” period to assure that complete thermal relaxation does not take place.

4.2.3. Conclusions

We proposed the calibration procedure for the evaluation of the thermal conductivity of various surfaces with SThM microprobing. The approach proposed is based on the theory of the steady heat transfer between the thermal tip and the surface. In fact, we observed that a linear relationship between temperature/deformation-reduced heat dissipation and bulk thermal conductivity held for the variety of surfaces from poorly thermally conductive polymers to highly conductive metals. The surface microthermal conductivity as measured by SThM correlated fairly well with known bulk values. On the basis of these findings, we proposed the realistic practical procedure for the fast evaluation of the surface thermal conductivity of unknown materials.

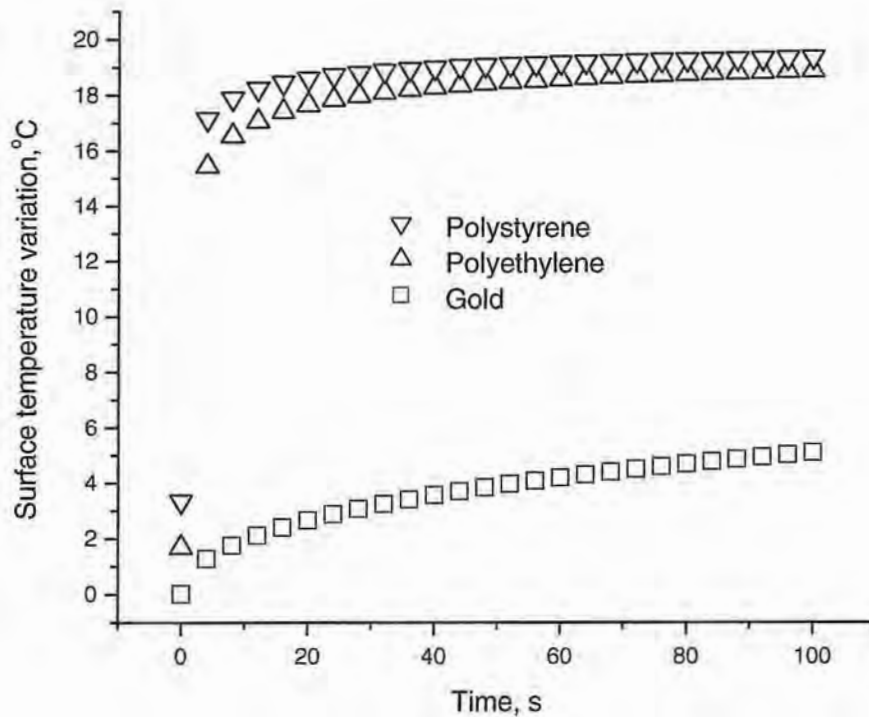


Figure 4.13. Time variation of the surface temperature for PS, PEHD, and gold surface under the thermal probe located at 10 μm above the surface after turning in its temperature to 40°C.

The model of quasi-steady heat transfer between the thermal tip and the surface was used to discuss our experimental results obtained and made certain recommendations for further measurements. This model described correctly the experimentally observed increase of the heat dissipation on the thermal probe approaching the surface with much higher increase observed for highly conductive metal surfaces. As was shown by our simulations, this phenomenon was caused by significant temperature gradient presented on metal surfaces right before the probe-surface physical contact due to the high efficiency of the heat absorption by highly conductive surfaces. Correspondingly, the surface of materials with low thermal conductivity demonstrated very small increase of the heat dissipation in the vicinity of these surfaces. This observation was explained by the fast initial rise of the surface temperature for large probe-surface distances.

The model explored here predicts that there is a lower limit for thermal probe velocities for obtaining meaningful thermal data. Higher velocities of the thermal probe ($>1 \mu\text{m/sec}$) can be recommended for higher sensitivity of microthermal probing especially for the surfaces with low thermal conductivity. Our model predicts that “non-contact” probing at high modulation frequencies (position and/or temperature modulations in kilo Hertz range) can be efficient for the detection of microthermal surface properties. This way, the thermal probing sensitivity can be increased significantly as compared to the conventional probing. Finally, the temperature gradient caused by different heat dissipation abilities of different materials (like in composite materials) persists long enough to create significant thermal contrast that can be detected by SThM measurements.

4.3. Ultra-microstructure and Microthermomechanics of Infrared Detectors in the beetle *Melanophila acuminata*

Microstructural organization of the biological infrared (IR) receptors was studied to elucidate their materials properties useful for prospective biomimetic design. The IR receptors in *Melanophila acuminata* beetles were studied with ultra-high-resolution scanning probe microscopy (SPM) in a range of temperatures. By application of micromechanical mapping and thermal stage, we made attempts to reveal the micromechanical and thermomechanical properties of the cuticular apparatus of the IR sensillum. The main

component of the cuticular apparatus is an internal endocuticular sphere with a diameter of about 15 – 20 μm (Hazel et al., 2001). Highly ordered multilayered organization of the lamellated peripheral mantle of the sphere was confirmed and characterized. It was observed that the interlayer spacing of this microstructure varied along the circumference and decreased to 300 nm in the vertex of the sphere. We demonstrated that the microlayered structure is composed of nanolayers with very different micromechanical properties and thermal behavior. Thermal expansion of the outer mantle was observed and local thermal expansion coefficient under given preparation conditions was measured to be at least $1.5 \times 10^{-4} \text{ grad}^{-1}$.

4.3.1. Experimental

The samples of pit organs of beetles *Melanophila acuminata* were made in Universität Bonn. Figure 4.14 is the schematic drawing of the IR sensillum in beetles *Melanophila acuminata*. The pit organs were in iced 0.05 M cacodylate buffer with 3% glutaraldehyde (pH 7.2) and fixed for 24h at 4°C. After postfixation with 1.5% OsO_4 in the same buffer for 2 h and washing in buffer solution, the specimens were dehydrated in ascending series of ethanol and embedded in Epon 812 (Luft 1961). EPON 812 is a glycidether (i. e. the epoxypropylether of glycerine). The resin was hardened with two different hardners: (i) DBA (2-dodecenyl-amberacid-anhydride and (ii) MNA (methylenedimethylphthalacid-anhydride). Two different mixtures named A (primarily soft) and B (primarily hard) were used. A: Epon 812 (62 g) and hardner DBA (100 g); B: Epon 812 (100 g) and hardener MNA (89 g). A and B were mixed 7:3. During mixing, 1.5% accelerator DMP-30 was added (2,4,6-tri(dimethylaminomethyl)phenol). Semithin sections were made with a Reichert Ultracut Microtome using glass knives. SPM studies were performed on a Dimension 3000 (Digital Instruments, Inc.) microscope and an Explorer (Thermomicroscopes, Inc.) microscope with a scanning thermal microscopy (SThM) mode according to the procedure described in previous publications (Gorbnov et al., 2000). To reveal surface topography, contact mode and tapping mode were employed. Surface composition was tested with lateral force mode and phase imaging.

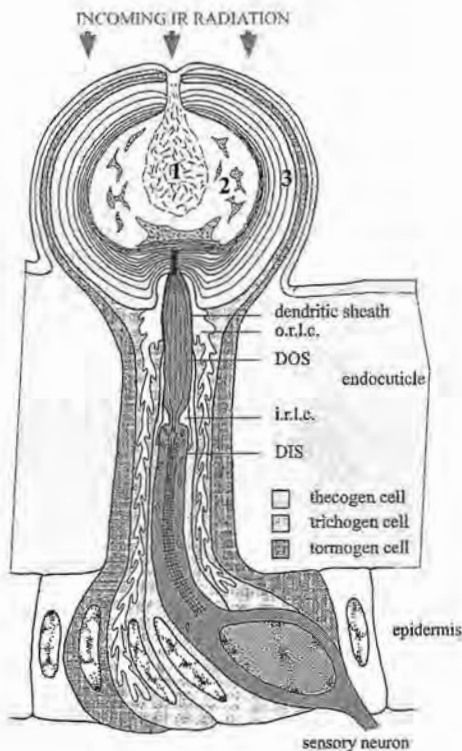


Figure 4.14. Schematic drawing of the IR sensillum. The internal cuticular sphere is composed of three distinguishable areas (1 – 3) and covered by a thin outer cuticle. Three enveloping cells (theco-, tricho-, and tormogen cell) surround the sensory neuron which is anchored with the tip of the dendrite within the peripheral area 3. DIS: dendric inner segment; DOS: dendric outer segment; i.r.l.c.: inner receptor lymph cavity; o.r.l.c.: outer receptor lymph cavity. Diameter of the spere is about 12 μm . Adapted from Vondrdan, 1995.

Microscopic elastic response and surface distribution of adhesion were obtained from force-distance data (Chizhik, 1998, Tsukruk, 1998). Surface distribution of elastic modulus was obtained in the Hertzian approximation according to our earlier developments (Chizhik, 1998). The force-distance data were collected within selected surface areas in force-volume mode and processed to obtain histograms of the elastic modulus and adhesive force distribution (Tsukruk, 2000). For microthermal studies, samples were placed on a thermal stage and scanned at elevated temperatures. Heating was done step-by-step with equilibration time at each temperature of about 15 minutes. Surface distribution of thermal conductivity was recorded with SThM (Gorbunov et al., 2000).

4.3.2. Results and discussion

A high-resolution optical micrograph of the IR organ (Figures 4.15 and 4.16 made in AFRL) shows a distribution of spherical receptors on the bottom of the pit surface. All sensillae are very round and highly reflected spheres of about 15-20 μm micrometers in a diameter. Up to 100-150 receptors are located within a single pit area in relatively ordered manner and with dense packing. Scanning electron microscopy (SEM) micrographs of the pit areas after gentle drying process in vacuum revealed a very different pattern. Initially very round and smooth spherical receptors adopt a collapsed shape with a central opening (Figure 4.17 made in AFRL). Obviously that the walls of spherical receptors collapsed towards the center of the receptors due to removal of water and wax (as indicated in recent TEM studies (Vondran, 1995)) from inside of these receptors as a result of the drying procedure.

To reveal fine microstructure of the receptor walls, the microtomed sections of epoxy-embedded receptors prepared as described above were examined. An optical system in SPM was used to locate a single receptor cross-section and to position the SPM tip on the selected receptor for high-resolution imaging.

General overview imaging (20 – 50 μm across) of receptor cross-sections by SPM demonstrated all major features described before on a basis of electron microscopy data (Figure 4.18). It showed the layered microstructure of the outer areas that are slightly elevated. Central part of the sphere was much more homogeneous and possesses some depletion in the very center of the receptor.

For high-resolution imaging, we concentrated on the lamellated area of the sphere. The peripheral area shows the lamellated structure typical for endocuticle (Hepburn, 1985, Neville, 1975) (Figure 4.19). Up to 5 – 10 curved layers are densely packed and their spatial arrangements are closely correlated, as is concluded from the presence of distinctive 2-D Fourier components (not shown). Interlayer distance varies along the perimeter as demonstrated in Figure 4.19. The average periodicity is 300 ± 100 nm in the vicinity of the apex. This periodicity increases to 1 μm in the bottom part of receptors. Multilayered

structure in the areas close to the receptor tip, consists of wide elevated strips separated by sharp deep grooves, which occupy less than 10 % of the radial dimension.

For multilayered structures with larger periodicity, the ridges are separated by wide valleys (Figure 4.19).

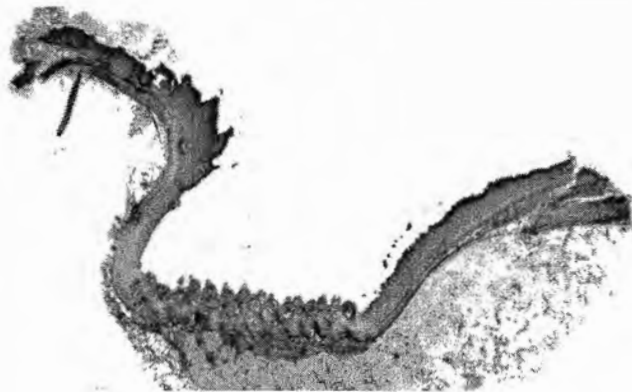


Figure 4.15. Optical micrograph of cross section of IR receptor area of beetles *Melanophila acuminata*.

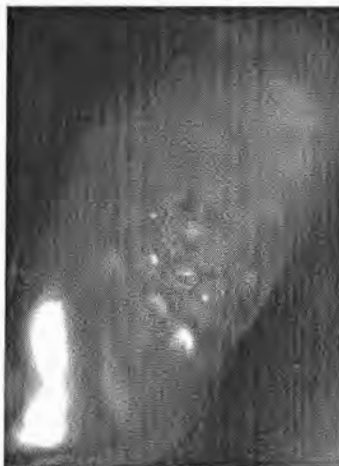


Figure 4.16. Optical micrograph of IR receptor area of beetles *Melanophila acuminata* from front side.

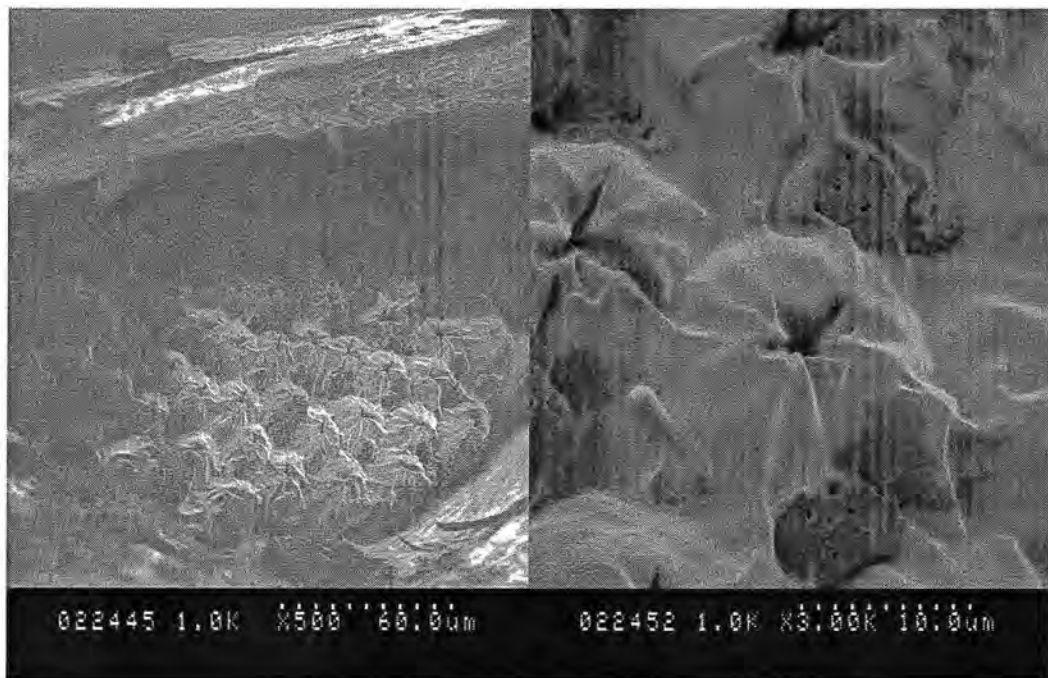


Figure 4.17. SEM micrographs of the receptor array after drying procedure at different magnifications taken by Dr. Stone in AFRL.

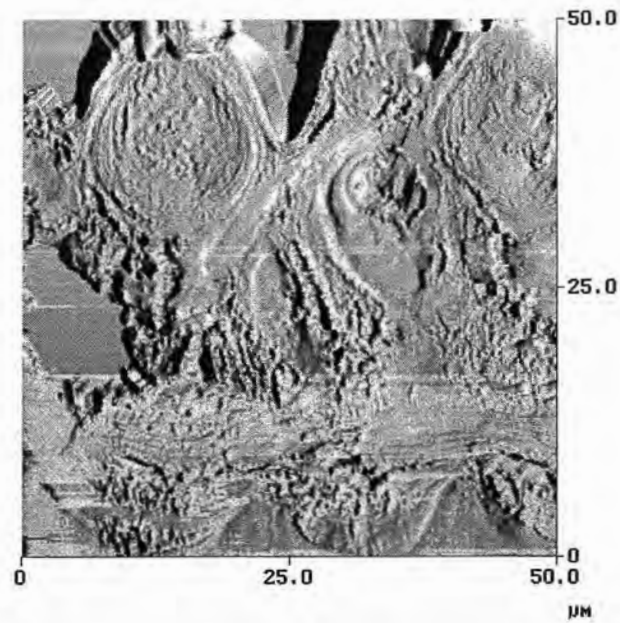


Figure 4.18. SPM topographical image of microtomed ultrathin slices of the receptor areas at low magnifications.

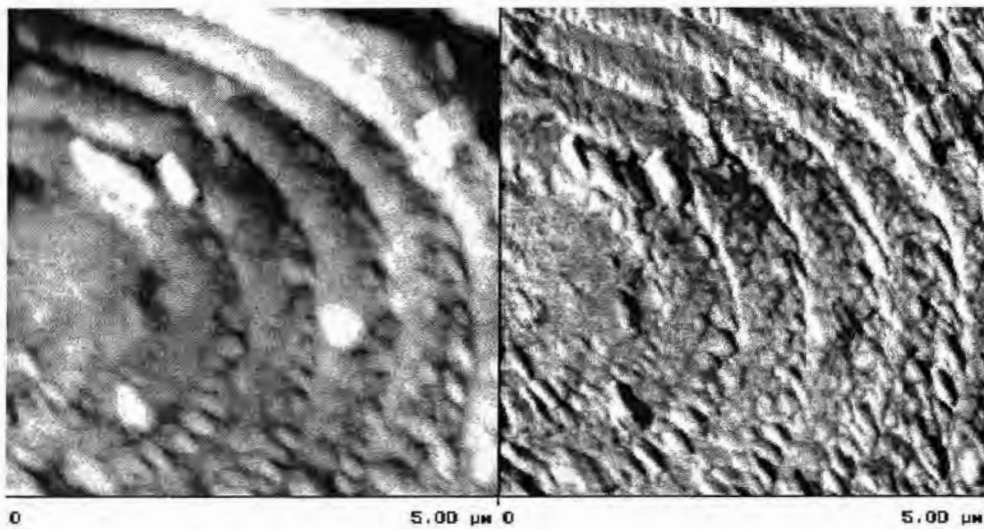


Figure 4.19. SPM topography (left) and lateral force (right) images of multilayered structures in outer areas of IR receptors at intermediate magnifications.

A new feature of surface morphology revealed by high resolution SPM scanning was the presence of ultra-fine grain texture (Figures 4.19 and 4.20). The lateral grain dimensions were in the range of 50 – 150 nm. The grains had irregular shape and were separated by sharp microcracks, as can be seen from higher resolution “deflection” mode that emphasizes fine details by removing a “height” contribution in the topographical image (Figure 4.20). Lateral force microscopy clearly showed grainy texture with groove and grain edges emphasized by spikes in the lateral forces (Figure 4.19). These variations are, to some extent, caused by a “geometrical” contribution generated by the steep edges of microcracks and ridges (Ratner et al., 1998).

As known, the surface variation of the lateral forces in the contact mode and the phase shift in the tapping mode are determined by the surface distribution of the shear strength and viscoelasticity/adhesion, respectively (Ratner et al., 1998, Tsukruk et al., 2000). These properties correlate closely with chemical composition and local stiffness of the surface. Therefore, these modes are considered to be instructive for testing surface composition. Both lateral force (Figure 4.19) and phase (Figures 4.21 - 4.23) images demonstrate that the surface of receptor cross-section is relatively homogeneous without significant variation of local chemical composition and stiffness. On top of the ridges, lateral force fluctuations are reduced. Significant increase of the lateral forces is observed along the groove edges and along the edges of grainy texture (Figure 4.19). The asymmetric shape of the lateral force response indicates significant contribution from “geometrical” friction caused by tilt of the SPM tip climbing over steep edges.

Pixel-by-pixel micromapping of the micromechanical properties revealed the variation of the local elastic response and adhesive forces associated with multilayered structure (Tsukruk et al., 2000, Schmitz et al., 1997). Elastic deformation was probed up to the indentation depth of 10 – 20 nm. Under these conditions, the surface was deformed elastically and was fully recoverable. The surface elasticity possessed a very broad distribution with higher modulus values on top of the grains and lower elastic modulus within the grooves (Figure 4.24). Surface distribution histograms possessed a peak value around 1.3 GPa and a mean value close to 3 GPa (Figure 4.24).

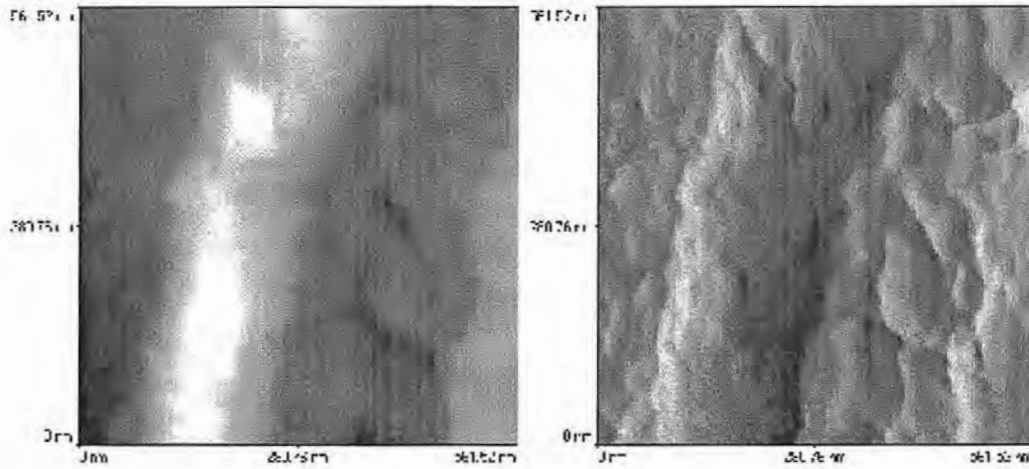


Figure 4.20. SPM topography (left) and amplitude deflection (right) images of multilayered structures with fine grainy morphology at highest magnifications.

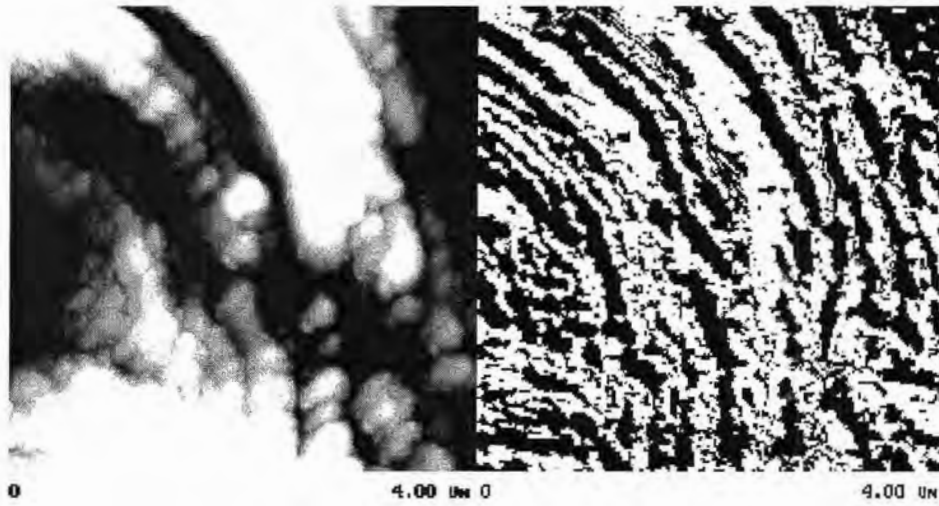


Figure 4.21. SPM topography (left) and phase (right) images of multilayered structures in outer areas of IR receptors at 70°C.

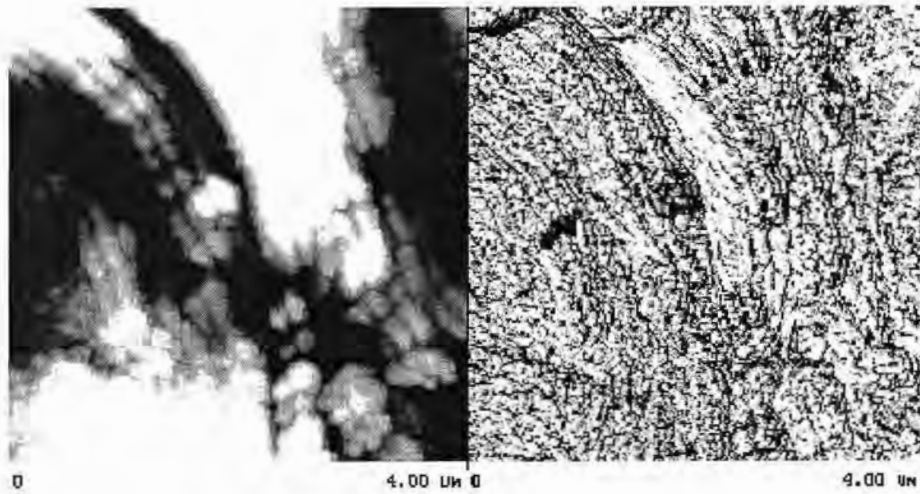


Figure 4.22. SPM topography (left) and phase (right) images of multilayered structures in outer areas of IR receptors at 70°C.

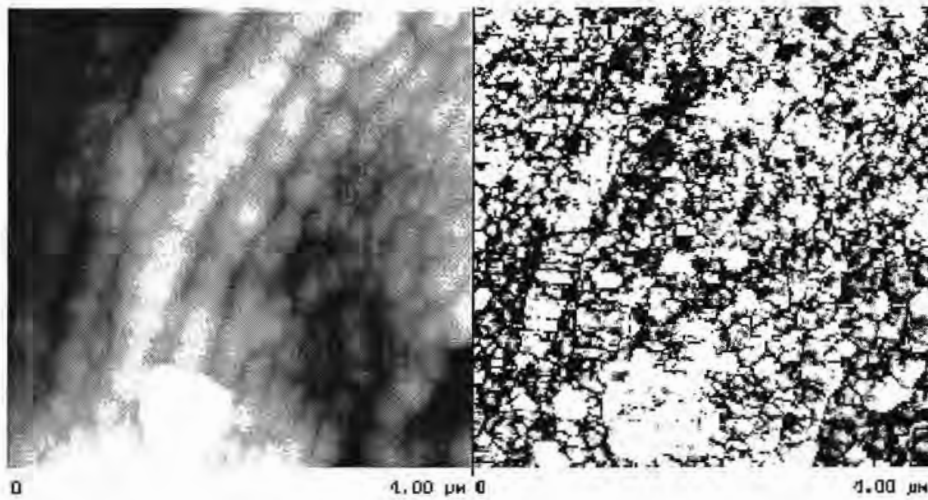


Figure 4.23. SPM topography (left) and phase (right) images of multilayered structures in outer areas of IR receptors at 25°C.

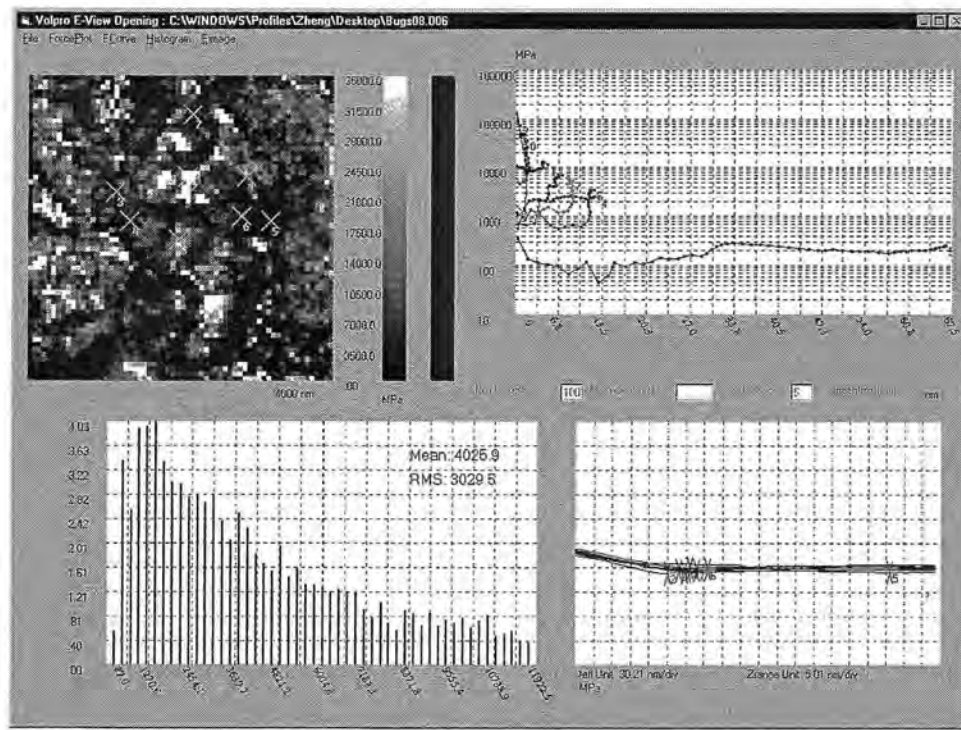


Figure 4.24. Micromapping of elastic modulus (32 x 32 pixels, 4 x 4 μm) (top-left) and corresponding surface histogram distribution of elastic modulus (bottom-left). Top-right and bottom-right images are the examples of Young's modulus depth dependence and the original force-distance curves, corresponding to the number in the elastic modulus mapping respectively.

These values were similar to expected elastic moduli value for the outer areas of insects (Chapman, 1998). Surface distribution of elastic modulus was broad due to variable contributions from surface areas within grooves and the tops of grainy ridges. In some places, indications of very thin topmost surface layer were detected that can be related to some surface contamination associated with the microtoming procedure, however, estimated thickness of these layers did not exceed several nanometers and their presence did not affect measured elastic and adhesive properties. The adhesive force distribution closely followed topography and showed lower values along the main grooves with higher values on top of the grainy-textured surface (Figure 4.25). This surface in a bi-modal surface distribution of adhesive forces with higher adhesion detected within between grains (Figure 4.25).

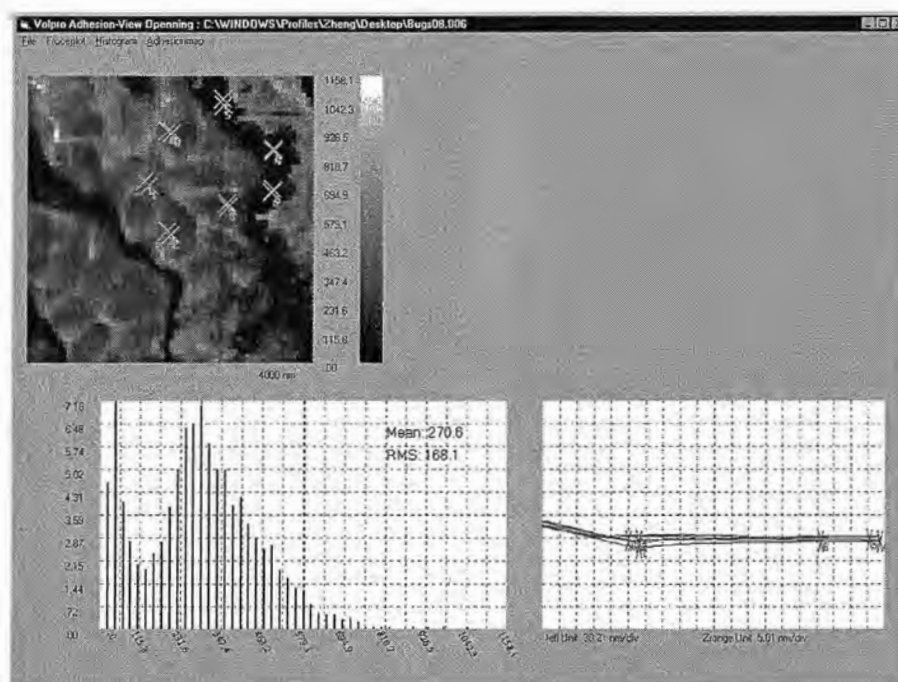


Figure 4.25. Micromapping of adhesive forces (32 x 32 pixels, 4 x 4 μm) (top-left) and corresponding surface histogram distribution of elastic modulus (bottom-left). Bottom-right image is the examples of the original force-distance curves, corresponding to the number in the adhesive forces mapping respectively.

Therefore, surface micromapping confirmed variable elastic and adhesive properties of the multilayered peripheral area. Significant variation of surface micromechanical properties can be associated with the lamellated endocuticular structure typical for insect cuticle as known from TEM experiments (Schmitz et al., 1997). Insect cuticle is composed of microscopic fibrils organized in layers with alternating orientations in perpendicular directions along the surface (Chapman, 1998). In such a case, microtoming exposes fibrils cut either in transversal or longitudinal directions. These cross-sections will have very different micromechanical properties due to their natural anisotropy of fiber cross-sections.

Here, we need to mention that the standard procedure of the embedment of biological material into polymeric matrix (epoxy-resins) to provide support for microtoming may result in a number of artifacts unnoticed by SEM technique but critical for SPM imaging. This is

due to the fact that SPM scanning involves direct physical contact of the nanosharp tip and the surface. Surface contamination due to the transfer of a thin layer of polymeric materials onto the sliced surface during the cutting procedure can be an issue for measuring fine surface details. However, epoxy-resin material has a high glass transition temperature ($>100^{\circ}\text{C}$) after curing at elevated temperature. This significantly reduces the polymer mobility (even at elevated temperature) and should prevent its transfer to the inner surface. Indeed, the quality of ultra-high resolution images (sharpness, edges) confirms that a surface film, if present, could not be thicker than several nanometers. The presence of such ultrathin surface film should not significantly affect our morphology and micromechanical measurements, however, the thermal expansion of original material can be limited by the thermal properties of the epoxy matrix.

As the next step, the thermal behavior of the peripheral area was studied. Before these measurements, we tested if epoxy-resin surface film could significantly affect our results. For this, the surface of epoxy-resin outside of the receptor areas was probed. As was observed, surface stiffness of epoxy-resin was high and greatly exceeded 2 – 3 GPa. This confirms that resin is in glassy state after curing. We observed that a small fraction of the resin surface became more compliant at temperatures above 95°C . This can be related to the beginning of the glass transition. Therefore, to avoid significant contribution from possible softening of the surface resin film, our measurements temperature range was limited to below 95°C .

SThM imaging shows concurrently obtained surface distributions of topography and local heat dissipation associated with thermal conductivity (Figure 4.26)(Gorbunov, Fuchigami and Tsukruk, 2000). Due to the shape of the thermal probe with an effective radius of $5\text{ }\mu\text{m}$, the spatial topographical resolution of this mode was limited to several tenths of a micrometer. Therefore, we did not expect to visualize all of the fine details of the IR receptors (like multilayered structures) in this mode and instead focused on micrometer scale features revealed by SThM.

First, very close correlation was observed between surface topography and the thermal signal (Figure 4.26). In the areas of the receptor tip and receptor bottom, significant depletion was observed and multilayered edges (microstructure is not visible in this mode)

were elevated. Heat dissipation detected simultaneously with topography recording was much higher than the background level for depletions in both the tip and bottom areas (Figure 4.26). The lowest heat dissipation was observed along the elevated peripheral area. Obviously, the surface distribution of heat dissipation is affected by the variation of the tip-surface contact area caused by topography. Due to obvious geometrical reasons, in depleted parts of receptors, the contact area increases and along the ridges, the contact area decreases. This should result in corresponding increasing and decreasing the integrated heat dissipation even if actual local thermal conductivity is unchanged.

The real interesting point of this measurement was how the nano-grainy structure helps heat dissipation systematically in terms of thermal conductivity, mechanical property, and composition. The large radius of thermal probe tip makes such investigation difficult. For future development, one way to deal with this problem is to introduce nano-lithography into the thermal tip fabrication. Majumdar et al. started to develop nano-scale thermal tip in 1995, and the field of research gathered the many attention from the world.

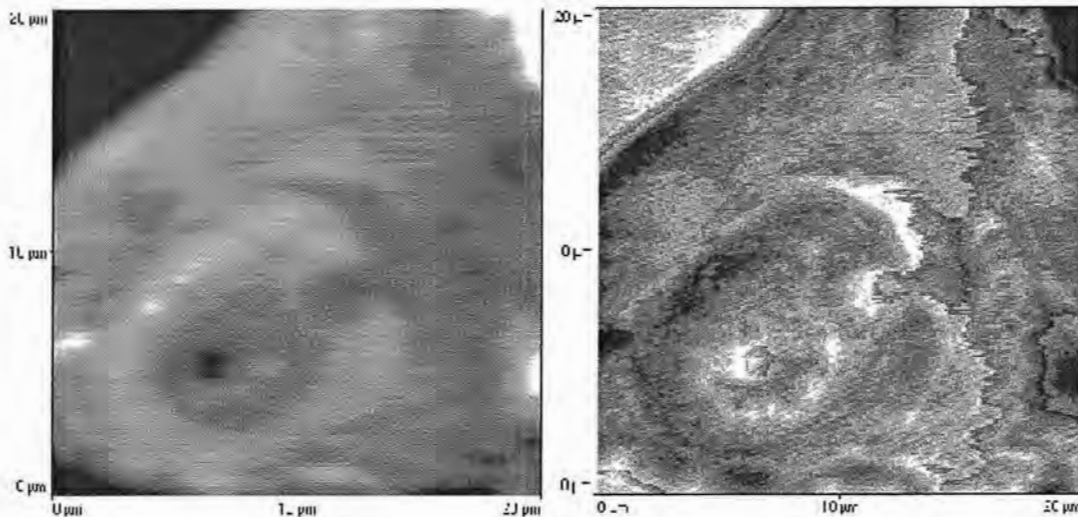


Figure 4.26. SThM topography (left) and heat dissipation (right) images of a section of the IR receptor.

Due to very complicated tip-curved surface interactions, separation of these contributions cannot be done in a simple analytical or numerical way. At this stage of the development of this experimental technique, we cannot quantify this observation nor evaluate what fraction of heat dissipation variation is related to microstructure/materials properties. Further investigations with higher resolution and the development of quantitative models of heat dissipation through the tip-surface interface are required to deconvolute topographical and thermal contributions.

Finally, we tested multilayered microstructure of the IR receptors at elevated temperatures (Figures 4.21 – 4.23). Samples were heated by 5-10°C, equilibrated, and SPM images were taken from the same surface area at identical scanning conditions. As clear from these images, the multilayered structure undergoes significant changes during heating. Although surface topography remained virtually unchanged, phase images were changed completely at elevated temperature. Heating to intermediate temperatures (40 – 60 °C) lead to a significant increase of dark areas on the phase images (Figure 4.21 – 4.23). Further heating resulted in dramatic changes of the phase image: clear layering occurred with formation of a very distinctive multilayered pattern that exhibited large differences in the phase shift between adjacent layers (Figures 4.21 – 4.23). This change demonstrated that softening of the multilayered structure occurred non-uniformly, with interlayers becoming compliant at elevated temperature. This observation is a confirmation of the fact that layers in the peripheral area of the sphere are composed from materials with different mechanical and thermal properties.

By scanning silicon grids in the same range of temperatures, we observed that, despite thermal drifts, lateral dimensions of surface features on SPM images obtained at elevated temperatures, can be reproduced within $\pm 0.5\%$. Thus, topography data can be used for evaluation of the rate of thermal expansion. To improve the accuracy of dimensional measurements, an image analysis was applied to the images to enhance grain boundaries. The variation of the interlayer periodicity averaged over three independent measurements for two independent heating cycles is presented in Figure 4.27. From this data it is clear that very minor thermal expansion of the multilayered structure occurred during heating from 25 to 95 °C. Linear regression analysis of the data gave a thermal expansion coefficient of

$k \leq 1.5 \times 10^{-4} \text{ grad}^{-1}$. The uncertainty of our measurements of interlayer spacing prevented more precise estimation. Therefore, the thermal expansion coefficient of multilayered structure as measured under given conditions does not exceed $1.5 \times 10^{-4} \text{ grad}^{-1}$. It worth to note that current estimation represents the lowest limit for thermal expansion due to the fact that data were collected for material embedded in epoxy matrix.

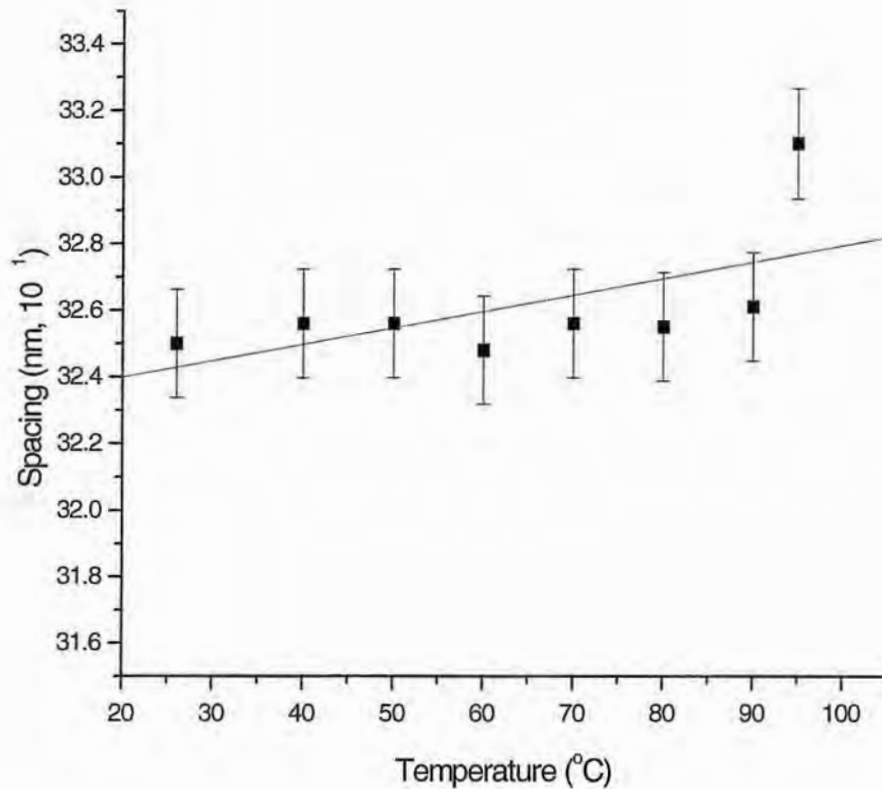


Figure 4.27. Temperature variation of multilayered spacing for sections of the IR receptors during heating cycle.

4.3.3. Conclusions and perspectives

SPM studies of IR sensilla revealed several ultra-fine features of their cuticular apparatus. First, we confirmed previous electron microscopic data on the structure of the peripheral lamellated area of the internal sphere composed of alternating elevated layers and grooves with layered periodicity in the range 0.3 – 1.0 μm and correlated packing of 5 – 10 layers. Second, ultra-high resolution imaging revealed nanograined surface texture with irregular grains of 50 – 150 nm, densely packed along the perimeter and separated by grooves and microcracks. Third, scanning thermal microscopy showed much higher apparent thermal conductivity at two specific locations within the cuticle where the neuron is located and lower thermal conductivity along the periphery of the sphere (i. e. area 3, c. f. Figure 4.14). Fourth, the multilayered structure was composed of alternating layers of ridges with high elastic modulus and low adhesion and grooves with lower elastic modulus and high adhesion. At elevated temperatures, interlayer areas became softer, creating an alternating compliant-stiff layered structure. Thermal expansion leads to a modest variation of interlayer periodicity with an estimated thermal expansion coefficient of $\leq 1.5 \times 10^{-4} \text{ grad}^{-1}$. This value is close to the range of thermal expansion coefficients required for cuticle to possess thermal expansion to work as photomechanical sensor (Vondran, 1995). To clarify some details of thermomechanical behavior of functioning biological IR receptors, more sophisticated experimental set-ups should be implemented to include in-situ studies of the IR receptors on live beetles with minimum distortions introduced by the preparation procedure.

From the point of view how these receptors can monitor thermal flux, their design to some extent recall the design of Golay cells that is based on the detection of a sub-micrometer scale deviation of thin membranes caused by expanded gas in a sealed cell (Chapman, 1998, Golay, 1947, and Chevrier, J-B et al., 1995). This design showed much improved sensitivity with a millisecond response time. It seems to us that several steps were undertaken by nature to increase thermal sensitivity of these receptors as compared to the Golay design. First, the outer receptor membrane is obviously composed of flexible materials with much higher compliance than solid membranes in current Golay cells. The design of the endocuticle from very compliant thin walls should provide much higher flexibility of the structure as compared to a rigid single membrane in current Golay design.

Second improvement is the multilayered structure of these walls that provides much faster response as we discussed above but also allows much higher probability for particular temperature fluctuation resulting in expansion of particular walls elements. Finally, spherical design with multilayered structures surrounding the vertex of the receptor instead of planar membrane arrangement results in significant amplification (by factor of 2π) of the geometrical displacements thus increasing thermal sensitivity of the design. Obviously, testing of these suggestions goes beyond the scope of this publication. It requires extensive studies on living specimens to characterize microthermomechanical parameters and understand how this design can be transferred to microtechnology-compatible design.

4.4. Ultra-microstructure and Microthermomechanics of Snake IR Receptors

The thermal or infra-red (IR) receptors of snakes with “night vision” were studied with ultra-high-resolution SPM at close to in-vivo conditions to elucidate their materials properties critical for prospective biomimetic design of “soft matter”-based IR sensors. The surfaces of living tissues were scanned and resulting parameters were compared with data obtained for chemically treated (formaldehyde-fixed) tissues under wet ambient conditions. We concluded, that microstructural parameters for formaldehyde-fixed snake skin are similar to ones observed for living skin but differ significantly for microtomed slices under ultra-high vacuum conditions. Significant difference in surface thermal conductivities was observed for receptor areas as compared to non-specific skin areas in the vicinity of receptors. Micromechanical analysis showed that pit areas are much more compliant and possessed gradient mechanical properties with maximum elastic modulus for topmost layer and gradually reduced elastic resistance for deeper layers. As heat transfer simulations showed, observed difference in surface thermal conductivities should result in significant local temperature gradient around receptors areas. Possible reason for such materials properties difference can be highly porous microstructure of underlying tissue as revealed by preliminary SPM studies of receptor tissue microstructure.

Several major questions are addressed in the course of this study:

- How surface morphology of snake IR receptors held under close to living, wet conditions are relevant to previous studies of surface morphology of snake skin conducted for chemically treated tissue and under high-vacuum?
- Are any features of surface thermal conductivity of snake IR receptors distinguish them from non-specific skin areas?
- Are any micromechanical responses of snake IR receptors that can be a signature of these areas as compared with non-specific skin areas?
- Are any details of microstructural organization or IR receptor tissue that can cause their functioning as high-sensitive photothermal receptors?

4.4.1. Experimental

SPM studies of surface topography were performed in the contact mode on a Dimension 3000 (Digital Instruments (DI), Inc.) microscope according to the procedure described in detail earlier. Silicon cantilevers had spring constants about 50 N/m and tip radius within 20 – 40 nm. Imaging was done at scan rates in the range 1 – 2 Hz. Micromapping of elastic response and surface distribution of adhesion were obtained with force-volume mode. The collection of force-distance probing curves within 1 x 1 μm areas with resolution 32 x 32 pixels were processed to obtain histograms of distribution of elastic modulus and adhesive forces as described in detail elsewhere (Tsukruk, 1998). Surface distribution of elastic modulus was obtained in Hertzian approximation as described earlier. (Tsukruk, 1998).

Microthermal imaging and microthermal probing were done in the same method described in 4.1. We calculated thermal conductivity of snake pit area and non-pit area using the procedure described in 4.4. Two types of measurement were carried out for this purpose. First, preheated thermal probe was approached to the surface and the heat dissipation was monitored before, during, and after actual physical contact. Preheated temperatures were chosen as 40, 52, 63, and 73 °C. Second, the temperature of the thermal probe was risen after direct physical contact with skin surface and heat dissipation was monitored during heating cycle (μTMA).

Samples for investigation were placed on a concave glass support covered by wet towel with edges submerged into water bath to provide local 100 % humid environment during measurements (Figure 4.28). Water absorbed by wet towels formed a thin water layer on an open surface area that was available for SPM scanning. This technique has been used for both living tissue and formaldehyde-fixed tissue to prevent fast drying and shrinkage. Under these conditions, scanning was performed on living tissue specimens within several hours after mounting to assure non-degraded state of the surface.

Here, it should be noted that the presence of sometimes relatively thick (100 – 500 nm) surface layer of water and blood does not affect our measurements. The SPM tip has a height of 3.5 μm and if the very end scan surface covered by layer of fluid, it does not affect experimental conditions in normal contact scanning and micromechanical probing. For living tissue because of presence of relatively thick layer of fluid, our data can be considered as relevant to skin-fluid interface, however, surface fluid layer can affect SThM measurements and, in our case, it prevented us from taking meaningful microthermal data for living tissue.

4.4.2. Results and Discussion

4.4.2.1. Surface morphology

Here, we focus on surface morphology observed for skin of living tissues of Indian Python (i. e. Burmese Python, or Python molurus bivittatus) cut from both receptor and non-specific skin areas. The comparison of collected from this experiment was made to concurrent data obtained from formaldehyde-fixed skin area of Ball Python in the course of this study (Hazel et al., 1999) as well as with previous SPM studies of Carpet Python skin under ambient conditions (Campbell et al, 1999).

Surface of Indian Python skin within non-specific areas as observed for living tissue under wet conditions displays the arrays of uniformly aligned terraces and randomly distributed nanopits with virtually uniform surface density all over the skin (Figures 4.29 and 4.30) Receptor areas show very similar morphology with familiar terrace-like microstructure and nanopit array (Figures 4.31 and 4.32).

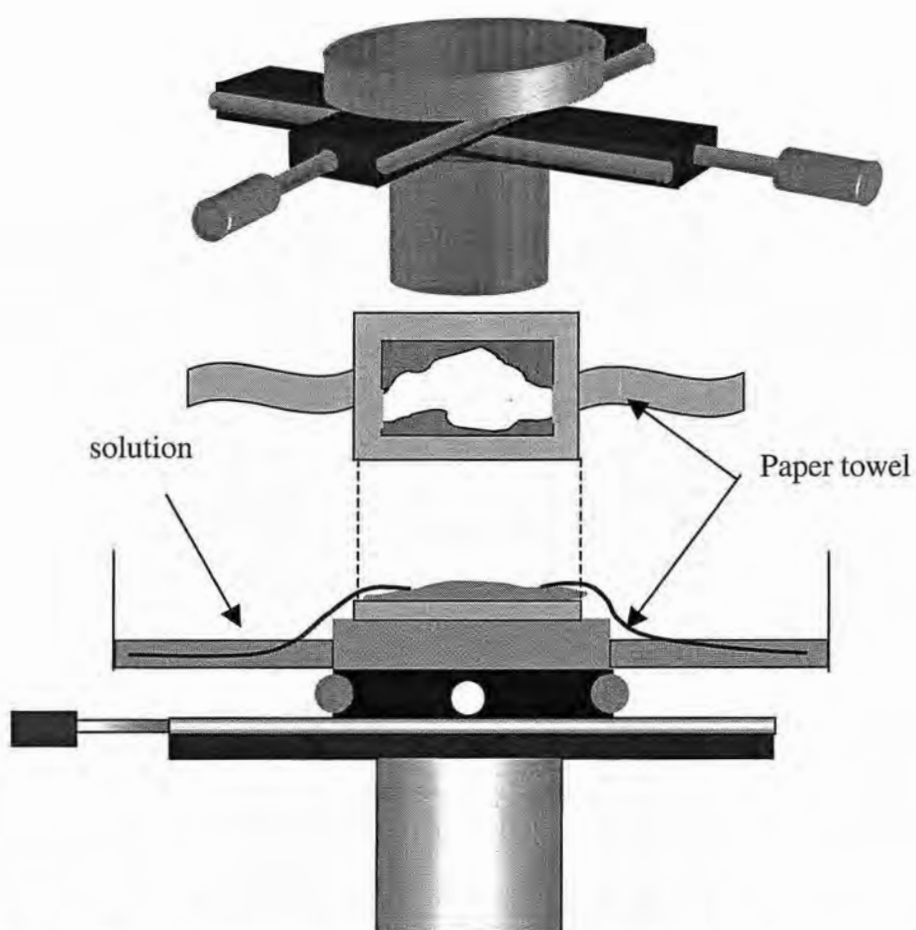


Figure 4.28. Special micro-stage supporting 100 % humid environment to biological samples by wet towel bridge. Samples are placed on the silicon substrate. Concave shape of the surface makes SPM scan less difficult.

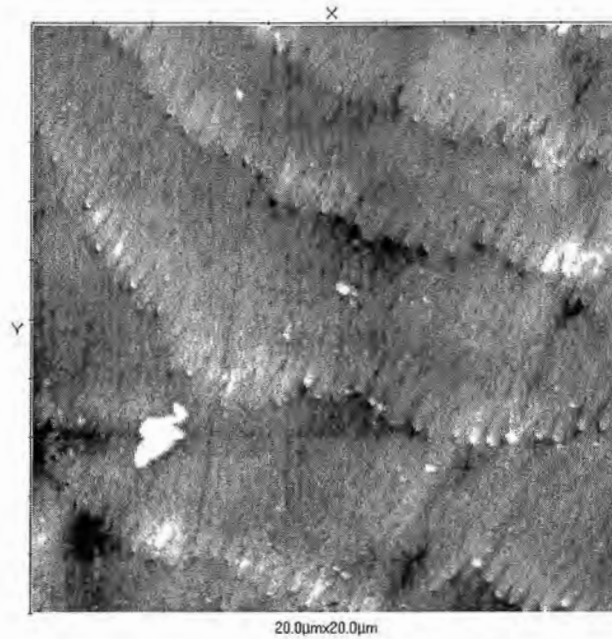


Figure 4.29. 3D surface morphology of snake skin (alive Indian Python)

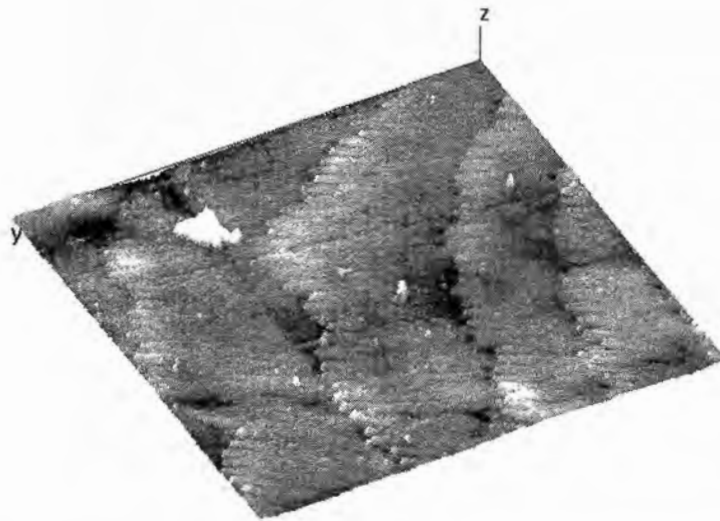


Figure 4.30. 3D surface morphology of snake skin (alive Indian Python) (3-D image analysis of Figure 4.29).

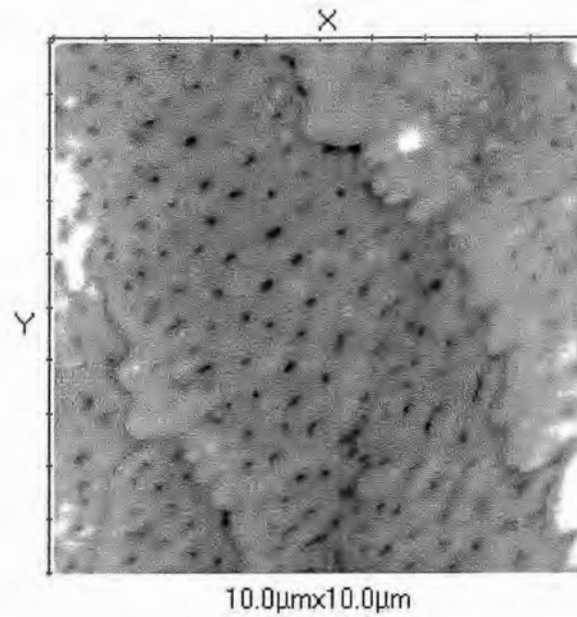


Figure 4.31. 3D surface morphology of snake IR receptor (alive Indian Python)

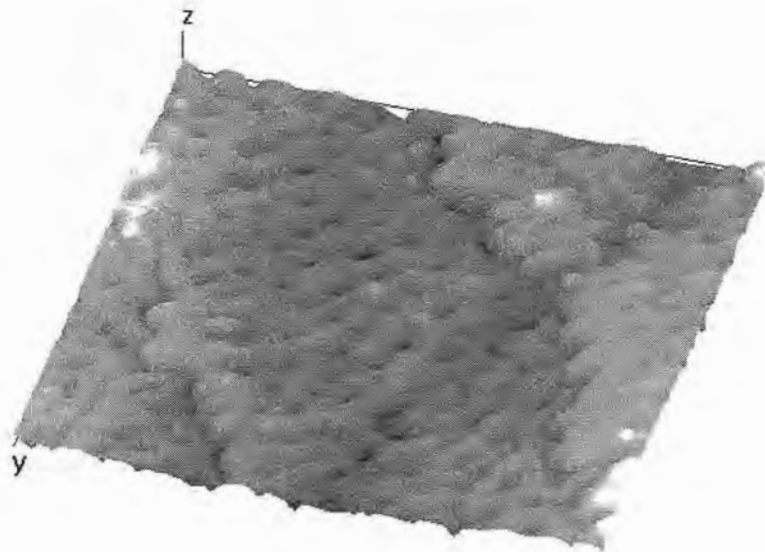


Figure 4.32. 3D surface morphology of snake IR receptor (alive Indian Python) (3-D image analysis of Figure 4.30).

These SPM data on living tissue confirms previous observations of nanopit and terrace-like surface morphology for treated skin that were discussed in detail previously. We should mention that this type of morphology was common for very different types of snakes despite their type and age (five different types were studied in the past) (Hazel et al., 1999, Campbell et al., 1999, Amemiya et al., 1995, Chiasson et al, 1989, and Stille, 1987). In our current studies of two different formaldehyde-fixed Ball Pythons skins of different ages we observed virtually identical surface morphology with indistinguishable geometrical parameters. On basis of these studies, we assume that the observed surface morphology is unique for all snakes with heat detection capability.

Therefore, we conducted comparative studies here as well as compared these results with observations published recently for other snakes (Table II).

For detailed analysis of surface morphology, we selected several “geometrical” parameters used before: the periodicity (the average distance) of terrace-like microstructure, the diameter and the depth of nanopits, and the distance between micropits (Table II). All these parameters were obtained from statistical analysis of several SPM images and their histograms of distribution based on at least 40 – 50 measurements are presented in Figures 4.33 – 4.36. As clear from these data, the average periodicity of nanopit array is more than one order magnitude smaller than the periodicity of terrace-like structure: 300 – 500 nm versus 5 – 6 microns. Variations of both parameters is fairly wide and is within 10 – 20 %. Within this variation, the periodicity of terrace-like structure is indistinguishable for non-specific skin and receptor areas giving the average value of about 5.5 μm . Unlike, the periodicity of nanopit array is much larger for receptor areas (Figure 4.34) This value is 520 nm for receptor areas and 330 nm for non-specific skin areas. This difference is significantly higher than standard deviation of surface distribution (about 20%). Similar differences are observed for diameter and depth of nanopits: nanopits are much wider (390 nm versus 130 nm) and deeper (120 nm versus 20 nm) in receptor areas (Figure 4.35) Standard deviation is comparable in both areas.

Similar trends are observed for formaldehyde-fixed skin areas of Ball Python studied here (Table II).

Table II. The average value of the morphological parameters for three types of snakes. Carpet Python data are taken from Campbell et al., 1999.

<u>The diameter of nanopits (nm)</u>		
	Pit	Non-pit
Indian Python (alive)	387±65	129±20
Ball Python	435±99	119±21
Carpet Python	319±92	249±72
<u>The depth of nanopits (nm)</u>		
	Pit	Non-pit
Indian Python (alive)	124±25	23±5.7
Ball Python	93±23	24±5
Carpet Python	46±23	16±10
<u>The distance between nanopits (nm)</u>		
	Pit	Non-pit
Indian Python (alive)	517±78	331±71
Ball Python	671±134	450±96
Carpet Python*	808±284	677±290
<u>The width of pit layers (μm)</u>		
	Pit	Non-pit
Indian Python (alive)	5.8±0.48	5.3±1.4
Ball Python	5.5±1	2.0±0.47
Carpet Python	3.5±1	1.9±0.5

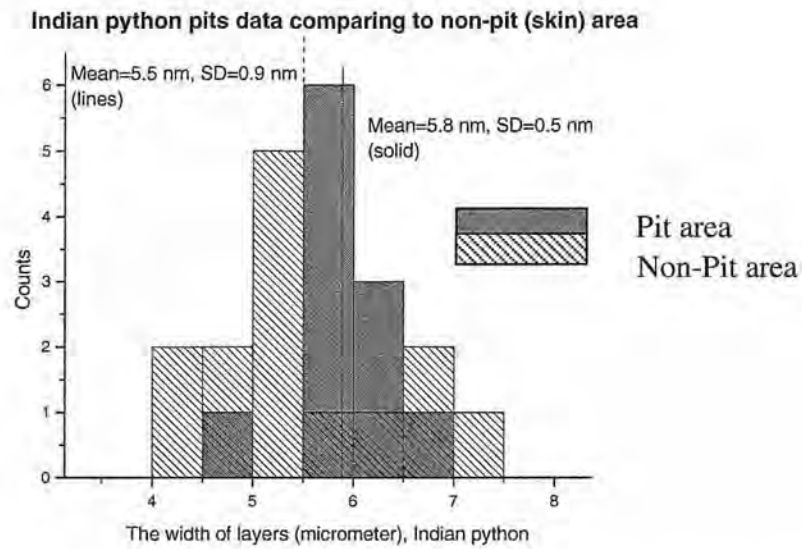


Figure 4.33. The distribution of the width of layers for alive Indian Python comparing the pit area to non-pit area.

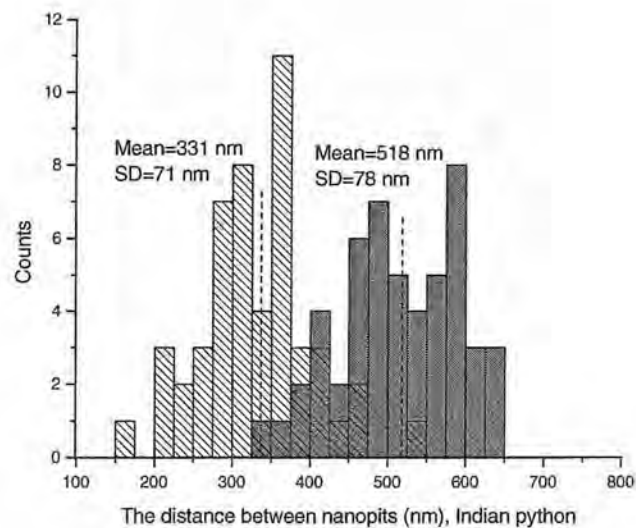


Figure 4.34. The distribution of the distance between nanopits for alive Indian Python comparing the pit area to non-pit area.

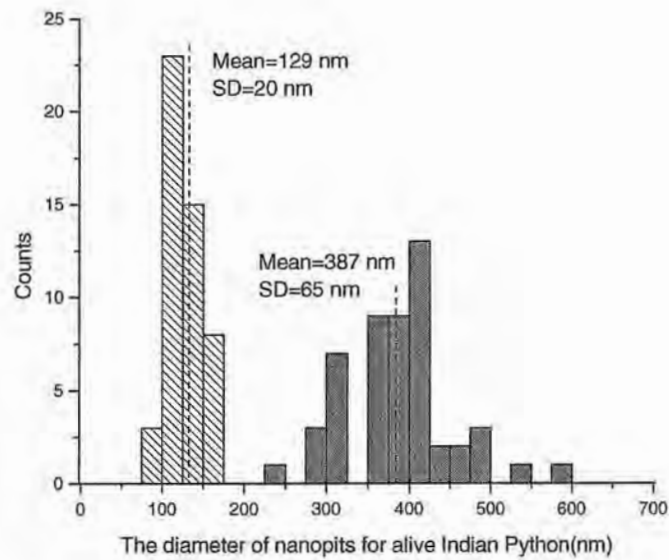


Figure 4.35. The distribution of the diameters of nanopits for alive Indian Python comparing the pit area to non-pit area.

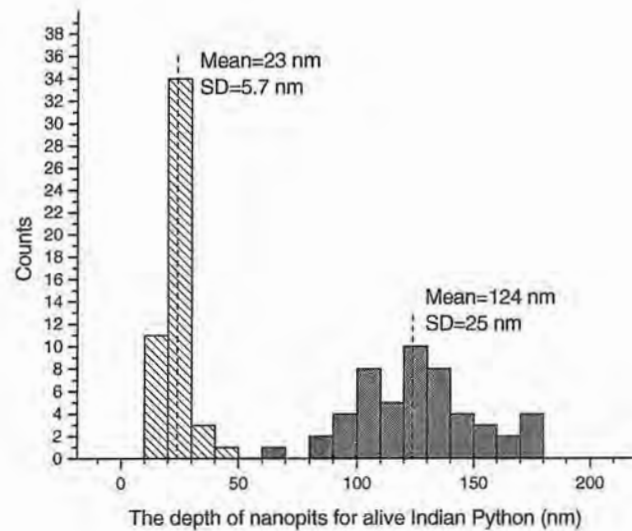


Figure 4.36. The distribution of the depths of nanopits for alive Indian Python comparing the pit area to non-pit area.

Similar conclusions can be made if we compare these data with data available for Carpet Python (statistical analysis was presented) (Table II, Figures 4.37- 4.40) The periodicity of terrace-like structure and nanopit arrays, diameter and depth of nanopits, all are lower for non-specific areas.

4.4.2.2. Microthermal properties

Here it should be mentioned that our attempts to measure surface thermal conductivity of living tissue failed due to the fact that its surface was very wet with a thick water/blood layer and physical contact of the thermal tip resulted in uncontrolled increase of the contact area and, thus, heat dissipation due to the meniscus formation.

Testing of microthermal properties of snake skin involves several independent experiments (Figures 4.41 - 4.44) First, we scanned receptor areas with SThM to observe if any singularities in surface thermal conductivity can be observed (Figure 4.41) For all surface areas, very uneven surface distribution of heat dissipation with local areas of several micron across with difference in heat dissipation of several mWs was observed. Careful comparison of surface topography and heat dissipation distribution shows close correlation: shallow areas display higher heat dissipation while bumps show much lower local heat dissipation. This kind of correlations indicate that the observed uneven surface distribution of heat dissipation is caused by the topographical contributions that cause variable contact area between the thermal tip and thus variable heat transfer in the contact point. At higher magnification (scan size $20 \times 20 \mu\text{m}$), some layering of surface distribution of heat dissipation is observed that can be associated with terrace-like morphology (Figure 4.41) Scanning with higher magnification is prevented by limited spatial resolution of current design of SThM technique. Indeed, spatial resolution of the thermal probe for compliant materials is estimated to be within $0.5 - 1 \mu\text{m}$ that is too low to expect resolving heat dissipation singularities associated with nanopit array with diameter of a single pit hole below 400 nm. Taking into account the effective contact area, the radius of heat dissipation distribution can be estimated to be in the range from 0.5 to $10 \mu\text{m}$. This estimation sets the limits of lateral resolution of microthermal probing and the depth of its thermal sensing under given experimental conditions.

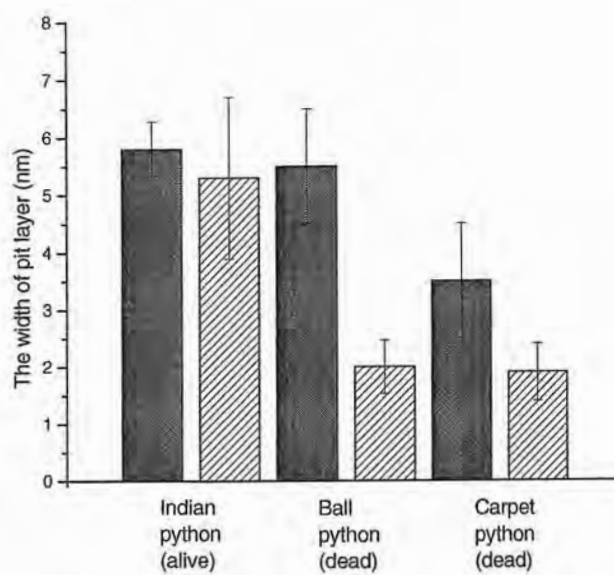


Figure 4.37. The average values of the width of a pit layer for three different kinds of snakes.

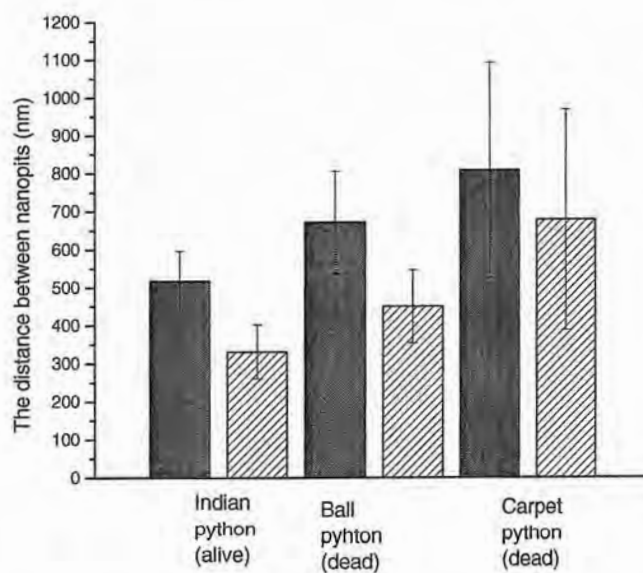


Figure 4.38. The average values of the distances between nanopits for three different kinds of snakes.

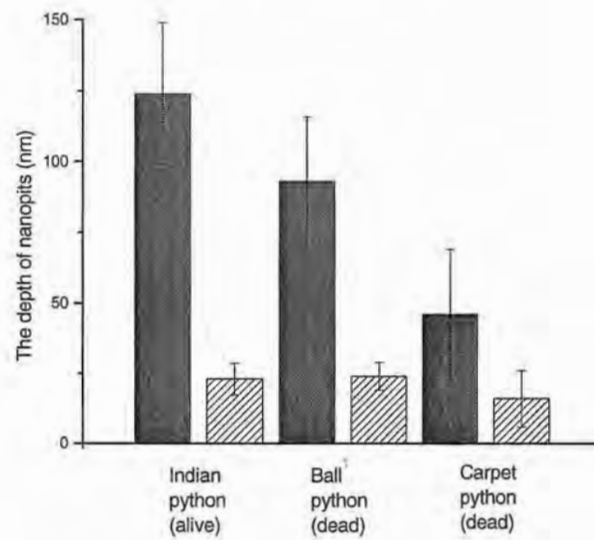


Figure 4.39. The average values of the depths of nanopits for three different kinds of snakes.

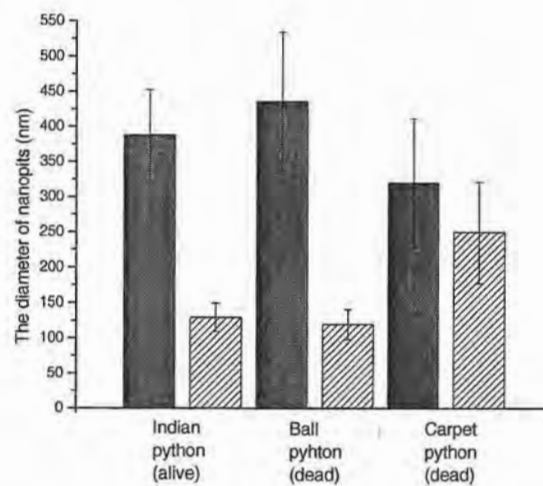


Figure 4.40. The average values of the diameters of nanopits for three different kinds of snakes.

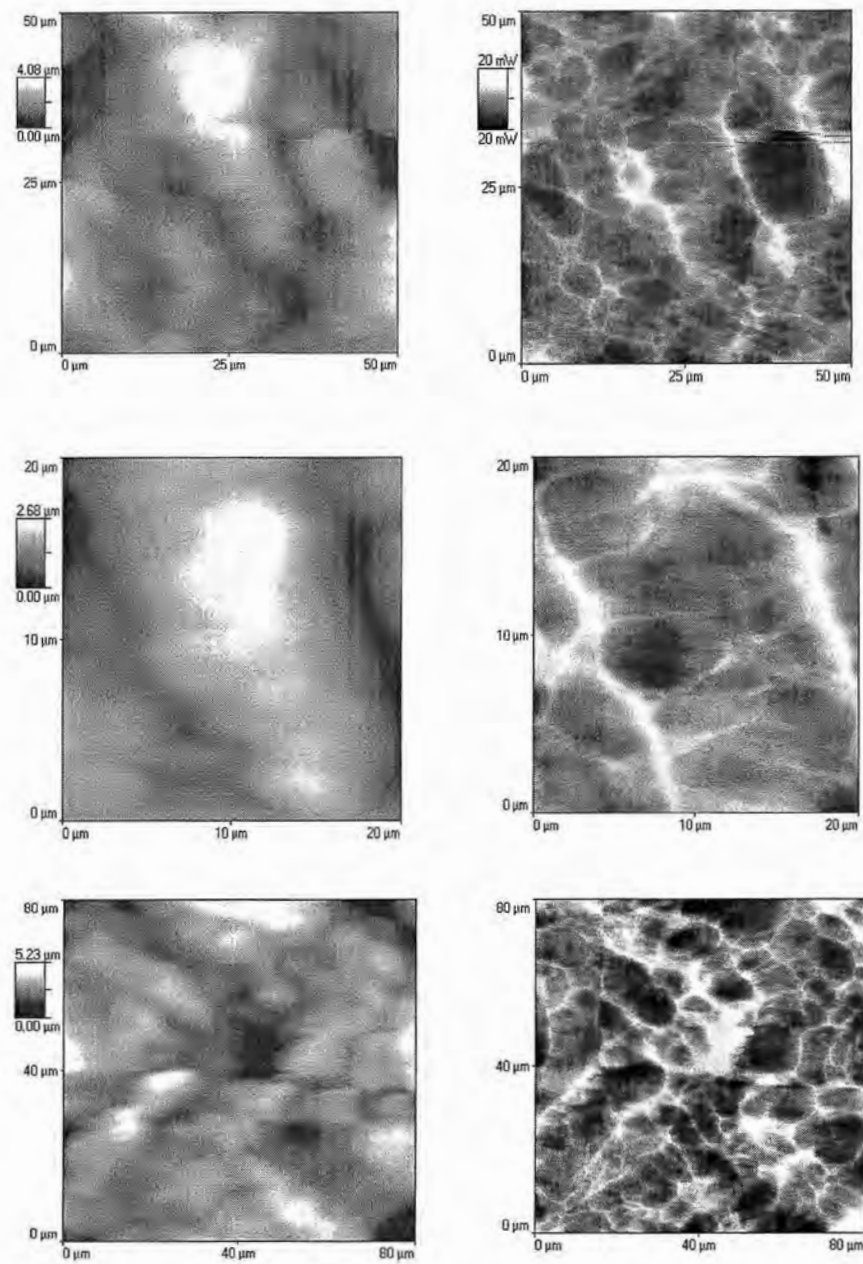


Figure 4.41. SThM images for Ball Python: morphology (left) and thermal conductivity contrast (right).

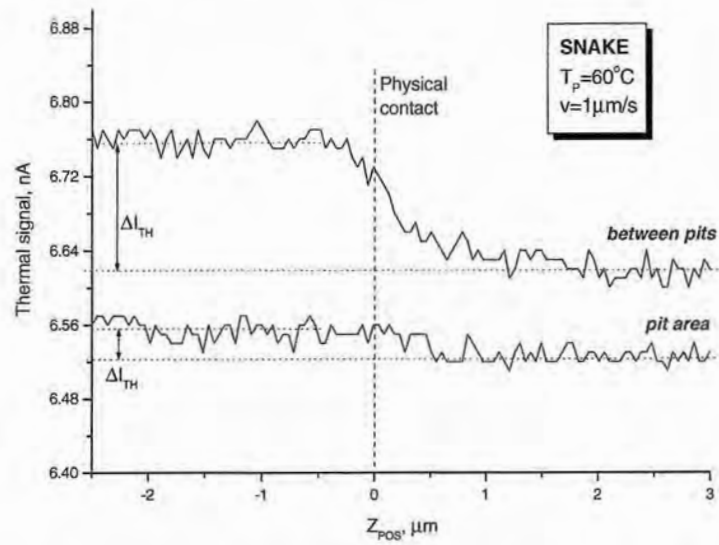


Figure 4.42. Thermal distance curve for snake pit area and non-pit area using Ball Python. Probe temperature was 60 °C, and approaching velocity of the probe was 1 $\mu\text{m}/\text{sec}$.

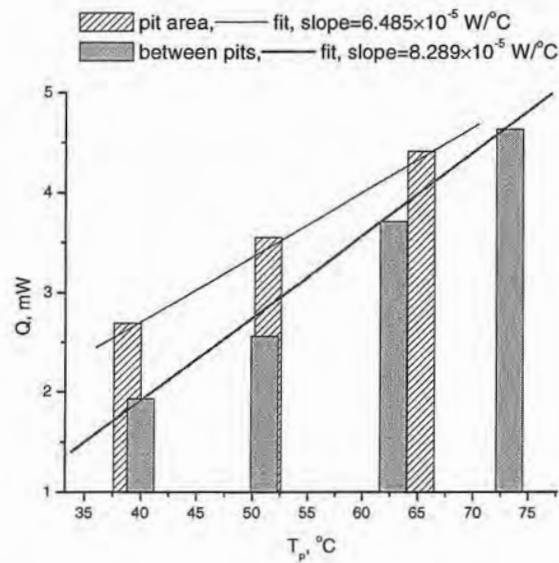


Figure 4.43. The dissipated heat during approaching-retracting motion of a thermal probe to the surface of snake pit and non-pit area using different initial probe temperatures.

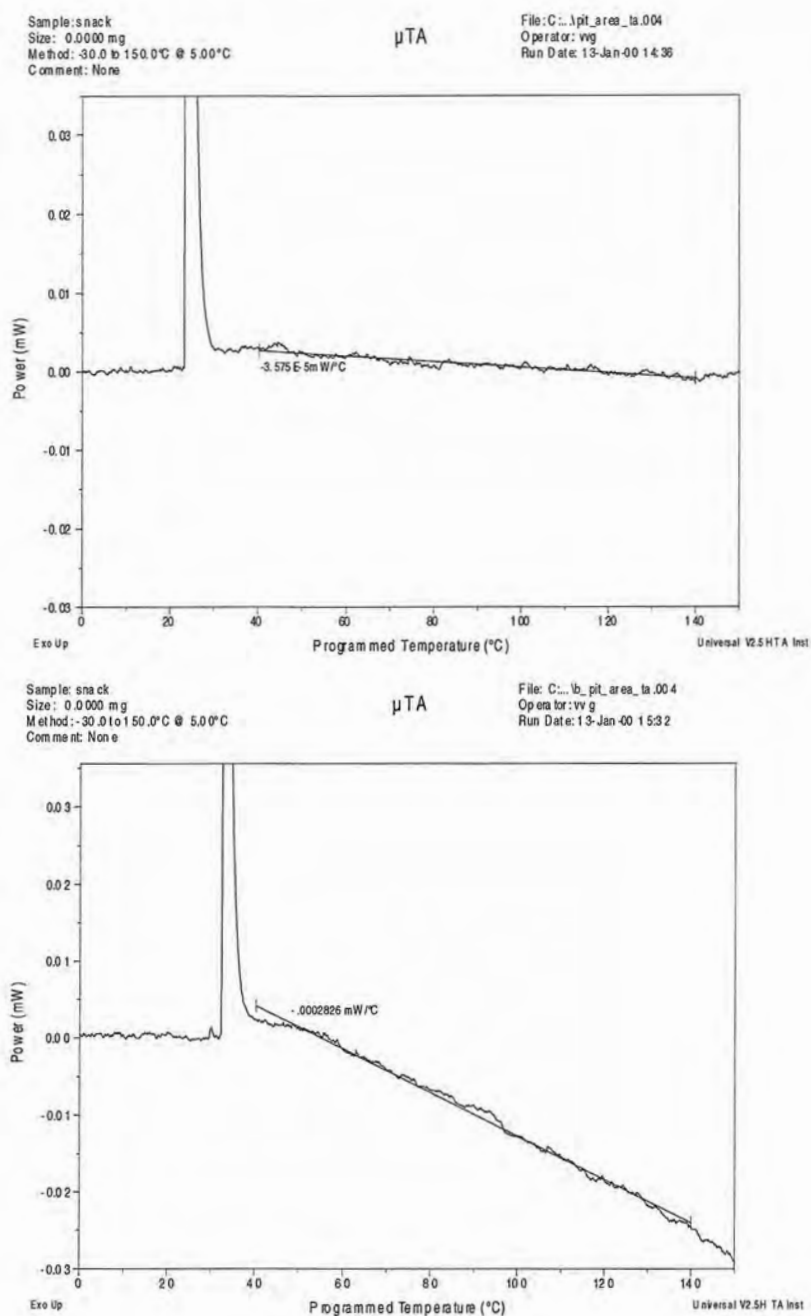


Figure 4.44. Microthermograms for the IR receptor (top) and the non-specific skin areas (bottom) of Ball Python. Heating rate was 5 °C/sec, and the same thermal probe was used for both measurement to keep the same conditions.

Considering that the size of snake pit receptors is several millimeters across and major histological structures are located within micrometers below the receptor surface, it can be concluded that we, indeed, measure integral microthermal response of snake surface as well as buried features within very thin ($<10\ \mu\text{m}$) layer under this surface. On the other hand, the probing area is very small in comparison with actual pit size that eliminates possible influence of adjacent non-specific skin areas.

To estimate the absolute values of surface thermal conductivity, we exploited two different approaches described in chapter 4.4. Here, first, the measurement of heat dissipation, ΔQ , at the physical contact of the thermal probe preheated to temperature T_p and snake surface with initial temperature T_s (microthermal probing) was done. Second, the instant monitoring of heat dissipation $Q(T)$ in the contact point after tip engagement during temperature increase (microthermal analysis) was done.

As we observed, heat dissipation variation during physical contact, ΔQ , increases significantly after physical contact of the thermal tip and snake surface (Figure 4.42). This increase is much higher for receptor surface areas. Repetition of such probing for different initial temperatures of the thermal tip displays virtually linear correlation with ΔT as expected from the equation (9) (Figure 4.43).

The cumulative results of multiple probing of microthermal properties of receptor and non-specific areas (about 30 independent measurements) are presented in Figure 4.45. Surface distribution of the temperature gradient of heat dissipation, $\Delta Q/\Delta T$, shows a broad distribution with two distinctive maxima separated far beyond random variations. The value for pit, receptor area is observed to be much lower than for the surface areas outside of snake receptors. This absolute value of surface thermal conductivity was calculated in the way described in chapter 4.2. We obtained values of $\lambda = 0.11\ \text{W/m-K}$ for receptors and $\lambda = 0.34\ \text{W/m-K}$ for non-specific skin areas outside of receptors but close to them. The latest value is close to the typical value for organic carbon-based macromolecular materials such as low density polyethylene, $\lambda = 0.29 - 0.35\ \text{W/m-K}$ (Granta Design). On the other hand, the surface thermal conductivity of the pit receptor areas is much smaller than the thermal conductivity of non-specific skin areas. It is also much lower than typical values for vast majority of organic polymer ($0.2 - 0.4\ \text{W/m-K}$) (Table III).

Table III. Young's modulus & Thermal conductivity of three types of snakes calculated from experimental data.

Young's modulus (MPa)		
	Pit	Non-pit
Indian Python (alive)	39±16	144±117
Ball Python	43±21	154±33
Carpet Python	N/A	N/A

Thermal conductivity (W/m-K)		
	Pit	Non-pit
Indian Python (alive)	N/A	N/A
Ball Python	0.11	0.34
Carpet Python	N/A	N/A

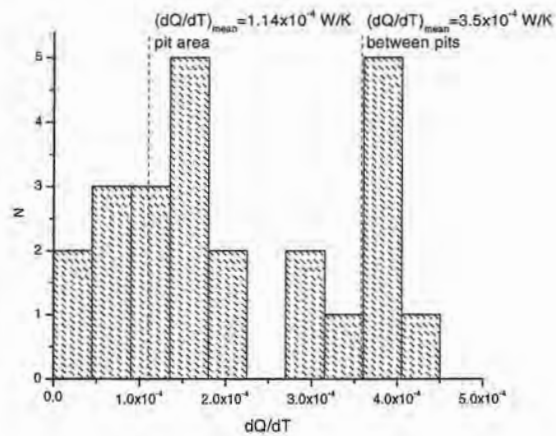


Figure 4.45. Histogram of surface distribution of thermal conductivities across receptors areas and outside receptors.

Therefore, the major conclusion from our microthermal measurements, is that snake receptors possess usually low surface thermal conductivity. To understand implementation of these results and what meaning they could have for the thermal sensing of receptor areas, we conducted simulation of surface temperature variation for receptor and outside receptor areas after turning on a thermal source above the surface. For these simulations, we used the model of quasi-steady heat transfer adapted to SThM measurements developed by Gorbunov et al., in 1999.

We assumed that the major component of the heat capacity and density of snake tissue is water and these parameters of water were applied for this simulation. As we tested, the variation of these parameters in a wide range changes numerical results insignificantly and does not affect principal conclusions.

The surface temperature variation during the thermal probe pre-heated to 35 – 65 °C approaching the surface as well as after turning on temperature on a thermal probe located above the surface was estimated (Figure 4.46, left). In approaching to the snake pit area, fast increase of surface temperature was observed down to the distance between probe and the surface of 5 μm . In contrast, surface temperature of the outside areas of pit receptors, increase slower pace (Figure 4.46, left). For comparison, the surface temperature of highly conductive materials; gold, and low thermally conductive materials; PEHD, were chosen to include this simulation. The surface temperature of gold in this simulation showed very slow pace rise until it reached to the surface. On the other hand, the surface temperature of PEHD showed much faster temperature saturation whose behavior is close to snake pit area. Obviously, low thermal conductivity of pit receptors prevents fast heat dissipation from surface area, therefore, initiates fast local temperature rise. Natural outcome of this uneven heating process is significant temperature gradient between pit and outside pit areas that can reach 3 °C (especially at large distances between probe and skin) for initial temperatures of the thermal probe of 40 °C (Figure 4.46, left). If the thermal source was turned on far from skin surface, the temperature gradient is established immediately, reaches 3 °C, and persists over a long time-period before the thermal equilibration takes place at $t > 100$ seconds (Figure 4.46, right). This behavior is very different from one expected for surfaces with highly thermally conductive properties like gold (Figure 46, right).

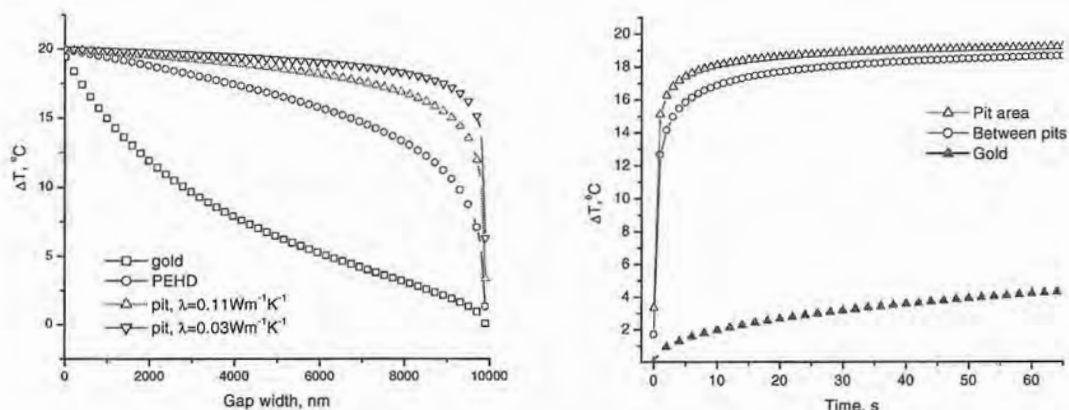


Figure 4.46. Variation of surface temperature for receptor and non-specific areas during approaching thermal tip pre-heated to 40 °C (left) and time-dependence of temperature gradient after turning on heat source (right).

4.4.2.3. Micromechanical properties

To compare micromechanical properties of pit receptor areas and non-specific skin areas, we conducted probing of surface compliance (elastic response) with the collection of multiple force-distance curves and the estimation of elastic modulus from repulsive part of these curves using Hertzian contact mechanics model (Tsukruk et al., 1998). In this mode, the lateral resolution was not high enough to resolve and separate nanomechanical behavior of nanopits. Instead, we receive surface distribution of elastic response that gives the average value of elastic modulus (Figures 4.47 and 4.48). An example, shown in Figure 4.47, demonstrates surface distribution of elastic moduli that shows 40 % of standard deviation typical for snake living tissue. From such array of nanomechanical responses, the representative force-distance curves as presented in Figure 4.49 (top) was selected. Initial curves were converted to penetration – normal load curves (Figure 4.49 (bottom)) that allows direct estimation of elastic modulus.

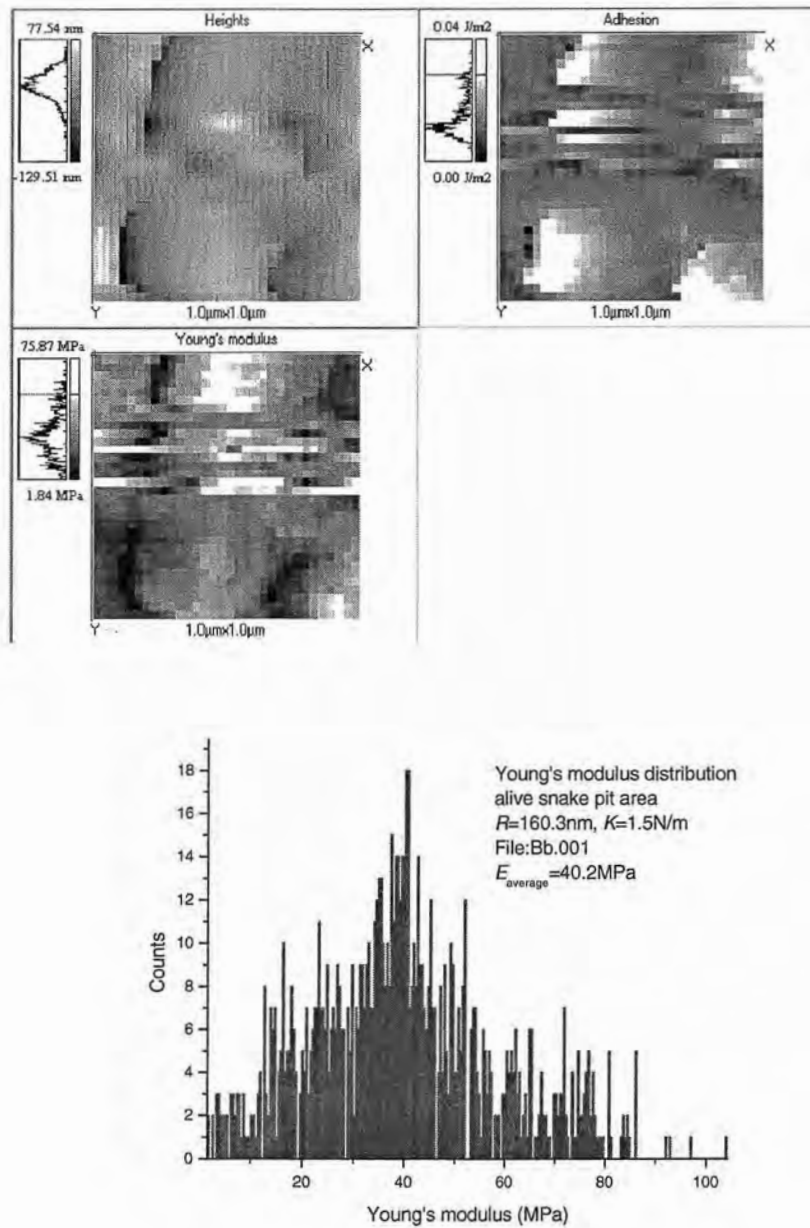


Figure 4.47. The surface Young's modulus (middle) and stiction (adhesion) (top-right) mapping corresponding to the pixel – by- pixel morphology image (top-left) and the distribution of Young's modulus values (bottom) using full-range penetration for pit area of alive Indian Python.

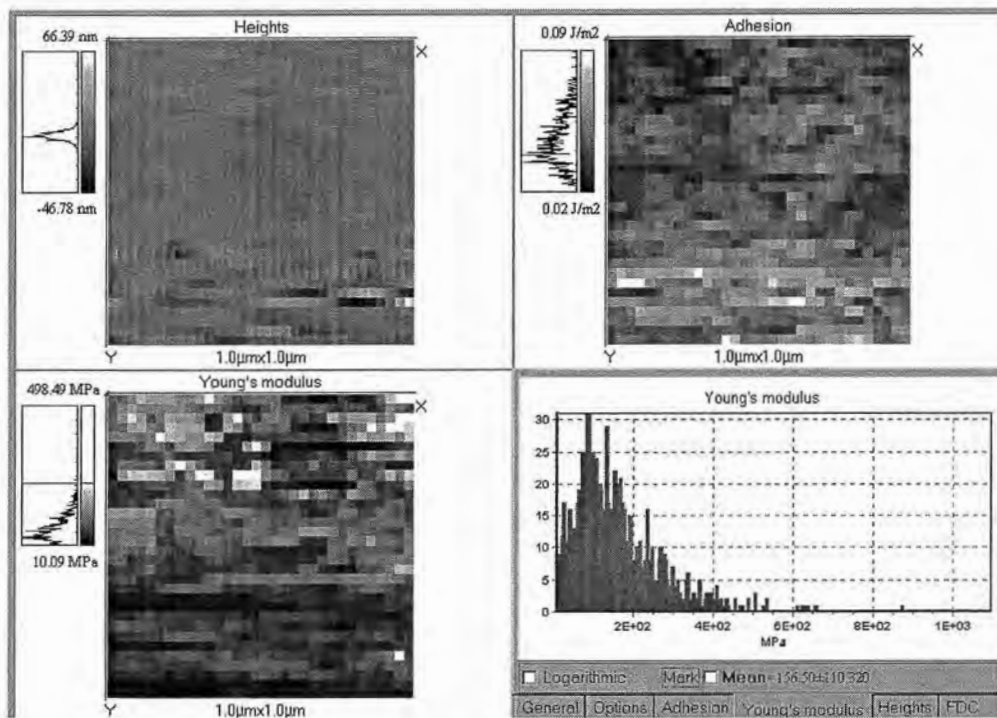


Figure 4.48. The surface Young's modulus (middle) and stiction (adhesion) (top-right) mapping corresponding to the pixel – by- pixel morphology image (top-left) and the distribution of Young's modulus value (bottom-right) using full-range penetration for non-specific skin area of alive Indian Python.

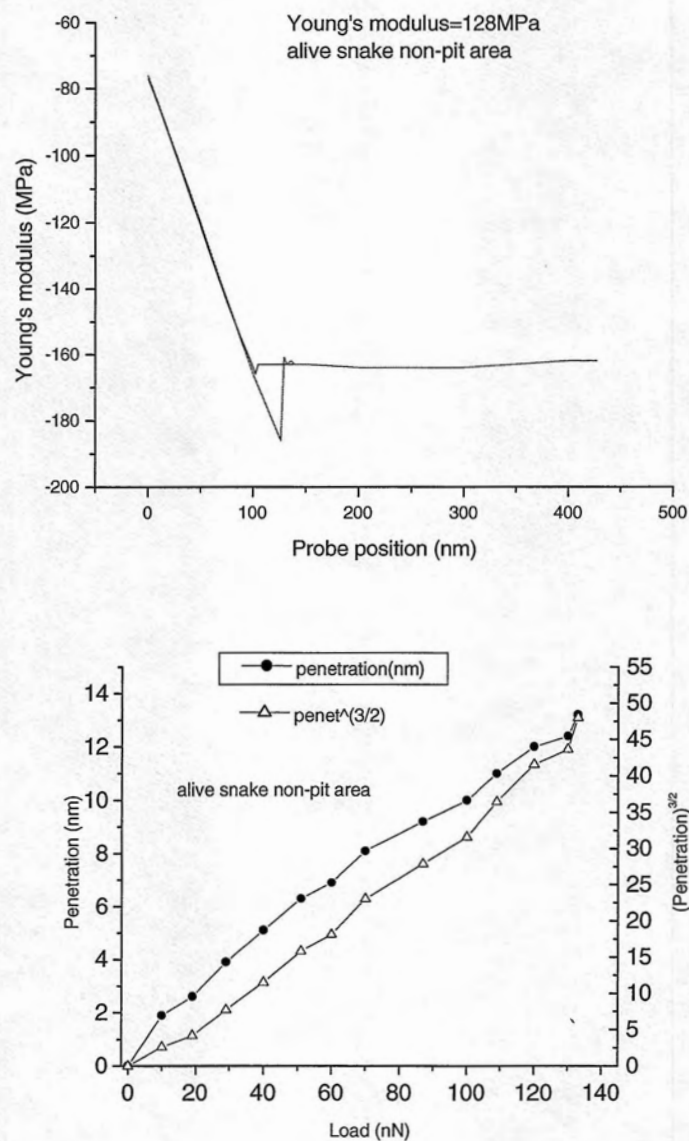


Figure 4.49. An example of force-distance curve (top) and the calculated penetration-load curve (bottom). Sample was alive Indian Python and the place was non-specific skin area.

In micromechanics measurement, pit area for Indian Python shows recognizable pit presence from pixel-by-pixel morphology image (Figure 4.47). In Young's modulus and stiction mapping, there are several noisy lines which are not accurate data. Comparing morphology image to Young's modulus mapping, it is clear that Young's modulus reflects morphology influence deeply. Higher morphology leads higher Young's modulus in Figure 4.47, which was caused by the difference of tip contact area. Smaller contact area of tip provides higher pressure on the contact area, which brings steeper force-distance curve. In the same manner, larger contact area can absorb more energy dissipation, which provides less pressure on the contact area. In this case, the slope of Young's modulus becomes smaller. This problem is very similar to the influence of geography for thermal conductivity distribution as was mentioned in chapter 4.3. Since higher place provides smaller tip contact area, and lower place such as bottom of valley provides larger tip contact area, Young's modulus is expected to be higher at higher place, and lower at lower place. On the other hand, stiction (adhesion) has opposite situation. The high place such as top of the hill has smaller contact area, so it provides less adhesion. The low place such as the bottom of valley provides more contact area, which leads higher adhesion as is seen in Figure 4.47 clearly.

Elastic modulus, calculated from such curves at different penetration depth, provides information about average elastic modulus of materials surface as well as possible presence of any depth gradients in micromechanical properties. Typical data for non-specific skin areas and receptor areas are presented in Figure 4.50. As clear from these data, micromechanical response is very different for pit receptors and for non-specific skin areas. First, skin outside receptor area is much stiffer with virtually no gradient of elastic modulus. Under given normal load, elastic penetration does not exceed 15 nm and the absolute value of elastic modulus is about 140 MPa with very significant surface distribution (Table III). Unlike, receptor areas are much more compliant and can be elastically deformed up to 1 – 2 μm (depth of indentation is technically limited to 2 μm because of the tip height) (Figure 4.49, bottom). Moreover, elastic modulus shows very significant depth gradient that corresponds to stiffer surface layer and much more compliant underlying material with average elastic modulus as low as 30 – 40 MPa for large indentations (Table III).

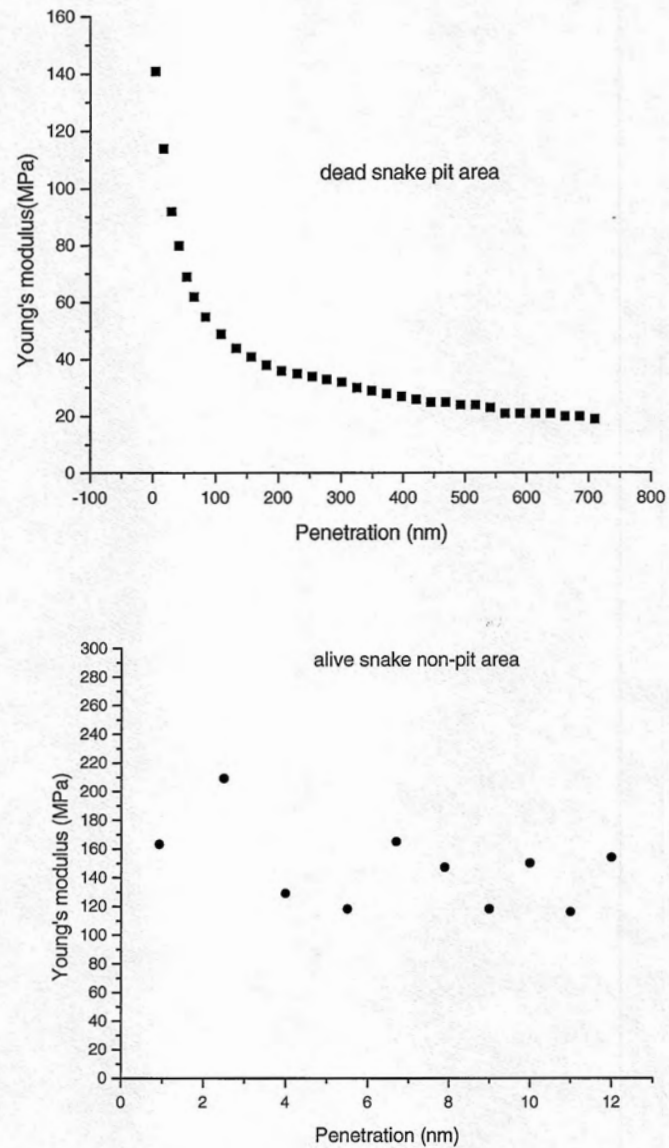


Figure 4.50. The penetration dependence of Young's modulus for IR receptor (top) and non-specific skin (bottom) area.

These results indicate compliant, “spongy”-like elastic behavior of pit receptor surface of living tissues with extremely large reversible deformations under modest normal loads. Initial higher stiffness can be associated with presence of the topmost cornified surface layer. For comparison, typical elastic modulus for crosslinked rubbers is in the range of 40 – 200 MPa. Very similar micromechanical behavior was also observed for formaldigaded snake skin. The values of elastic moduli obtained for Ball Python skin areas are close to ones reported above (Table III).

Therefore, the major conclusion of micromechanical testing is that snake skin in receptor areas is much more compliant than outside of receptor areas and possesses very significant depth gradient with stiffer surface layer and softer interior.

4.4.2.4. Tissue microstructure: preliminary data

A specific combination of morphological, micromechanical, and microthermal properties of snake IR receptors indicates that these areas are extremely smooth, with a large number of relatively large (hundreds of a nanometer) and deep nanopits, possess very surface thermal conductivity. The morphology and properties of the receptor areas are very different from non-specific snake skin located in the vicinity of the receptor areas. This non-specific skin is much stiffer with higher surface thermal conductivity and shows much finer nanopit array.

The combination of materials properties observed for receptors areas can be associated with microstructure of underlying tissue with developed microporous organization. In addition to current observations, our previous studies suggested that an interconnected micropore underskin net should exists to justify skin permeability for low-energy fluids (Hazel et al, 1999). In addition to this, high-resolution studies of tissue cross-section reveal fine layered microstructure of the topmost cornified skin layer with crack-like features.

To gain additional input on possible tissue microstructure of IR receptors, additional preliminary study on underlying tissue was conducted, which exposed by removing topmost skin layers. In this way, underlying tissue can be exposed at the depth from a micrometer to several tens of a micrometer (Figures 4.51 – 4.53) taken by J. Hazel, Western Michigan University)

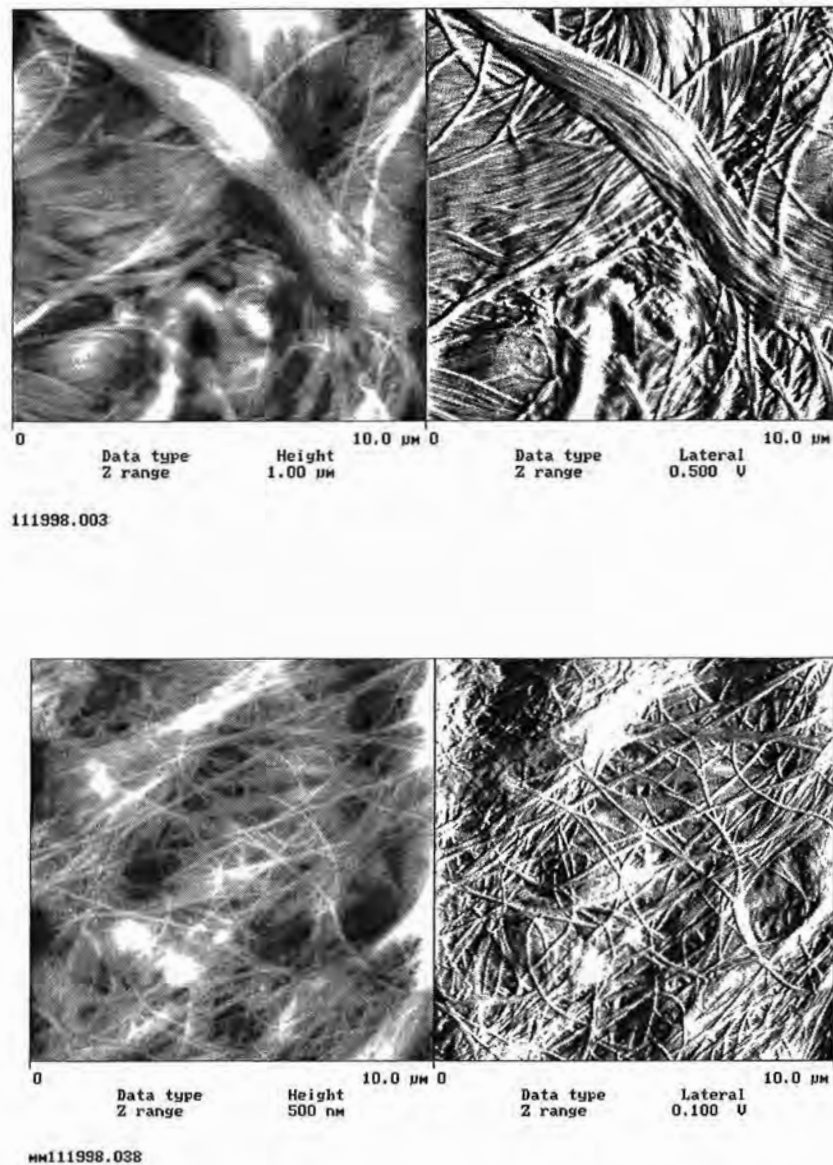


Figure 4.51. AFM scanning image of underlying tissue of snake IR receptor area, which demonstrates collagen fibers taken by John Hazel, Western Michigan University.

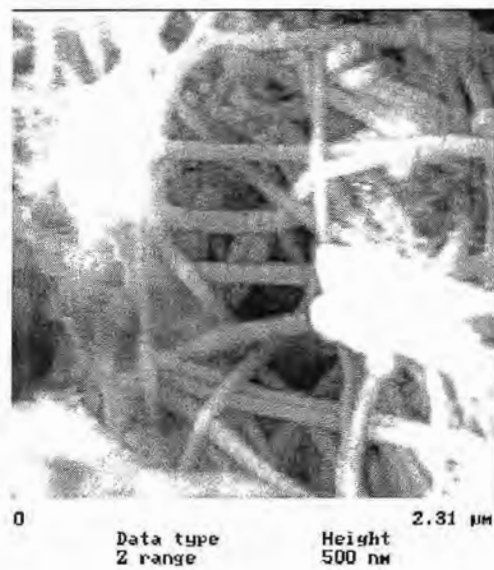
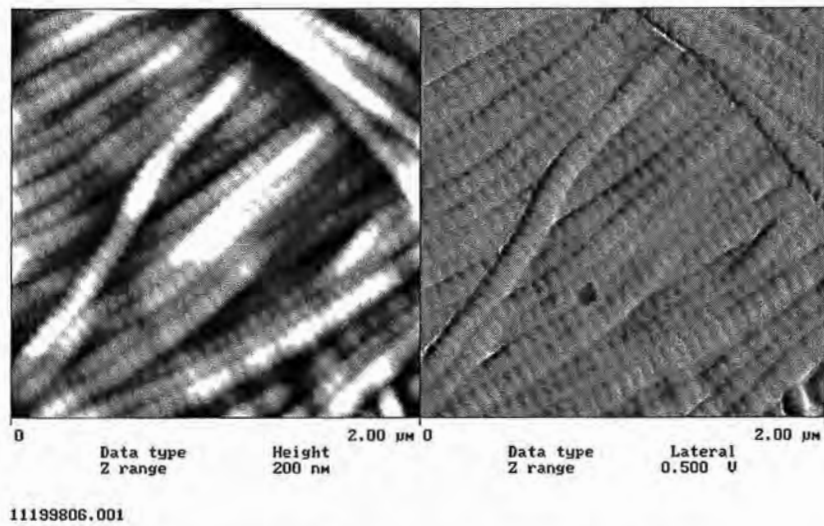


Figure 4.52. AFM scanning image of underlying tissue of snake IR receptor area taken by John Hazel, Western Michigan University.

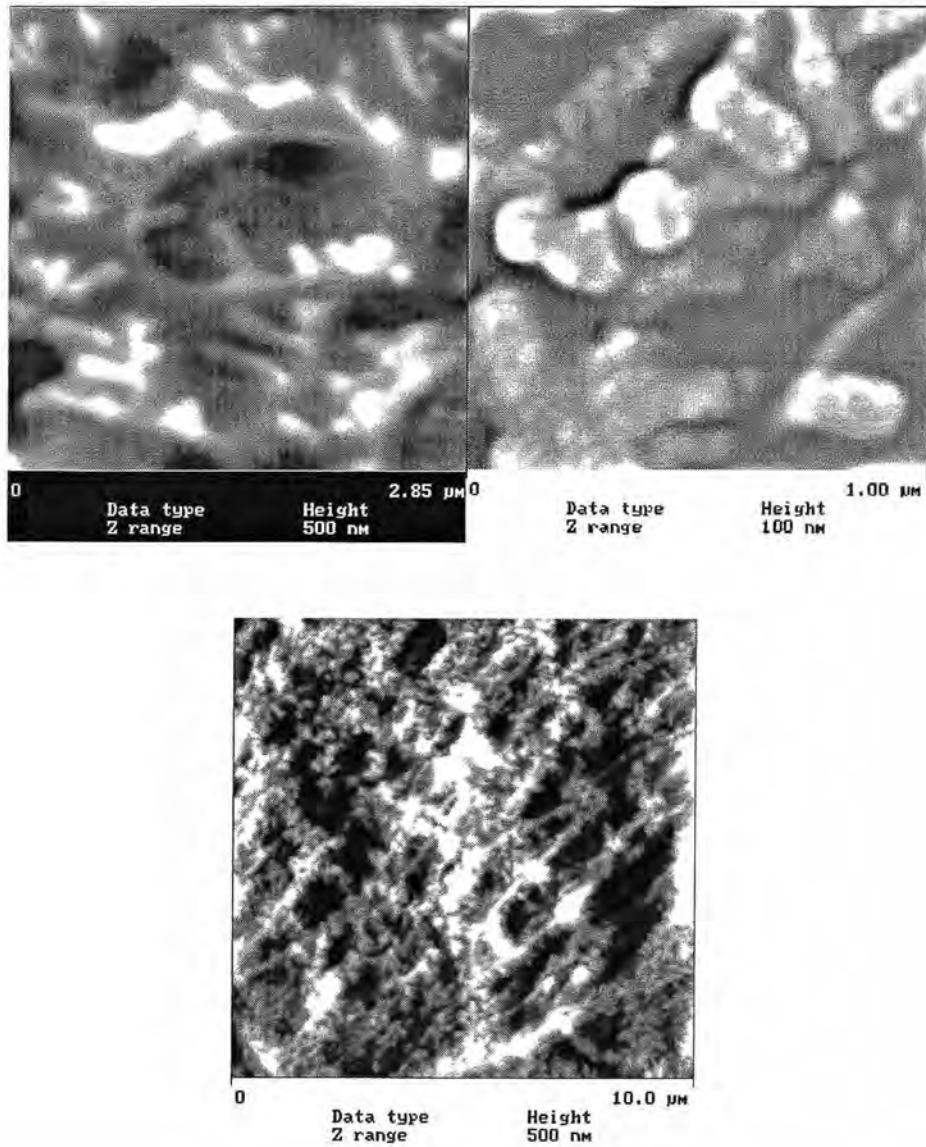


Figure 4.53. AFM scanning image of underlying tissue of snake IR receptor area taken by John Hazel, Western Michigan University.

These sections show two primary types of tissue organization: very branched and random network of fibrillar structure and cellular-like microstructure formed by short-branched morphological features. First type of microstructure is composed of collagen-based microfibrils of about 130 – 145 nm across and very regular periodicity along the fibril axis of 60 – 80 nm and is observed at deeper levels (Figures 4.51 – 4.53)

Highly developed cellular morphology is observed in the proximity to the surface and reminds the ending of nerve fibrils (Figure 4.53) Level of porosity is within 30 – 70 % for various locations and pores possess a wide distribution of sizes with average value about or below 1 μm . The nature of these microstructures will be a subject of further investigations, and here, we only would like to point out on highly porous character of both organizations that confirms our suggestion on microporous internal microstructure of tissue material within receptor areas.

This micropore, microfoam-like tissue structure explains very high compliance of pit areas in comparison with non-specific snake skin areas with thick cornified layer. From standpoint of microthermal properties, microvoids with low thermal conductivity (λ_{air} is an order of magnitude lower than any organic material) should significantly reduce overall thermal conductivity of pit receptors.

4.4.3. Conclusions

In conclusion, we characterized surface morphology of IR receptor areas obtained for both living tissue and chemically treated tissue with SPM technique under humid environment condition. The geometrical parameters of characteristic nanopit morphology under these preparation conditions are very similar, however, it seems that the values obtained for diameter, depth, and spacing of nanopits under dried, high-vacuum conditions are significantly (several times) smaller than ones observed under wet conditions.

Combined measurements of micromechanical and microthermal properties and tissue microstructure revealed much higher compliance and lower surface thermal conductivity of receptor areas as compared to non-specific skin areas in the vicinity of snake pits. We suggest that the observed characteristic difference is caused by microfoam-like microstructure of tissue within receptor areas with extremely high microporosity level.

Very low surface thermal conductivity provides excellent isolation for the heat dissipation from the receptor area that results in fast rising of local surface temperature within pit areas. In turn, the neighboring non-specific skin areas with higher thermal conductivity dissipate thermal energy faster, thus, they are not heated up to the same level. This difference in heat dissipation processes gives rise to the temperature gradient between receptor skin and neighboring non-specific skin areas. This temperature gradient combined with close proximity of terminal nerve mass to skin surface provide efficient mechanism for high sensitivity of photothermal detection. Array of surface nanopits may also serve for the reduction of effective thermal conductivity (damping lateral heat dissipation) in addition to their function as selective optical filter as was suggested earlier (Campbell, 1999).

We believe that similar mechanism of heat detection exists in other types of snakes such as Crotaline snakes where thin free-suspended membrane is separated from bottom of heat receptor by air reservoir with very low thermal conductivity.

4.5 Microthermal Analysis of Polymer Ultrathin Films

The result of microthermal studies of ultrathinpolymeric films deposited on a silicon substrate is presented. The microthermal analysis of ultrathin polymer films is conducted to elucidate limits of applicability of this technique in studying their microthermal properties, and observing thermomechanical response during local heating for films with thickness above 10 nm. The glass transition temperature of ultrathin polystyrene films deduced from these experiments decreases for film thickness below 400 nm. For the thinnest PS film with clearly detectable microthermal response (25 nm), the glass transition temperature is 20°C below its bulk value. Our estimation of the heat dissipation within the tip-surface contact shows that observed μ TA response for polymer films is associated mainly with temperature-induced elastic variation of the contact area.

4.5.1. Experimental

The sample for investigations was polystyrene with molecular weight $M_w=220,000$, $Q=2.7$ (Aldrich) as measured by GPC. DSC measurements at 30 °C/min show glass transition temperature for bulk PS at 103 °C. Ultra-thin polystyrene films with thickness 3, 6,

10, 25, 50, 100, 200 and 400 nm were prepared on silicon wafers by spin-coating technique. The silicon substrate was a highly polished (100) wafer with silicon oxide thickness of 1 nm. Before spin-coating, the silicon surface was cleaned with pirania solution.

For μ TA measurement, we employed Explorer PS system from Thermomicroscopes, Inc. In the experimental scheme for polymer ultra-thin films, reference probe was placed on the silicon substrate (Figure 4.54). The thickness as thin as less than 30 nm is extremely thin for μ TA system. For example, the dissipating heat from thermal probe passes through thin film on silicon substrate very quickly and the heat is absorbed in silicon substrate. As a result, the thermogram of polymer thin film taken in this scheme shows mostly the behavior of silicon, although actually this thermogram includes information of polymer thin film as well. The information on polymer thin films is too small compared to that of silicon. In order to take the information only on polymer, our scheme; to place probe onto the silicon substrate, was introduced. In this new scheme, during measurement, the dissipating heat from thermal probe is absorbed in silicon surface for both of probes, so after differentiating the both signals, only thermal signals caused by polymer will be appeared.

With modified measurement setup, the thermal sensitivity of the main thermal probe increased dramatically, thus, allowing detection of minute heat dissipation variations (<1 μ W) associated with polymer film itself. The baseline was recorded prior to μ TA measurements by using two identical bare silicon substrates. All measurements were conducted from room temperature up to 300 $^{\circ}$ C. μ TA was calibrated by using standard procedure (TA Instruments, Inc., 1999). The “optimal” heating rate of the thermal probe (10 $^{\circ}$ C/sec) was selected based on the best visualization of the transition points on μ TA data plots. DSC measurements were conducted on a Perkin Elmer instrument. The samples for calibration were selected to present materials with known glass transition (T_g) or melting (T_m) temperatures (Table IV). For calibration, we used polystyrene (PS), high-density polyethylene (PEHD), and polyethylene terephthalate (PET). All polymers were analyzed according to standard DSC routine at heating rates from 20 to 40 $^{\circ}$ C/min to identify glass transitions and melting temperatures. The T_g for HDPE was taken from the database, MatWeb.

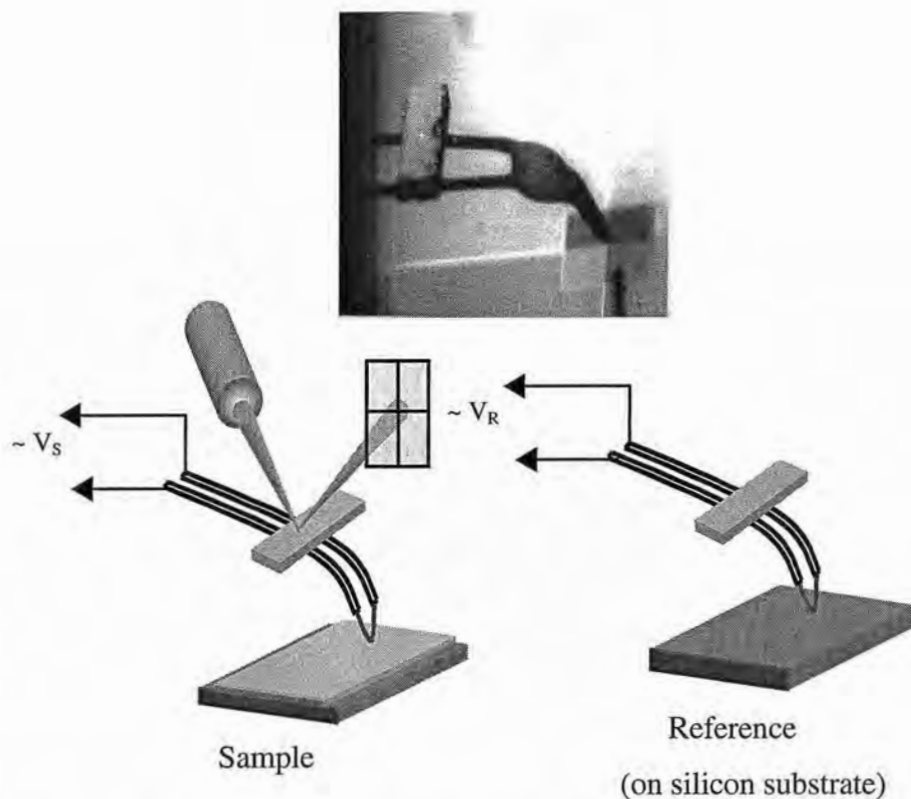


Figure 4.54. Sketch of the SThM detection scheme for ultrathin films measurements (right) and the micrograph of the actual thermal probe (left).

Table IV. Glass transition and melting temperatures as measured by μ TA.

Polymers	T_g , $^{\circ}\text{C}$	T_m , $^{\circ}\text{C}$
polystyrene (PS)	103	–
high-density polyethylene (HDPE)	-110 *	131
polyethylene terephthalate (PET)	78	263

* Literature data [from MatWeb]

4.5.2. Results and Discussion

To test the rate-dependence of μ TA response, the microthermal signal for the bulk sample of PET (Figure 4.55, top) and PS film with 200 nm thickness (Figure 4.55, bottom). Melting temperature of PET increases from 256 °C for low heating rate (1°C/sec) to 264 °C for high heating rate (5 °C/sec) to 111 °C for high heating rate (25 °C/sec). Glass transition temperature is measured from μ TA data as onset of a rapid probe deflection in accordance with the known approach for thermomechanical measurements (Haines, 1995).

We collected thermal data for PS films with different thicknesses at the fixed heating rate of 10°C/sec (Figure 4.56). As clear from these data, in our experimental design, the glass transition temperature can be unambiguously detected for PS films thicknesses below 400 nm. For 25 nm thick PS film, which is close to undisturbed coil dimensions ($2R_g=14$ nm), the microthermal response is smeared, however, the change of slope at glass transitions still can be detected for this film. For samples, with the thickness well below the unperturbed macromolecular chain dimensions (10, 6, 3 nm), thermal response follows closely the baseline and glass transition temperature cannot be detected in this experimental design. Possible experimental reason can be that high thermal conductivity of the silicon substrate prevents the detection of minor modulations related to monomer thick PS films. On the other hand, glass transition itself becomes much less defined for highly collapsed macromolecular chains (Overney, 2000).

The variation of glass transition temperature of ultrathin PS films deduced from μ TA experiments is presented in Figure 4.57. As this data demonstrates, the glass transition temperature significantly decreases when the film thickness decreases below 200 nm. For the thinnest film presented in this plot (25nm), the glass transition temperature decreases by 20 °C from its bulk value. These results follow general trends known for ultrathin polymeric films deposited on solid substrates with weak film-substrate interactions (Beaucage, 1993, Jiang, 1999, and Keddie, 1994). Theoretical considerations relate the decreasing glass transition temperature to increasing free volume caused by distorted packing of macromolecular chains under confined conditions.

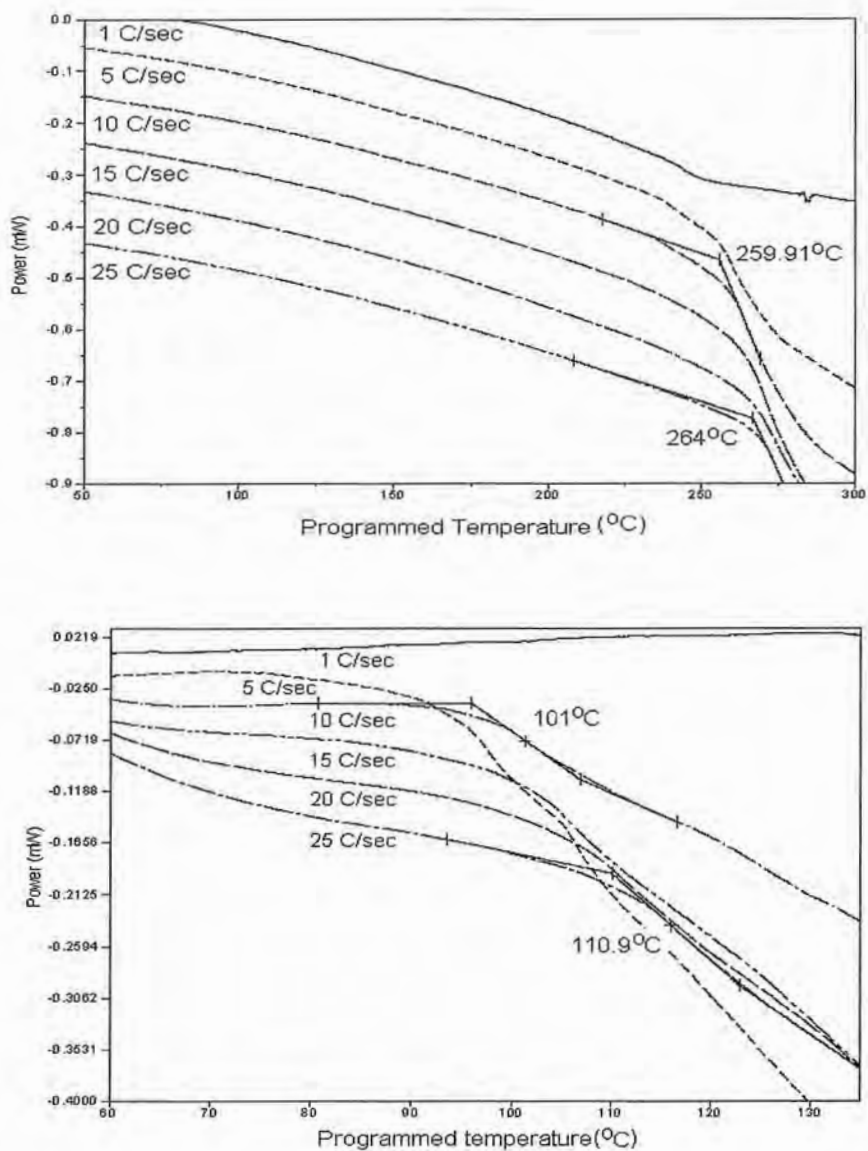


Figure 4.55. Microthermal probing of bulk sample of PET (top) and PS film with 200 nm thickness on silicon substrate (bottom) at various heating rates. Data plots are offset along y-axis.

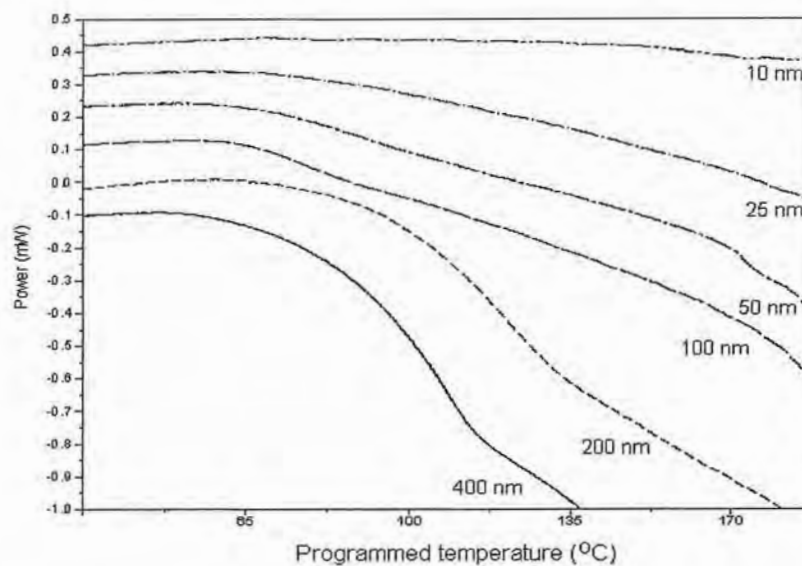


Figure 4.56. μ DSC of the PS films with different thicknesses on silicon substrate (data plots are offset along y-axis)

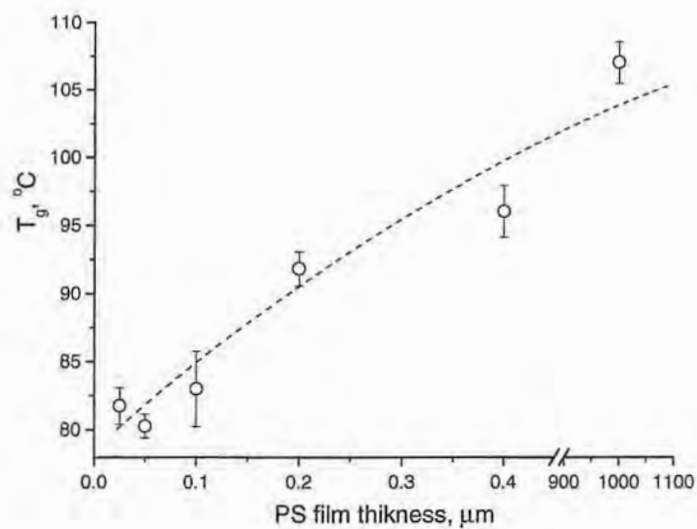


Figure 4.57. The variation of glass transition temperature for PS films with different thicknesses.

This data demonstrate the sensitivity of present μ TA design for probing nanometer thick polymer films comparable with other techniques but complimented with micromapping capabilities with submicrometer lateral resolution (Gorbunov, 1999).

The change of surface thermal properties at the glass transition temperature can be associated with both changes in thermal conductivity (heat capacity) and elastic deformation in the contact area of the thermal tip. To estimate what contribution defines the microthermal response detected by μ TA probing, we applied the model of quasi-steady heat transfer in the point of elastic contact developed earlier (Gorbunov et al., 2000). As we demonstrated, this model can be applied to SThM measurements of polymeric surfaces because elastic deformations are very small under given normal load and time of measurements is much shorter than the rate of heat dissipation.

From equations (9) and (11), we estimate the micromechanical contribution for PS films by using the ratio of heat dissipations below (glass) and above (rubber) glass transition in the form:

$$\frac{Q_r}{Q_g} = \frac{\lambda_r \cdot R_{c,r} \cdot T_r}{\lambda_g \cdot R_{c,g} \cdot T_g} \approx 5 \quad (12)$$

Here, $R_{c,r}$ and $R_{c,g}$, are the radius of contact area by thermal probe onto rubber and glass state respectively. This ratio is estimated from the temperature dependence of elastic moduli for PS material ($E_g/E_r \sim 10^2$), thermal conductivities ($\lambda_r/\lambda_g \approx 0.9$), and for $T_g/T_r = 300\text{K}/400\text{K}$ (Sperling, 1992 and Van Krevelen, 1997). This estimation shows that the heat dissipation, associated with thermo-mechanically driven increase of the contact area, should increase by 4 – 5 times after the transition from glassy to elastic state. Indeed, experimentally observed increase is 3 – 6 times for different PS films. This is fairly close to estimated micromechanical contribution due to the temperature variation of elastic materials properties. Therefore, our estimations support conclusion that observed μ TA response for polymer films is associated, mainly, with elastic thermomechanical variation of the tip-surface contact area. On the other hand, we demonstrated that μ TA is a powerful tool for the direct measurement of microthermal properties of nanometer thick polymer films. As we showed before (Gorbunov et al., 1999, 2000), the lateral resolution of the thermal imaging

mode is on a sub-micrometer scale. Therefore, the combination of modified μ TA routines with SThM imaging enables microthermal mapping of nanocomposite materials.

4.6. Calibration of the Cantilever Spring Constant

As was already described in chapters 4.3 – 4.4, many micro-mechanical measurement have been done in this project. In micromechanics measurement, the most critical issue is to obtain the spring constant of the cantilever in AFM tip as accurate as possible. The reason is compared to other parameters, the spring constant of cantilever is much more influential in calculation of the surface Young's modulus as is clear from the following equation (Hertzian model; Chizhik, 1998).

$$E = \frac{3}{4} \cdot \frac{1-\nu^2}{R^{\frac{1}{2}}} \cdot \frac{k \cdot Z_{defl}}{h^{\frac{3}{2}}} \quad (13)$$

Here, E is Young's modulus, k is the spring constant of cantilever, R is the tip radius, Z_{defl} is cantilever deflection, and h is penetration depth (Chizhik, 1998). In equation (13), k (spring constant of cantilever) is proportional to the Young's modulus while R is more ineffective mathematical shape to the result of Young's modulus. From this thought, we should be concerned about how to obtain most accurate spring constant of cantilever. In the course of this work, we established the experimental procedure for the calibration of spring constant and SPM tip radius.

4.6.1. The cantilever – against – cantilever measurement

There are two ways to get the spring constant of cantilever. One is direct measurement using two AFM tips, and another is to make use of resonant frequency. Simplest and most reliable one is direct measurement, so-called “cantilever – against – cantilever” measurement (Figures 4.58 and 4.59).

The idea of direct measurement is, by making use of the constant – known cantilever, probing onto another constant – unknown cantilever and measuring the force – distance curve.

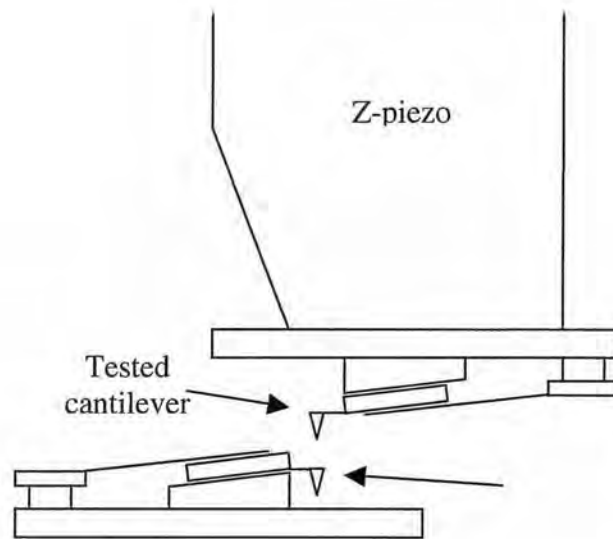


Figure 4.58. The scheme of cantilever – against – cantilever spring constant measurement.

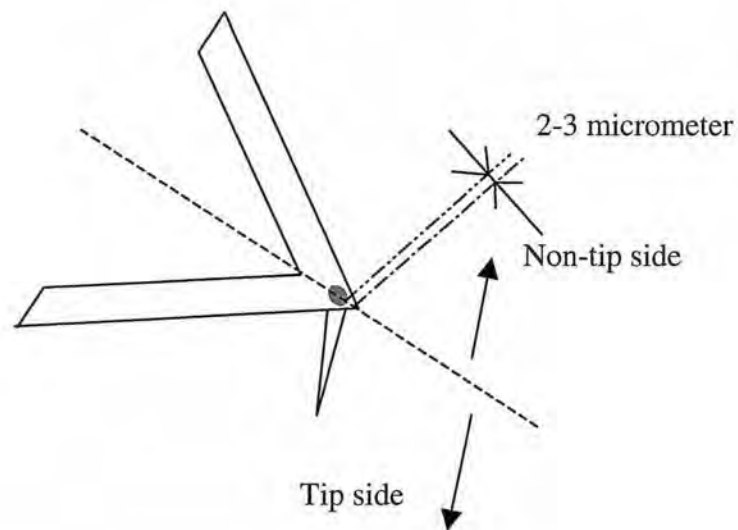


Figure 4.59. The position of the tip on v-shaped cantilever.

The force – distance curve will be converted to the penetration – load curve whose slope is correlation coefficient for the spring constant of this probe.

The resonant frequency of the AFM tip gives us crucial information on the spring constant of cantilever (Cleveland et al., 1992, Sader et al, 1999, and Hazel et al, 1999). In obtaining the resonant frequency, several factors should be considered seriously. First of all the shape of cantilever is mentioned. Usually AFM tips consist of two types of the cantilevers; rectangle straight beam and V-shaped cantilevers. V-shaped cantilevers are popular for many researchers due to the toughness for the measurement, and flexibility for unexpected morphology condition. There aren't much work in the field of the measurement of the spring constant of cantilever which is concerned about this tip geometrical difference. Hazel et al. brought new perspective to measure the more accurate spring constant of cantilever by taking account the geometrical problem and the structure of the tip in 1999. As other factors, weight of the cantilever, and temperature of the cantilever are important (Walters, 1996). The principle that different weight has different resonant frequency provided one method for cantilever spring constant measurement (Cleveland et al., 1992).

Cleveland added a tiny tungsten sphere on the AFM cantilever one by one, and measured the resonant frequency using different weight (Figure 4.60). This method works very well with the deviation of spring constant from 10 – 20 % while other methods usually provide 50 – 200 % deviation. Taking into account the technical difficulty in this method, this still deserves to be a standard for the spring constant of cantilevers.

The frequency measurement at different temperature seems to be another interesting way to attempt (Walters et al., 1996). Although this temperature method requires additional install of hardware such as Q-factor generator, experiment itself is clearly non-destructive, time-saving, and user friendly system. Nowadays, to make use of temperature in this kind of experiment is getting more and more popular among research laboratories. Technical challenge in temperature control enormous for AFM since z-piezo ceramic has fairly strict physical constrain such as capability up to only 150°C.

In terms of economical and reliable method, the direct cantilever - against - cantilever method, and tungsten added mass method are the best ones for research laboratories. Here we report the reliability and simplicity of this method.

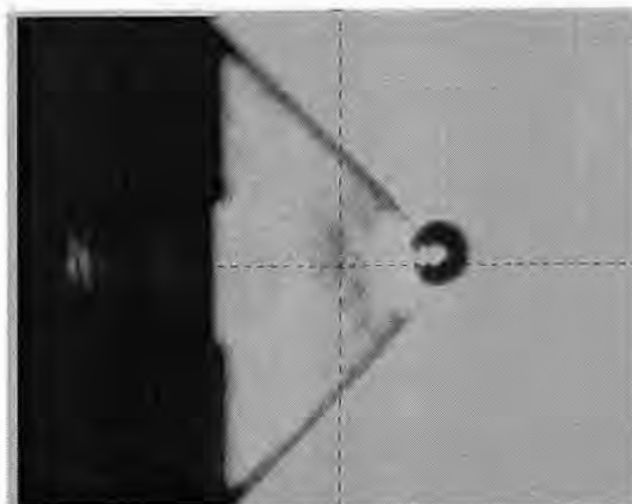


Figure 4.60. The cantilever of AFM with tungsten added mass.

In terms of experimental procedure, tested cantilever is mounted on a tip holder with z-piezo ceramic tube, which means tested cantilever comes to upper position, unknown cantilever comes to lower position. Unknown cantilever is mounted on another tip holder (recommended), keeping the tip-side down (Figure 4.58) to avoid the crush of tip to tip.

Measure the force-distance curve using silicon substrate to take the sensitivity of the tip and save this file to refer accuracy of sensitivity. The parameters are optimized such as follows; trigger threshold=15nm, setpoint=0.01V, z-range=60 nm, absolute mode (setpoint and z-range are changed by user's choice.) Take at least two data at different place to make sure the data is fine.

Next is the measurement of the force-distance curve on the unknown cantilever. First locate the unknown cantilever below the tested cantilever. At this time, make sure there is enough space between upper and lower tips since it is so easy to crush those tips not noticing it. Then locate the unknown cantilever parallel to the tested. By looking at those tips from in front, and from left side, more or less lower tip should be located reasonably. Next is to look at the lower tip through optical system in DI microscope. Easiest way is to use lowest zoom which allows user to have widest view. After finding the tip, zoom and focus the tip surface. Now engage the tip onto the tip surface. Since a tip is located on just 2-3 micrometer inside

from the very edge of the cantilever (Figure 4.59), positioning the tip should be done carefully. Final adjusting can be done using x- and y- offset function in AFM. In this measurement, setpoint is recommended to use as low as 0.01 V. During engaging the tip, you need to always look at the optical system's monitor in order to see if tip is going to break or not. If you observe the tip is bent too much, abort the measurement immediately. Then try engage again. Recommended parameters here are the same as silicon's measurement. In the cantilever - against – cantilever measurement, be always careful of the situation of the tips through optical monitor.

Data analysis is done using the Micro Mechanical Analysis (MMA) Software. To confirm the sensitivity of the measurement system, open the silicon file which was obtained at first. Then click on the calibration tag and measure the slope of the force-distance curve. See whether the slope shows about 1 or not. (If not, you may have forgotten the sensitivity measurement in DI software.) If everything is fine, use this sensitivity for the data analysis of tip-to-cantilever measurement. After opening the file of tip-to-cantilever measurement, obtain penetration curve using MMA software, then calculate the slope of the penetration curve. After this whole procedure, the spring constant is calculated by following equation;

$$K = \frac{k_{test}}{slope} \quad (14)$$

Here K is divided by the slope. If tested cantilever is located at lower position, equation (14) becomes;

$$K = k_{test} \cdot slope \quad (15)$$

Actually locating the tested cantilever at lower place is better in terms of experiment. In this case, experimentalists don't need to take z-piezo off from time to time, which will lead experiment faster and more accurate due to the consistency, however, the drawback is we can not measure the frequency of fresh tip. The frequency of those tips are very important for data analysis. Looking at correlation between the spring constant of cantilevers

and the frequency will give us clear idea that how frequency affects the spring constant. So after finishing the cantilever – against – cantilever measurement, the resonant frequencies of the cantilevers are measured one by one.

After all, the spring constants of cantilevers are plotted as a function of (resonant frequency)³, which is supposed to show linear relationship (Cleveland et al., 1993) (Figures 4.61 - 4.63). This measurement was done for Si₃N₄ coated Si cantilever of contact mode with both long and short cantilever, and non-contact mode with short cantilever.

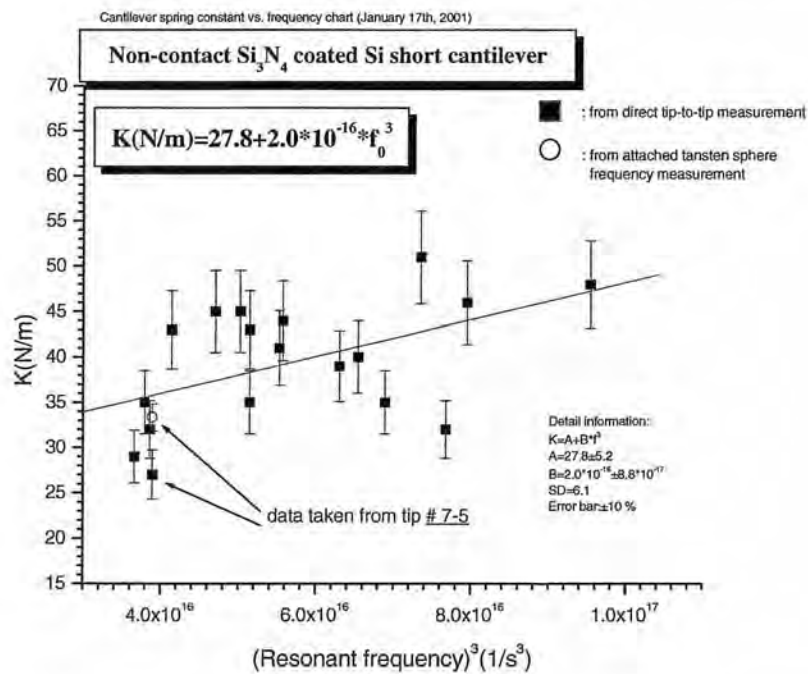


Figure 4.61. The spring constant of cantilevers versus (resonant frequency)³ for non-contact Si₃N₄ coated Si short cantilever.

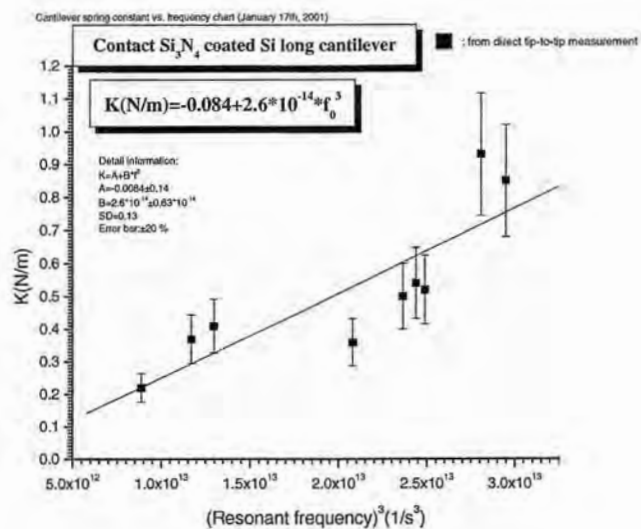


Figure 4.62. The spring constant of cantilevers versus $(\text{resonant frequency})^3$ for contact Si₃N₄ coated Si long cantilever.

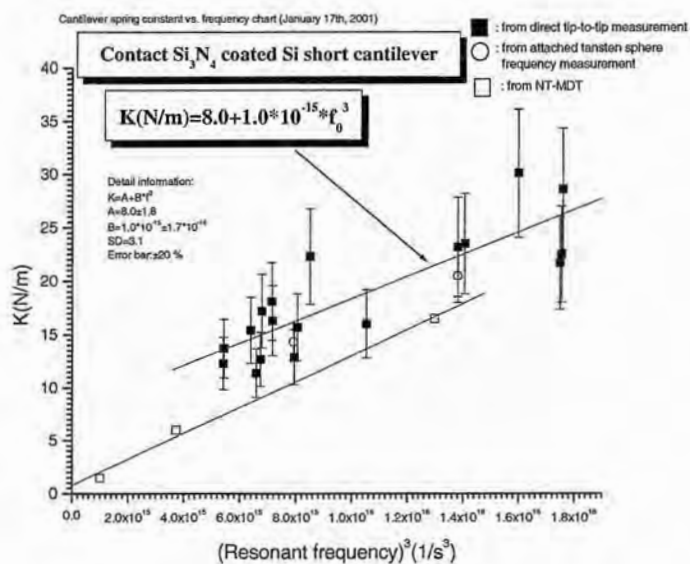


Figure 4.63. The spring constant of cantilevers versus $(\text{resonant frequency})^3$ for contact Si₃N₄ coated Si short cantilever.

4.6.2. Added end mass method using tungsten micro-sphere.

When an end mass m^* is added to the whole entire mass of the cantilever, the resonant frequency is given by (Cleveland, 1992);

$$f = \frac{\omega}{2\pi} \sqrt{\frac{k}{M + m^*}} \quad (16)$$

Equation (2) can be rearranged to give;

$$m^* = k(2\pi f)^{-2} - M \quad (17)$$

From equation (17), if several different mass are added to the cantilever and are measured the resonant frequency, the slope of the m^* versus $1/(2\pi f)^2$ will be the spring constant of cantilever (Figure 4.64), and the negative intercept will be entire mass of the original cantilever (Cleveland, 1992).

As the sample cantilevers, silicon cantilever for non-contact mode, silicon cantilever coated by Si_3N_4 for both contact and non-contact mode were chosen (NT-MDT, Inc.). The long cantilevers were not employed for this measurement due to the unavailability for this experiment. Long cantilevers has less toughness and are likely to bend with added tungsten mass, which makes resonant frequency measurement less accurate.

On near end of a fresh slide glass, tungsten spheres were placed. Very gently those spheres were nudged by clean paper to push off some of spheres. By doing so, some of the spheres were connected to the very edge of the slide glass and form straight row towards outside because of the extreme high surface energy of the edged surface. Now that there is some spheres to pick up by AFM tip, the cantilever was located beneath the spheres and raised up very slowly. After making sure sphere is placed on the end of the cantilever (Figure 4.60), the resonant frequency was measured. In order to know the diameter of the tungsten sphere, optical micrograph was taken by AFM optical system as well (Figure 4.60)

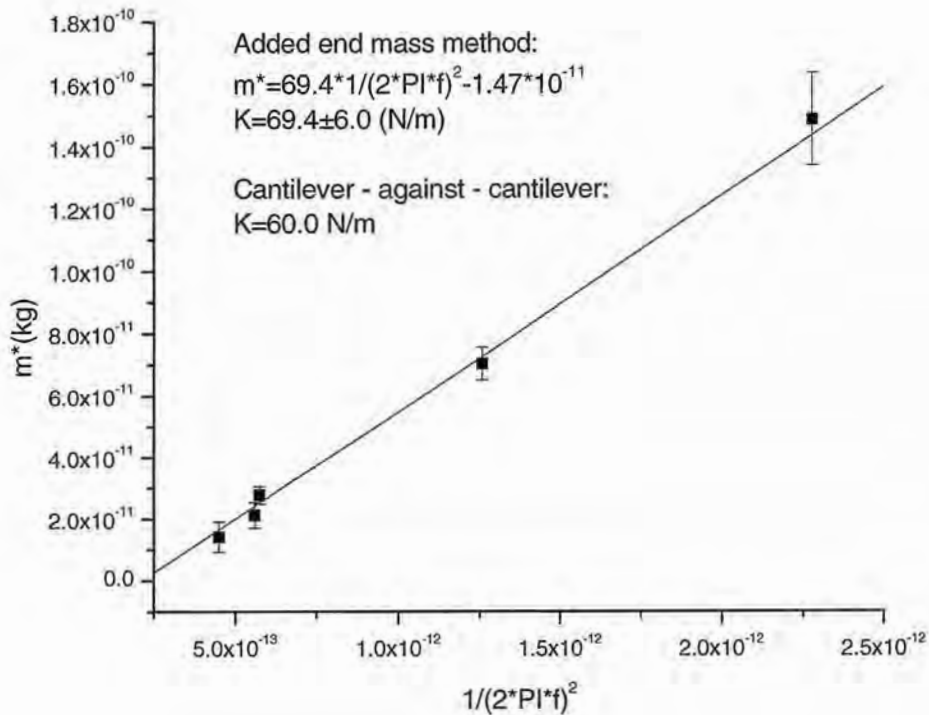


Figure 4.64. The result of added end mass measurement using silicon cantilever. Slope is the spring constant of cantilevers.

The value of diameter is used for calculation of the mass of the tungsten sphere. After whole measurement, data was analyzed to calculate the spring constant of the cantilever and was compared with the spring constant of cantilever obtained by cantilever – against – cantilever method

Figure 4.64 demonstrates the result from silicon non-contact mode short cantilever. The regression analysis demonstrates very small deviation from the generated linear curve. The standard deviation of the regression analysis is within 10 %, which is outstanding accuracy in the determination of spring constant of AFM cantilever. Usually the determination of spring constant of AFM cantilever provides $\pm 100\%$ error (Cleveland et al, 1993), so from this fact, it is clear that how this method is critical as the reference data for

other measurements. Other cantilevers such as silicon cantilevers coated by Si_3N_4 also demonstrated the same level of accuracy using this method.

The spring constants obtained by the added end mass method were compared to the spring constants obtained by the cantilever – against – cantilever measurement (Table V and Figure 4.65). The spring constants of cantilevers obtained by both methods show close values within 10 - 17 % difference. Our measurement of spring constant of cantilever by cantilever – against – cantilever with constant – known – cantilever is confirmed by frequency method which is completely independent of constant – known – cantilever. This indicates our experimentation of cantilever – against – cantilever was reasonable and the constant – known – cantilever purchased from a company provided reliable value originally (NT-MDT, Inc).

In reality, the humidity and temperature of experiment room is extremely important for cantilever – against – cantilever spring constant measurement. The water in air is easily condensed onto the AFM tips, and increases the adhesiveness of the cantilever. The sticky surface will destruct the accurate force – distance curve measurement at probe pull-off the surface point. Also for added – mass method, water molecule will be additional weight for the probe which will cause inaccurate frequency measurement.

Table V. The spring constants of cantilevers from added end mass method and cantilever – against – cantilever method corresponding data of Figure 58.*

	K(N/m)	K (N/m)
	Added mass	Cantilever-against-cantilever
Silicon non-contact “short”	69.4±6.0	60.0±6.0
Silicon coated with Si_3N_4 for contact mode “short”	14.4±0.3	12.9±0.1
Silicon coated with Si_3N_4 for contact mode “short”	20.5±0.08	23.2±2.3

*Only short cantilevers were employed for added end mass measurement due to the availability for experiment.

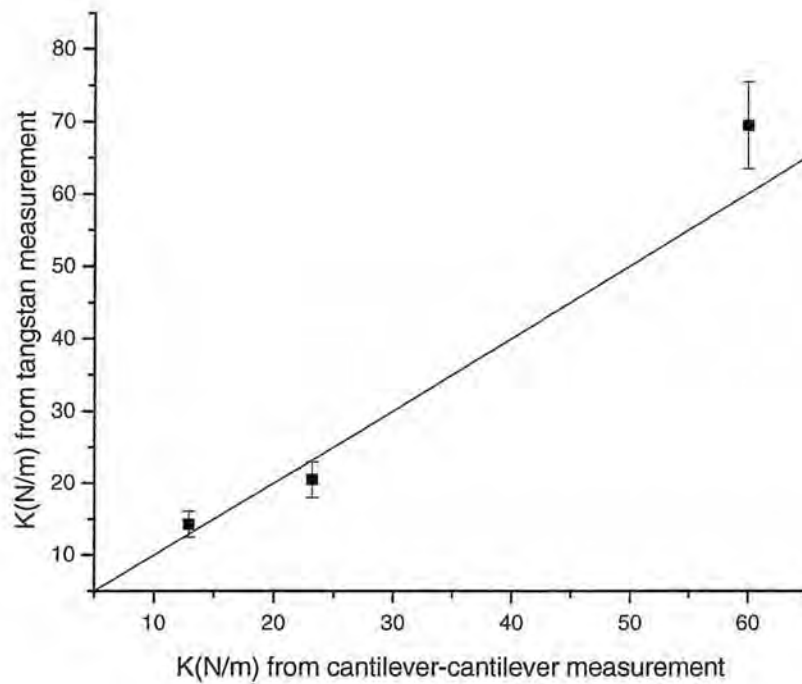


Figure 4.65. The plot of spring constants of cantilevers obtained by added end mass method versus the spring constants of cantilevers obtained by cantilever – against – cantilever method. The data are from Table V.

4.6.3. The tip radius measurement

For accurate calculation of Young's modulus (equation (13)), a tip radius plays an important role. For reasonable AFM scanning, small tip radius and good sphere shape are necessary. In micro-mechanics measurement, sometimes the tip radius is desirable to be small, and sometimes to be large, depending on the purpose, and sample condition (i.e. thickness, structure, humidity, and Young's modulus).

To obtain the tip radius, we employed the gold nano-particle AFM scanning image method (Vesenska et al., 1993). Gold particles were purchased from Tedpella, Inc. Gold particles are dispersed on the fresh flat mica surface. Then after scanning gold nanoparticle by AFM (Figure 4.66), the image is analyzed (Figure 4.67)

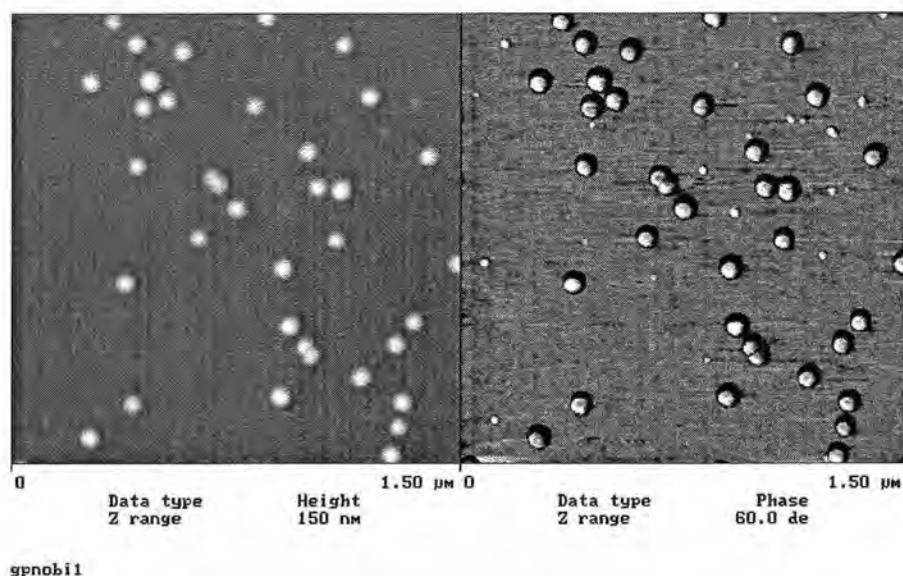


Figure 4.66. Scanning image of gold nanoparticles by AFM. The average diameter of the particles were 28 nm.

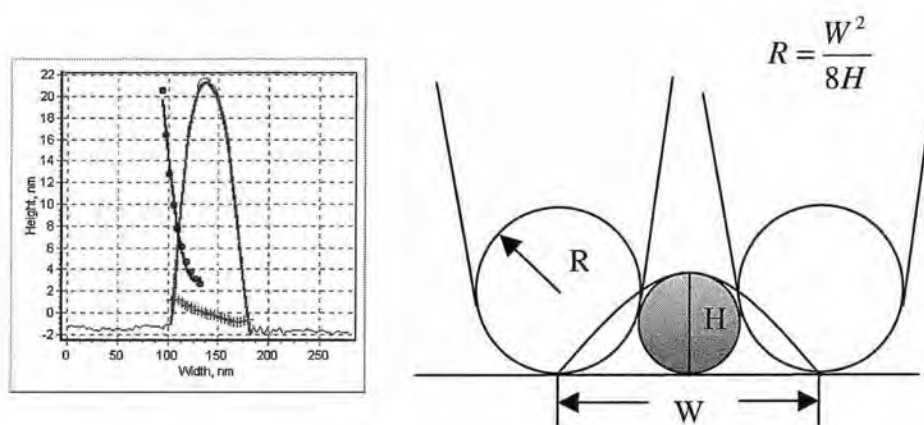


Figure 4.67. The cross section image of gold particle (left) and schematic drawing of AFM tip scanning of gold nanoparticle (right). From height and width data of captured gold nanoparticle image, the radius of AFM tip is calculated.

In the cross-section image from AFM 3-D image, height and the width are measured by software (Dimension 3000, Digital Instruments, Inc.). The tip radius is calculated by the equation (18);

$$R = \frac{W^2}{8H} \quad (18)$$

where W represents the width of cross-section image of gold particles, and H represents the height of gold particles (Chizhik, 1998). More than three directions for one particle are taken cross sections to see the deviation depending upon the axis. This procedure is repeated for 10 – 20 particles to obtain enough statistical data.

There are variety of diameters for gold nanoparticles such as, 5, 14, 18, 28, and 60 nm. The size should be chosen in terms of the purpose. Smaller particles provides better resolution of the tip image, however, in the meantime they are easy to be influenced by the surface condition. When choosing the size of gold nanoparticle, we should pay attention to this point. From our experience, 28 nm is the easiest size to scan.

Figure 4.68 demonstrates an example of the distribution of gold nanoparticle diameters taken from our measurement. For each set of different size gold particles, the difference of the average diameter was within 20 %, and statistical standard deviation was very close. (Shape of the curves were almost same.) The difference within 20 % comes from the sample preparation procedure. Actual surface of mica is coated by Poly – L – Lysine to give surface adhesion and very flat polymer surface without bumps and aggregates, however, polymer soft surface causes the penetration of gold nanoparticles into the materials, and certainly this leads the diminishing of measured height of gold nanoparticles. Especially, as time goes by, this will be more serious so one has to preserve gold nanoparticles samples in desiccator.

There are other standard samples for tip radius and shape measurement such as triangle grid, complex nano-fabricated grating, and semiconductor trench. Among them, gold nano-particle method is one of the most accurate, reliable, and simplest one. Many scientists prefer to use this method nowadays.

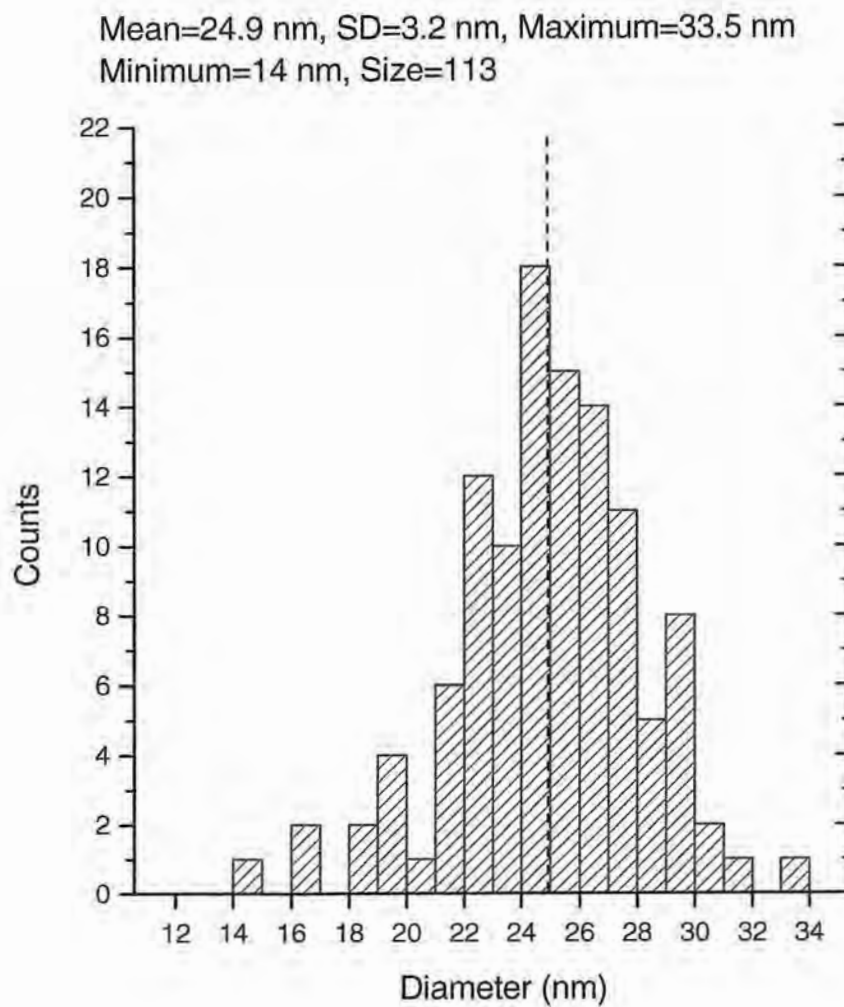


Figure 4.68. The distribution of the diameters of gold nanoparticles counted by AFM. Manufacturer provided the size as 28.3 nm.

4.6.4. Conclusions

The importance of the spring constants of cantilevers used in SPM is the fact that the spring constants of cantilevers are most influential and critical parameters to the calculation result of Young's modulus (equation 13).

The principle and methodology of the measurement of spring constant of cantilevers were described. The spring constants of SPM tips were calibrated using cantilever – against – cantilever method and tungsten added mass method. Both values were corresponded within difference of 17 %, which are reasonable range for practical use. Credited method of cantilever – against – cantilever should be now used in such occasions as one need highly accurate spring constant of cantilever within error of 15 - 20 % since obvious drawback of this method is time-consuming. For other usual micromechanics measurements, the results of regression analysis for the data taken by cantilever – against – cantilever method will be applied for each type of cantilever due to the convenience. The resonant frequency of the unloaded cantilever is the only parameter which one needs to obtain in this method. This method still provides 20 % - 30 % deviated values that are still appropriate to use for most of the micromechanics measurements. Another advantage of this method is nondestructive nature. Different from cantilever – against – cantilever, SPM tips can keep their fresh untouched condition. In cantilever – against – cantilever method, the shape and the radius of tips are sacrificed during the calibration. So the tip shape and radius must be measured after the measurement of spring constant of cantilevers.

The tip radius calibration procedure was described. SPM scanning of gold nanoparticle method was employed for this purpose. The quality of samples is very important in this method. The comparison of the diameter of gold nanoparticles obtained by SPM measurement with manufacturer's value must be done to see the availability. Because of gold nanoparticles' sink, the diameters usually show lower value than the values manufactures provide. The gold particles samples should be preserved in gentle environment such as in desiccator.

BIBLIOGRAPHY

- Amemiya, F., Goris, R. C., Masuda, Y., Kishida, R., Atobe, Y., Ishii, N., and Kusunoki, T. (1995) The surface architecture of snake infrared receptor organs, *Biomedical Research*, 16 (6) 411-421
- Beaucage, G., Compsto, R., and Stein, R. S. (1993) Ellipsometric Study of the glass transition and thermal expansion coefficients of thin polymer films, *Journal of Polymer Science: Part B: Polymer Physics*, 31, 319-326
- Binning, G. and Quate, C. F. (1986) Atomic force microscope, *Physical Review Letters*, 56(9), 930-933
- Blok, H. (1937) Theoretical study of temperature rise at surfaces of actual contact under oiliness lubricating conditions, *Proc. Gen. Discussion Lubrication & Lubricants, Inst. Mech. Eng.*, 2, 222 – 235
- Burnham, N., Dawn, D., Mowery, R., and Colton R., (1990) Probing the surface of monolayer films with an atomic-force microscope, *Physical Review Letters*, 64-16, 1931 – 1934
- Campbell, A. L., Bunning, T. J., Stone, M. O., Church, D., and Grace, M. S. (1999) Surface ultrastructure of pit organ, spectacle, and non pit organ epidermis of infrared imaging boid snakes: A scanning probe and scanning electron microscopy study, *Journal of Structural Biology* 126, 105-120
- Chapman, R. F. (1998) *The insects*, Cambridge University Press
- Chevrier, J-B, Baer, K., and Slater, T. (1995) *J. Micromech. Microeng.*, 5, 193
- Chiasson, R. B., Bentley, D. L., and Lowe, C. H. (1989) Scale morphology in *Agkistrodon* and closely related Crotaline Genera, *Herpetologica*, 45(4), 432
- Chizhik, S. A., Huang, Z., Gorbunov, V. V., Myshkin, N. K., and Tsukruk, V. V. (1998) Micromechanical properties of elastic polymeric materials as probed by scanning force microscopy, *Langmuir (Letters)*, 14(10) , 2606 – 2609
- Chizhik, S. A., Gorbunov, V. V., Luzinov, I., Fuchigami, N., and Tsukruk, V. V. (2000) Surface force spectroscopy of elastomeric nanoscale films, *Macromolecular symposium*, accepted
- Cleveland, J. P. and Manne, S., Bocek, D., and Hansma, P. K. (1993) A nondestructive method for determining the spring constant of cantilevers for scanning force microscopy, *Review of Scientific Instruments*, 64(2) 403 – 405

Digital Instruments (1996) *Scanning Probe Microscopy Training Notebook*

Evans, W. G. (1964) Infra-red receptors in *Melanophila acuminata* De Geer, *Nature*, 202, 211

French, A. S. (1992) Transduction mechanisms of mechanosensilla, *Annual Review of Entomology*, 33, 39

French, A. S. (1992) Mechanotransduction, *Annual Review of Physiology*, 54, 135

Gans, C., and Baic, D. (1997) Regional specialization of reptilian scale surfaces: relation of texture and biologic role, *Science*, 195, 1348

Golay, M. J. (1947) A pneumatic infra-red detector, *Review of Scientific Instruments*, 18, 357

Gorbunov, V. V., Fuchigami, N., Hazel, J. L., and Tsukruk, V. V. (1999) Microprobing surface thermal properties by scanning thermal microscopy, *Langmuir*, 15, 24

Gorbunov, V. V., Fuchigami, N., Tsukruk, V. V. (2000) Microthermal analysis with scanning thermal microscopy. I. methodology and experimental[&], *Probe Microscopy*, 2, 53-63

Gorbunov, V. V., Fuchigami, N., Tsukruk, V. V. (2000) Microthermal analysis with scanning thermal microscopy. II: calibration, modeling, and interpretation[&], *Probe Microscopy*, 2(1), 65-75

Gorbunov, V. V., Fuchigami, N., and Tsukruk, V. V. (2000) Microthermal probing of ultrathin polymer films, *High Performance Polymers*, 12, 603-610

Gorbunov, V. V., Fuchigami, N., and Tsukruk, V. V. (2000) Microthermal analysis of ultrathin polymeric films with scanning thermal microscopy, *Polymer Preprints*, 41, 1493-1494

Gorbunov, V. V., Fuchigami, N., and Tsukruk, V. V. (2000) Microthermal analysis with scanning thermal microscopy., *Polymer Preprints*, 41, 1495-1496

Gorbunov, V. V. (2000) MicroMechanical analysis with atomic force microscopy. *Software manual for MicroMechanical Analysis*, unpublished, 24 - 26

Granta Design Limited (1999) *CES Selector (Cambridge Engineering Selector)* version 3.0

- Guymon, C. A., Dougan, L. A., Hoggan, E. N., and Bowman, C. N. (1996) Polymerization effects on the electro-optic properties of a polymer stabilized ferroelectric liquid crystal, *MRS Symposia Proceedings*, Materials Research Society, Pittsburgh, PA, 425, 197
- Haines, P. J. (1995) *Thermal methods of analysis. Principles, applications and problems*, Blakie Academic and Professionals, Glasgow, UK
- Hammiche, A., Pollock H. M., Song, M., Hourston, D. (1996) Sub-surface imaging by scanning thermal microscopy, *Measurement Science and Technology*, 7, 142 – 150
- Hammiche, A., Reading, M., Pollock, H., Song, M., Hourston, D.J. (1996) Localized thermal analysis using a miniaturized resistive probe, *Review of Scientific Instruments*, 67(12), 4268 – 4274
- Hammiche, A., Hourston, D. J., Pollock, H. M, Reading, M., Song, M. (1996) Scanning thermal microscopy: Subsurface imaging, thermal mapping of polymer blends, and localized calorimetry, *Journal of Vacuum Science and Technology*, 14(2), 1486 – 1491
- Hanes, P. J. and Wilburn, F. W. (1995) *Thermal Methods of Analysis, Principles, Applications and Problems*, 63 - 122
- Haritonov, V.V. and Yakutin, N.V. (1997) The heat exchange in a contact different materials, *Technical Physics Journal (in Russian)*, 67(2), 1 – 6
- Harris, J. F. and Gamow, R. I. (1971) Snake infrared receptors: Thermal or photochemical mechanism?, *Science*, 172, 1252-1253
- Hazel, J. L. (1999) Quantitative, non-destructive calibration of scanned probe microscope cantilevers, Master's thesis, Western Michigan University, Kalamazoo
- Hazel, J. L. and Tsukruk, V. V. (1999) Spring constants of composite ceramic/gold cantilevers for scanning probe microscopy, *Thin Solid Films*, 339, 249-257
- Hazel, J., Stone, M., Grace, M. S., and Tsukruk, V. V. (1999) Nanoscale design of snake skin for reptation locomotions via friction anisotropy, *Journal of Biomechanics*, 32, 477-484
- Hazel, J., Fuchigami, N., Gorbunov, V. V., Schmitz, H., Stone, M., and Tsukruk, V. V. (2001) Ultra-microstructure and microthermomechanics of biological IR detectors: materials properties from biomimetic prospective, *Biomacromolecules*, accepted
- Hepburn, H. R. (1985) *Comprehensive insect physiology, biochemistry, and pharmacology*, Kerkut, G. A., Gilbert, L. I. (eds.). Pergamon Press, Oxford, 1

- Jaeger, J.C. (1942) Moving heat source and friction temperature, *J. A. Proc. Roy. Soc.*, New South Wales, 76(3), 22 – 39
- Jiang, Q., Shi, H. X., and Li, J. C. (1999) Finite size effect on glass transition temperatures, *Thin Solid Films*, 354, 283
- Johnson, K.L. (1998) Contact mechanics and adhesion of viscoelastic spheres, In: *Microstructure and Microtribology of Polymer Surfaces*, ACS Symposium Series edited by V. V. Tsukruk and K. J. Wahl, 741, 24 – 41
- Kajiyama, K., Tanaka, K., and Takahara, A (1995) Depth dependence of the surface glass transition temperature of a poly (styrene-block-methyl methacrylate) diblock copolymer film on the basis of temperature-dependent X-ray photoelectron spectroscopy, *Macromolecules*, 28, 3482-3484
- Keddie, J. L., Jones, R. L., and Cory R. A. (1994) Size-dependent depression of the glass transition temperature in polymer films, *Europhysics Letters*, 27(1), 59
- Lai, J., Chandrachud, M., Majumdar, A., and Carrejo, J. P. (1995) Thermal detection of device failure by atomic force microscopy, *IEEE Electron Device Letters*. 16(7), 312-315
- Lever, T. J. and Price, D. M. (1998) Using microthermal analysis to characterize the nanoworld, *American Laboratory*, August, 1-5
- Luo, K., Shi, Z., Varesi, J., and Majumdar, A. (1997) Sensor nanofabrication, performance, and conduction mechanisms in scanning thermal microscopy, *J. Vacuum Science and Technology*, B 15(2), 349-360
- Luzinov, I., Julthongpiput, D., Liebmann-Vinson, A., Cragger, T., Foster M.D., and Tsukruk, V. V. (1999) Epoxy-terminated self-assembled monolayers: molecular glues for polymer layers, *Langmuir*, 16(2) 504 – 516
- Majumdar, A., Carrejo, J. P. and Lai, J. (1993) Thermal imaging using the atomic force microscope, *Applied Physics Letters*, 62, 2501 – 2503
- Majumdar, A., Lai, J., Chandrachud, M., Nakabeppu, O., Wu, Y., and Shi, Z. (1995) Thermal imaging by atomic force microscopy using thermocouple cantilever probes, *Review of Scientific Instruments*, 66 (6), June
- MatWeb (1998) <http://www.matls.com/searchindex.html>
- Neville, A. C. (1975) *Biology of the Arthropod Cuticle*. Springer

- Newman, E. A., and Hartline, P. H. (1982) The infrared "vision" of snakes, *Scientific American*, 246, 116-127
- Nonnenmacher, M., and Wickramasinghe, H. K. (1992) Scanning probe microscopy of thermal conductivity and subsurface properties, *Applied Physics Letters*, 61, 168
- Oesterschulze, E., Stopka, M., Kassing, R. (1994) Photo-thermal characterization of solids and thin films by optical and scanning probe techniques, *Microelectronic Engineering*, 24, 107 – 112
- Orts, W. J., van Zanten, J. H., W., W. L., and Satija, S. K. (1993) Observation of temperature dependent thickness in ultrathin polystyrene films on silicon, *Physical Review Letters*, 71, 867
- Overney, R. (2000) Size and confinement effects in thin polymer films, *Polymer Preprint*, 41(2), 1474 – 1475
- Pollock, H. M., Hammiche, A., Song, M., Hourston, D. J., and Reading, M. (1998) Interfaces in polymeric systems as studied by C.A.S.M – A new combination of localized calorimetric analysis with scanning microscopy, *Journal of Adhesion*, 67, 217 - 234
- Price, D. M., Reading, M., Hammiche, A., Pollock, H. M., and Branch, M. G. (1999) Localised thermal analysis of a packaging film, *Thermochimica acta*, 332, 143-149
- Prucker, O., Christian, S., Bock, H., Rühle, J., Frank, C. W., and Knoll, W. (1996) Glass transition in ultrathin polymer films, *Organic Thin Films*, Edited by Curtiss, W. Frank., ACS Symposium series 695, 233-249
- Ratner, B., Tsukruk, V. V. Eds. (1998) *Scanning Probe Microscopy in Polymers*, ACS Symposium Series, 694
- Reading, M and Hanes, P. J. (1995) *Thermal Methods of Analysis: Principles, Applications and Problems*, Blackie Academic & Professional, London, 123-160
- Reading, M., Price, D. M., Pollock, H. M., Hammiche, A. and Murray, A. (1999) Recent progress in microthermal analysis, *American Laboratory*, January, 1-4
- Reading, M., Price, D. M., Pollock, H. M., Hammiche, A., and Craig, D. Q. M. (1998) Royal, P., *Journal of Pharmacy and Pharmacology*, 50, 8
- Rief, M., Oesterhelt, O., Heymann, B. and Gaub, H. E. (1997) Single molecule force spectroscopy on polysaccharides by atomic force microscopy, *Science* 275, 1295-1297

- Sadar, J. E., Chon, J. W. M., and Mulvaney, P. (1999) Calibration of rectangular atomic force microscope cantilevers, *Review of Scientific Instruments*, 70(10), 3967 - 3969
- Schmitz, H., Bleckmann, H., and Murtz, M. (1997) Infrared detection in a beetle, *Nature*, 386, 773
- Schmitz, H., and Bleckmann, H., (2000) Response of the infrared sensilla of *Melanophila acuminata* (Coleopta: Buprestidae) to monochromatic infrared stimulation, *Journal of Comparative Physiology, A*, 186, 543 - 549
- Sperling, L. H. (1992) *Introduction to physical polymer science*, Wiley-Interscience Publication
- Srinivasan, A. V., Haritos, G. K., Hedberg, F. L., and Jones, W. F. (1996) Biomimetics: Advancing man-made materials through guidance from nature, *Appl. Mech. Rev.* 49, (10), part 2, S194-S200
- Stille, B. (1987) Dorsal scale microdermatoglyphics and rattlesnake (*Crotalus* and *Sistrurus*) phylogeny (Reptilia: Viperidae: Crotalinae) *Herpetologica*, 43 (1), 98-104
- TA Instruments, Inc. (1999) *µTA 2990 MicroThermal Analyzer Operator's Manual*. PN 899094.002, 3-50 – 3-58
- TA Instruments, Inc., (1999) Micro-Thermal analysis – An holistic approach to materials characterization, www.tainst.com/products/thermal.html#
- TA Instruments, Inc., (1999) Characterisation of surface morphology changes by micro-thermal analysis, www.tainst.com/products/thermal.html#
- TA Instruments, Inc., (1999) Modulated DSC™ Compendium, basic theory & experimental considerations, www.tainst.com/products/thermal.html#
- Thompson, L. F., Willson, G., and Tagawa, S. (editors) (1994) *Polymers for microelectronics: resists and dielectrics*, American Chemical Society
- Thurm, U. (1996) *Neurowissenschaft*, Dudel, J.; Menzel, R.; Schmidt, R. F. (eds.). Springer, Berlin, Heidelberg, New York, 331
- TopoMeteix, Inc. (1998) *TopoMetrix User's Manual Addendum – SThM*, 1-5
- Trannoy, N., Grossel, P., and Troyon, M. (1998) Thermal effects induced by laser irradiation in scanning tunneling microscopy: thermal expansion of sample and tip influence, *Probe Microscopy*, 1, 201-206

- Tsukruk, V. V., Bliznyuk, V. N., Hazel, J., and Visser, D. (1996) Organic molecular films under shear forces: Fluid and solid langmuir monolayers, *Langmuir*, 12(20), 4840-4849
- Tsukruk, V. V. and Wahl, K. (2000) Eds. *Microstructure and microtribology of polymer surfaces*, ACS Symposium Series: Washington DC, 741
- Tsukruk, V. V., Huang, Z., Chizhik, S. A., and Gorbunov (1998) V. V., Probing of micromechanical properties of compliant polymeric materials, *Journal of Materials Science letters*, 33, 4905 – 4909
- Van Krevelen (1997) D. V., *Properties of Polymer*, Elsevier
- Vesenska, J., Manne, S., Gilbertson, R., Marsh, T., and Henderson, E., (1993) Colloidal gold particles as an incompressible atomic force microscope imaging standard for assessing the compressibility of biomolecules, *Biophysical Journal*, 65, 992-997
- Vondran, T., Apel, K. –H., Schmitz, H. (1995) The infrared receptor of *Melanophila acuminata* De Geer (Coleoptera: Buprestidae): ultrastructural study of a unique insect thermoreceptor and its possible descent from a hair mechanoreceptor, *Tissue & Cell*, 27, 645 – 658
- Walters, D. A., Cleveland, J. P., Thomson, N. H., and Hansma, P. K. (1996) Short cantilevers for atomic force microscopy, *Review of Scientific Instruments*, 67(10), 3583 - 3520
- Williams, C. C.;Wickramasinghe, H. K. (1986) Scanning thermal profiler, *Applied Physics Letters*, 49, 1587
- Williams, C. C.;Wickramasinghe, H. K. (1988) Photothermal imaging with sub-100-nm spatial resolution, In: *Photoacoustic and Photothermal Phenomena*, ed Hess, P. and Peltzl, J., Springer-Verlag, Berlin, 364-369